



Universidad Autónoma  
de Madrid

– Facultad de Ciencias–

**Atomistic Description of Thermodynamic Forces in Open  
Systems for Equilibrium and Non-Equilibrium Quantum  
Electron Transport**

Tesis para obtener el título académico de  
Philosophiæ doctor (Ph.D.)

presentado por **Carlos Salgado**

Director : Prof. Dr. Juan José Palacios



Part I

FRONTMATTER

## DECLARATION

---

Por la presente declaro que he escrito el presente trabajo de forma independiente y no he utilizado ninguna otra fuente que las indicadas en la bibliografía.

Los capítulos 2, 4, 3, 5 y 6 se basan en material que se ha publicado o se publicará en distintas revistas científicas. Estos contienen oraciones, párrafos, figuras y tablas idénticas a las referencias presentes en el apartado 'Publications'.

Este trabajo aún no se ha presentado a ninguna otra autoridad de examen en la misma forma o similar.

*Madrid, 17. October 2019*

---

Carlos Salgado

ABSTRACT

---

The thesis project consists in the theoretical and computational investigation of the influence on the mechanical properties of nanoscale conductors due to the presence of thermodynamic equilibrium rupture conditions, under current conditions of particles and energy (1, 2). They are analyzed by nanostructures such as metal nanocontacts, rare earth nanocontacts (Europium, Gadolinium), two-dimensional nanomaterials (graphene), molecular conductors ...

The main line of the project deals with the theoretical description at the atomic level of the interaction between electronic-spintronic transport and the nanomechanics of the conductors, that is, the forces experienced by each atom, the result of transport conditions and rupture of equilibrium. This phenomenon is known as electromigration. The aforementioned phenomenology gives rise to applications in Nanotechnology, as is the case of the manipulation of individual atoms mediated by voltage and current (4,6). Individual atoms serve as building-blocks for nanoengineering, nanoelectronics and nanospintronics. As a result of the collaboration with experimental physicists from other universities, the study of magnetic properties of rare earth nanocontacts such as Europium and Gadolinium was carried out in the presence of a very densely localized electric current and a strong magnetic field (5).

The core of the methodology used to address the problems raised is standard in the Theoretical Physics of Condensed matter and Nanotechnology when they are treated from the theoretical-computational mechano-quantum approach.

In the first place, the so-called Functional Density Theory (DFT) intervenes, in this case, applied on a base of localized Gaussian wave functions that make up a reduced Hilbert space. This method based on the use of localized orbitals is known as the Linear Combination of Atomic Orbitals (LCAO), and is of conventional use in the study of finite mechano-quantum systems (such as molecules) and periodic infinity (such as crystals).

The foundation of the thermodynamic forces acting on atoms lies in the Lippmann-Schwinger Scattering State Formalism, which explains the behavior of particles through a constriction or potential obstacle. This formalism, in order to be implemented computationally in simulations, needs to be translated into the Green Functions Off-Balance (NEGF) method. The incorporation of the electrodes or reservoirs of particles through boundary conditions allows reproducing the conditions of infinite non-periodic system. These are necessary to study nanoscale contacts between macroscopic electrodes and simulate the rupture of electrochemical equilibrium. There is a matrix form of the NEGF formalism, which is given by the description of the electron density projected as a matrix on the basis of wave functions of Gaussian profile. This description facilitates the compatibility of this formalism with the previous one, the LCAO-DFT. The combination of both methods is widespread among the community

of scientists specialized in the fields of Nanophysics, Nanoelectronics and Nanospintronics.

The theoretical extension of the formalism that describes the thermodynamic forces through the NEGF-DFT method in its LCAO form for the description of electronic and spintronic systems out of balance is the central object of this thesis.

RESUMEN

---

El proyecto de tesis consiste en la investigación teórica y computacional de la influencia sobre las propiedades mecánicas de conductores a escala nanométrica debidas a la presencia de condiciones de ruptura del equilibrio termodinámico, bajo condiciones de corriente de partículas y energía (1,2). Son objeto de análisis nanoestructuras como nanocontactos metálicos, nanocontactos de tierras raras (Europio, Gadolinio), nanomateriales bidimensionales (grafeno), conductores moleculares...

La línea principal del proyecto trata la descripción teórica a nivel atómico de la interacción entre transporte electrónico-spintrónico y la nanomecánica de los conductores, esto es, las fuerzas que experimenta cada átomo, fruto de las condiciones de transporte y ruptura del equilibrio. A este fenómeno se le conoce como electromigración. La mencionada fenomenología da lugar a aplicaciones en Nanotecnología, como es el caso de la manipulación de átomos individuales mediada por voltaje y corriente (4,6). Los átomos individuales cumplen la función de building-blocks para hacer nanoingeniería, nanoelectrónica y nanospintrónica. Como resultado de la colaboración con físicos experimentales de otras universidades se ha llevado a cabo el estudio de propiedades magnéticas de nanocontactos de tierras raras como Europio y Gadolinio en presencia de corriente eléctrica muy densamente localizada y campo magnético fuerte (5).

El núcleo de la metodología empleada para abordar los problemas planteados es estándar en la Física Teórica de la materia Condensada y la Nanotecnología cuando son tratadas desde la aproximación teórica-computacional mecano-cuántica.

En primer lugar interviene la conocida como Teoría del Funcional Densidad (DFT, por sus siglas en inglés), en este caso, aplicada sobre una base de funciones de onda gaussianas localizadas que conforman un espacio de Hilbert reducido. A este método basado en el uso de orbitales localizados se le conoce como Combinación Lineal de Orbitales Atómicos (LCAO), y es de uso convencional en el estudio de sistemas mecano-cuánticos finitos (como moléculas) e infinitos periódicos (como cristales).

La fundamentación de las fuerzas termodinámicas que actúan sobre los átomos radica en el Formalismo de estados de Scattering de Lippmann-Schwinger, que explica el comportamiento de las partículas atravesando una constricción o un obstáculo de potencial. Este formalismo, a fin de ser implementado computacionalmente en simulaciones, necesita ser traducido al método de Funciones de Green fuera del equilibrio (NEGF). La incorporación de los electrodos o reservorios de partículas a través de las condiciones de frontera permite reproducir las condiciones de sistema infinito no periódico. Estas son necesarias para estudiar contactos de escala nanométrica entre electrodos macroscópicos y simular la ruptura del equilibrio electroquímico. Existe una forma matricial del formalismo NEGF, que viene dada por la descripción de la densidad electrónica proyectada como matriz sobre la base de funciones de onda de perfil gaussiano. Esta descripción facilita la compatibilidad de este formalismo con el anterior, el LCAO-DFT. La combinación de ambos métodos está extendida entre la

comunidad de científicos especializados en los ámbitos de la Nanofísica, Nanoelectrónica y Nanospintrónica.

La extensión teórica del formalismo que describe las fuerzas termodinámicas a través del método NEGF-DFT en su forma LCAO para la descripción de sistemas electrónicos y spintrónicos fuera del equilibrio es el objeto central de esta tesis.

## PUBLICATIONS

---

- González-Herrero, H., Gómez-Rodríguez, J., Mallet, P., Moaied, M., Palacios, J., Salgado, C., ... Brihuega, I. (2016). Atomic-scale control of graphene magnetism by using hydrogen atoms. *Science*. 352(6284). doi:[10.1126/science.aad8038](https://doi.org/10.1126/science.aad8038)
- Müller, M., Salgado, C., Néel, N., Palacios, J., & Kröger, J. (2016). Plasticity of single-atom Pb junctions. *Physical Review B*. 93(23). doi:[10.1103/PhysRevB.93.235402](https://doi.org/10.1103/PhysRevB.93.235402)
- Olivera, B., Salgado, C., Lado, J., Karimi, A., Henkel, V., Scheer, E., ... Untiedt, C. (2017). Electronic transport in gadolinium atomic-size contacts. *Physical Review B*. 95(7). doi:[10.1103/PhysRevB.95.075409](https://doi.org/10.1103/PhysRevB.95.075409)
- Salgado, C. & Palacios, J. (2019). Atomistic Evaluation of Thermodynamic Forces in Open Systems for Equilibrium and Non-Equilibrium Electron Quantum Transport. TO BE PUBLISHED.

## ACKNOWLEDGMENTS

---

My grandmother, Celinda, because you treated me like I was your son.

To my love, Bea, because life was never as it is with you now.

My mother, Celinda, for teaching me what courage is.

To Juanjo, for giving me the opportunity, and also the freedom, to develop a thesis on an ambitious topic and, of course, for financial support.

To Elsa Prada, J. Gómez-Herrero, J.M. Soler and to all those who have helped me during my journey at the UAM.

To all the people with whom I have collaborated in the research, and they have most of the merit: Héctor González-Herrero, José M. Gómez-Rodríguez, Félix Yndurain, Iván Brihuega, Bernat Olivera, Jose L. Lado, Elke Scheer, Joaquín Fernández-Rossier, Carlos Untiedt, M. Müller, N. Néel, J. Kröger, Pierre Mallet, Miguel M. Ugeda, Jean-Yves Veuillen, A. Karimi, V. Henkel and Mohamed Moaied.

To Álvaro, Artu, Víctor, Nano, Paula, Pipo, Rodrigo, Román, Gros, Willy, Godo, Pablo, Dani, Miguel, Goofy and all my friends, who really are the big part of my family.

To Ayquemal and all my colleagues in the infamous character exchange network.

To all the people who just entered my life, for being so nice to me.

To my new coworkers for identical reasons, and my new bosses, for trusting me.

A very special gratitude goes out to all down at Research Fund and also Rich Foundation for helping and providing the funding for the work.

And finally, last but by no means least, also to everyone in the open-source community, who help me every day doing what I love. Special mention for stackoverflow.

Thanks for all your encouragement!

# CONTENTS

---

## I FRONTMATTER

1	ABSTRACT	vii
2	RESUMEN	ix

## II THESIS

1	GREEN'S FUNCTION	3
1.1	Hamiltonian	3
1.2	Green's function	5
1.3	Mean Field Theory: Hartree-Fock method	8
1.4	Steady-state formalism	12
1.4.1	Transient solution	17
2	THEORY	19
2.1	Abstract	19
2.2	Introduction	19
2.3	Equations	20
2.3.1	Canonical Grand-Potential $\Omega$	20
2.3.2	Nonequilibrium statistical operator	21
2.3.3	Forces	25
2.3.4	Analytical derivatives	26
2.4	Results	28
2.4.1	Atom adsorption onto a single electrode: checking the method	29
2.4.2	Two electrodes	32
2.4.3	Attraction between the plates of a quantum capacitor	34
2.4.4	Electromigration of an atom between two electrodes	34
2.4.5	Alternative formulation in terms of the current operator	36
3	NEGFY CODE	39
3.1	Abstract	39
3.2	Description	39
3.3	Results	39
4	HYDROGEN ADSORPTION FROM GRAPHENE WITH A Pt STM TIP	41
4.1	Abstract	41
4.2	Introduction	41
4.3	Experimental atomic H manipulation	42
4.4	Theoretical methodology H on graphene	42
4.5	10. Pt tip manipulation of H	43
4.6	Conclusions	44
5	ELECTRONIC TRANSPORT IN GADOLINIUM ATOMIC-SIZE CONTACTS	47
5.1	Abstract	47
5.2	Introduction	47
5.3	Experiments	49

5.4	Theory . . . . .	55
5.5	Conclusions . . . . .	60
6	PLASTICITY OF SINGLE-ATOM PB JUNCTIONS	63
6.1	Abstract . . . . .	63
6.2	Introduction . . . . .	63
6.3	Experimental . . . . .	65
6.4	Results and discussion . . . . .	66
6.5	Conclusions . . . . .	74
<b>III APPENDIX</b>		
A	NOTATION FOR THE POSITION-SPIN REPRESENTATION	77
B	TIME EVOLUTION	79
B.1	Equations of motion for operators in the Heisenberg picture . . . . .	80
C	TIME-DEPENDENT QUANTUM AND ENSEMBLE AVERAGES.	83
C.1	Time-dependent quantum averages: the Keldysh contour . . . . .	83
C.2	Time-dependent ensemble averages: the density matrix operator . . .	85
D	EQUATIONS OF MOTION OF THE GREEN'S FUNCTION ON THE CONTOUR	89
D.1	Equations of motion on the contour . . . . .	89
D.2	Operator correlators on the contour . . . . .	89
D.3	The Green's function as the average of the correlators . . . . .	93
E	THE MEAN-FIELD APPROXIMATION: HARTREE-FOCK AND THE DYSON EQUATION	95
E.1	The Hartree-Fock Approximation . . . . .	95
E.1.1	The Dyson equations . . . . .	97
F	THE EMBEDDING SELF-ENERGY	101
F.1	The Embedding Self-Energy . . . . .	101
G	THE SELF-CONSISTENT METHOD	107
H	KELDYSH COMPONENTS IN STEADY-STATE	109
H.1	Steady-State Ensemble Averages . . . . .	111
<b>IV SUMMARY AND OUTLOOK - RESUMEN Y PERSPECTIVAS</b>		
1	CONCLUSIONS	117
2	CONCLUSIONES	119
<b>V BIBLIOGRAPHY</b>		

## LIST OF FIGURES

---

Figure 2.1	Toy representation of an atomic contact between whose two tips an atom can be moved by means of bias or temperature, following the gradient of the canonical grand potential $\Omega$ vs. position $x$ curve. . . . .	28
Figure 2.2	Two different systems to be compared. System (a) is a finite chain to whose tip the red adatom can be chemisorbed, developing the internal energy $U$ vs. position $x$ curve. System (b) is an infinite chain, modelled by a 1D-reservoir, to whose tip the red adatom can be also chemisorbed, developing, in this case, the canonical grand potential $\Omega$ vs. position $x$ curve. . . . .	30
Figure 2.3	Energy-distance curves for the adsorption of an adatom on the tip of a chain. The blue dotted line represents the internal energy $U$ curve for the adsorption on a finite 20-atom chain. The purple, brown and red lines, which lie far below the dotted one, represent the internal energies $U$ of 2-, 3- and 4-atom chains connected to an infinite reservoir chain providing the open boundary conditions, which are not correct. The blue, red and yellow lines, which approach progressively the dotted one, represent the canonical grand potential $\Omega$ of 2-, 3- and 4-atom chains connected to an infinite reservoir chain providing the open boundary conditions, which are correct. . . . .	30
Figure 2.4	Energy-distance curves for the adsorption of an adatom on the tip of a chain. The blue line represents the internal energy $U$ curve for the adsorption on a finite 20-atom chain. The red discontinuous line represents the internal energies $U$ of a 6-atom chain connected to an infinite reservoir providing the open boundary conditions. The yellow dotted line, which approaches the blue one, represents the canonical grand potential $\Omega$ of a 6-atom chain connected to an infinite reservoir providing the open boundary conditions. . . . .	32
Figure 2.5	Energy-distance curves for the adsorption of an adatom on the tip of a chain. The blue dotted line represents the internal energy $U$ curve for the adsorption on a finite 20-atom chain. The purple, brown and red lines, which lie far below the dotted one, represent the internal energies $U$ of 2-, 3- and 4-atom chains connected to an infinite reservoir chain providing the open boundary conditions, which are not correct. The blue, red and yellow lines, which approach progressively the dotted one, represent the canonical grand potential $\Omega$ of 2-, 3- and 4-atom chains connected to an infinite reservoir chain providing the open boundary conditions, which are correct. . . . .	33

Figure 2.6	Energy curves for the separation of the two plates of a quantum 1D atomic capacitor consisting of two semiinfinite chains. The tip-tip distance is represented in the horizontal axis, while the vertical one represents the calculated canonical grand potential $\Omega$ . . . . .	34
Figure 2.7	Energy curves for an atom moving between two diatomic single-orbital tips with two vacancies between them. The tip-tip distance is three times the lattice parameter of the chains. The blue curve represents the internal energy $U$ vs. position, while the red dashed curve represents the grand potential $\Omega$ vs. position curves. . . . .	35
Figure 2.8	Energy curves for an atom moving between two diatomic single-orbital tips with two vacancies between them. Thus, the tip-tip distance is three times the lattice parameter of the chains. All the curves represent the grand potential $\Omega$ vs. position curves at different applied voltages. . . . .	36
Figure 2.9	Energy curves for an atom moving between two diatomic single-orbital tips with two vacancies between them. The tip-tip distance is three times the lattice parameter of the chains. All the curves represent the grand potential $\Omega$ vs. position curves at different applied temperature gradients. . . . .	37
Figure 2.10	Variation of the ensemble average $\langle \hat{Y}^Q \rangle$ with the distance for a symmetric atomic 1D-contact. The blue lines display the voltage based conventional expression $\langle \hat{Y}^Q \rangle$ while the red discontinuous ones represent $\langle \hat{Y}_I^Q \rangle$ . Results for voltages of $0.1V$ , $0.2V$ and $0.3V$ are shown in subfigures (a), (b) and (c) respectively. . . . .	38
Figure 3.1	Energy-distance curves for the adsorption of an adatom on the tip of a chain. The blue line represents the internal energy $U$ curve for the adsorption on a finite 20-atom chain. The red discontinuous line represents the canonical grand potential $\Omega$ of a 6-atom chain connected to an infinite reservoir providing the open boundary conditions as calculated with a simple model. The yellow dotted line, which approaches the blue one, represents also the canonical grand potential $\Omega$ of a 6-atom chain connected to an infinite reservoir, but calculated with NEGFY code. . . . .	40
Figure 4.1	DFT calculation of the evolution of the binding energy of the H atom in between the tip and graphene as a function of tip-sample distance. See movie S1 for the complete sequence . . . . .	45

- Figure 5.1 Typical conductance traces for atomic size contacts made out of Gd. Bright/dark curves stand for breaking/creating contacts as arrows indicate. Upper plot: Measurements taken with STM technique in equilibrium with liquid He bath and at  $10^{-8}$  mbar. All traces have been taken at 100 mV bias voltage. Inset: artistic representation of nanocontacts; hcp ball-stacking is pictured, where balls represent atoms. Lower plot: Measurements taken with lithographic MCBJ technique in equilibrium with liquid He bath and at  $10^{-5}$  mbar. Red and green traces and their return traces have been taken at 5 mV bias voltage, yellow curve has been taken at 10 mV. . . . . 50
- Figure 5.2 Histograms of conductance calculated from conductance traces for Gd atomic-size contacts. Upper/lower plot stands for breaking/closing contact mode. Same colors for upper and lower plot stand for a set of traces with electrodes that have not been modified with deep indentations (i.e. less than  $\approx 20 \frac{2e^2}{h}$ ). The different colors illustrate the variability in the histograms between contacts, or for different choices of depth of indentations. All measurements have been taken with STM technique at 100 mV bias voltage in equilibrium with liquid He bath and  $10^{-8}$  mbar, except the purple curve, that has been taken with MCBJ technique, where a bias voltage of 10 mV has been applied. For STM histograms few (from 1 to 10) thousands of traces are considered. For MCBJ  $\approx 500$  traces are included. . . . . 52
- Figure 5.3 (Linear color scale) Overlapped Gd conductance traces measured with STM. Breaking contact (left-sided plot) and creating contact (right-sided plot) situations are shown. Traces are centered to 1 nm when  $0.01 \frac{2e^2}{h}$  is reached from higher/lower to lower/higher conductance values for breaking/creating contacts. Total number of traces are 2524 and 2511 for breaking and creating contact cases, respectively. . . . . 53
- Figure 5.4 Spin resolved projected density of states onto the  $d$ -levels of Gd, in chain (a) and bulk (b) structures. Chain structures show net spin polarization in the  $d$ -manifold, apart from the one due to  $f$ -electrons. In comparison, bulk structures do not show polarization in the  $d$ -manifold, being the magnetism almost entirely due to localized  $f$ -levels. . . . . 56
- Figure 5.5 Spin resolved density of states of Gd in chain structures calculated with ELK (LAPW) projected onto the manifolds  $s$  (a),  $p$  (b),  $d$  (c) and  $f$  (d). Same cases calculated with CRYSTAL14 (LCAO) ( $s$  (e),  $p$  (f),  $d$  (g) and  $f$  (h)). . . . . 57

Figure 5.6	Gd $\langle 111 \rangle$ nanocontact calculated conductance-distance characteristic. Upper plot: two atomically-sharp tips in the $\langle 111 \rangle$ direction forming a dimeric contact. The distance $\Delta z$ equals 0 when the distance between both tip apex atoms equals the n.n. distance in bulk. Lower plot: an atomically-sharp tip in the $\langle 111 \rangle$ direction against a blunt $\langle 111 \rangle$ one. Both tips touch to form a monomeric contact. The distance $\Delta z$ equals 0 when the distance between the tip apex atom in the atomically-sharp tip and each tip apex atom in the blunt one equals the n.n. distance in bulk. . . . .	58
Figure 5.7	Spin resolved principal eigenchannels . . . . .	61
Figure 6.1	(a) Representative conductance evolution of a junction comprising Pb(111) and a Pb-coated W tip acquired at 50 mV. Tip approach (black line) leads to an exponential increase of the conductance in the tunneling range (displacements $\Delta z < 0$ pm). The abrupt change of the conductance from $G_j = 0.2 G_0$ to $G_c = 2.9 G_0$ at $\Delta z = 0$ pm reflects the formation of the contact. In the probed contact range ( $\Delta z > 0$ pm) the conductance increases linearly. Upon tip retraction (gray line) the conductance decreases linearly and reveals instabilities in the form of, e.g., two-level fluctuations (dashed rectangle). The definition of the hysteresis width, $H$ , is indicated. Inset: Two-level fluctuations observed in the conductance trace upon tip retraction. (b) As (a) for a contact to a single Pb adatom on Pb(111) with $G_j = 0.1 G_0$ and $G_c = 2.2 G_0$ . Inset: Pseudo-three-dimensional representation of an STM image of Pb(111) (0.1 V, 55 pA, 50 nm $\times$ 50 nm). Two terraces are visible. A Pb adatom appears as a protrusion on the upper terrace. Additional structure is due to near-surface voids induced by Ar <sup>+</sup> bombardment. (Schmid, Hebenstreit, Varga, & Crampin, 1996; Kurnosikov, Adam, Swagten, De Jonge, & Koopmans, 2008) Image processing was performed by Nanotec WSxM. (Horcas et al., 2007) (c), (d) Density plots of all acquired conductance traces [137 for Pb(111), 19 for single Pb adatoms]. The color scale depicts the number of conductance data linearly grouped into bins defined by a regular 90 $\times$ 90 grid, which was spanned from $-1090$ pm to 260 pm and from $0 G_0$ to $7 G_0$ . Full lines are the conductance traces shown in (a), (b). . . . .	67
Figure 6.2	Histograms of observed contact conductances ( $G_c$ ) on pristine Pb(111) (a) and on single Pb adatoms (b). (c), (d) Histograms of hysteresis widths ( $H$ ) observed from closing and subsequent breaking of junctions comprising Pb(111) and single Pb adatoms, respectively. All contacts were formed with bias voltages ranging from $-50$ mV to 50 mV. . . . .	69

Figure 6.3	Calculations of conductance-distance characteristics during forming and breaking of Pb contacts. (a) A single-atom terminated tip approaches (filled symbols) to and retracts (open symbols) from on-top (squares) and hollow (circles) Pb(111) lattice sites. (b) Same as (a) for a single Pb adatom (triangles). (c), (d) Position of single-atom terminated tip (filled and hatched circles for apex atom and second-layer atoms, respectively) relative to the Pb(111) lattice (circles) for contacts comprising the on-top (c) and the hollow (d) site. (e), (f) Like (a), (b) for a four-atom terminated tip. (g), (h) Position of four-atom terminated tip (filled circles) relative to the Pb(111) lattice (circles) for contacts comprising the on-top (g) and hollow (h) site. (i) Snapshots of calculated contact geometries for a single-atom terminated tip approaching an on-top site of pristine Pb(111). Increasing (decreasing) displacements ( $\Delta z$ ) correspond to tip approach (retraction). Upon retraction the tip apex atom (encircled by a full red line) is transferred to a Pb(111) hollow site adjacent to the approached on-top site. . . . . 72
Figure H.1	Contour for the Hamiltonian $\hat{H}(z)$ to calculate the time-dependent ensemble average of any operator in a system whose time-evolution is governed by the Hamiltonian $\hat{H}(z)$ from the initial equilibrium in $t_0$ . The system is supposed to be at temperature $T$ , being $\beta = 1/(k_B T)$ . . . . . 112

## LIST OF TABLES

---

Table 6.1	Calculated contact conductances ( $G_c$ ) and hysteresis widths ( $H$ ) of atom-sized Pb junctions. Pb tips grown in the $\langle 100 \rangle$ ( $\langle 111 \rangle$ ) have apices terminated by 1 and 4 (1 and 3) atoms. On pristine Pb(111) contacts are formed at on-top and hollow sites. The contacted single Pb adatom resides at a Pb(111) hollow site. . . . .	73
-----------	--	----

Part II

THESIS

## GREEN'S FUNCTION

---

### 1.1 HAMILTONIAN

We treat systems with scattering Hamiltonian operators of the form  $\hat{H} = \hat{H}_0 + \hat{H}_{int}$ , which can be written in terms of the Lippmann-Schwinger scattering states operators, which diagonalize the Hamiltonian, as:

$$\hat{H}(\mathbf{x}, t) = \sum_{k\alpha} \epsilon_{k\alpha} \hat{\psi}_{k\alpha}^\dagger(\mathbf{x}, t) \hat{\psi}_{k\alpha}(\mathbf{x}, t) \quad (1.1)$$

where  $\hat{\psi}_{k\alpha}^\dagger$  creates a particle in the eigenstate with eigenenergy  $\epsilon_{k\alpha}$  connected to reservoir  $\alpha$  (typically  $L, R$ ) and  $k$  labels the continuum of states.

It is important to notice that in equation (1.1) and throughout this book  $\mathbf{x} = (\mathbf{r}\sigma)$  is contraction for the position-spin coordinate, based on the notation in reference (Stefanucci & Van Leeuwen, 2010) and explained in A. Thus, there is no need to specify the spin component of the scattering eigenstate operators  $\hat{\psi}_{k\alpha}^\dagger(\mathbf{x}, t)$ , because it is completely specified by entry  $\mathbf{x}$ .

The expression of the scattering Hamiltonian in terms of its eigenstates is closely related to the expression of the number operator  $\hat{N}$ :

$$\hat{N}(\mathbf{x}, t) = \sum_{k\alpha} \hat{\psi}_{k\alpha}^\dagger(\mathbf{x}, t) \hat{\psi}_{k\alpha}(\mathbf{x}, t) \quad (1.2)$$

If we convert the expressions to a general basis set of spin-orbitals  $\varphi_i(\mathbf{x})$ , where the Lippmann-Schwinger scattering eigenstates take the form of a linear combination:

$$\hat{\psi}(\mathbf{x}, t) = \sum_i \varphi_i(\mathbf{x}) \hat{d}_i(t); \quad \hat{\psi}^\dagger(\mathbf{x}, t) = \sum_i \varphi_i^*(\mathbf{x}) \hat{d}_i^\dagger(t); \quad (1.3)$$

we get expressions for the operators which are more suitable for the computations, for example, if the  $\varphi_i(\mathbf{x})$  basis constitutes a combination of plane waves or a linear combination of atomic orbitals (LCAO), by which the infinite system can be decomposed to the Caroli partition scheme, frequent in the literature (Datta, 1995; Caroli, Combescot, Nozieres, & Saint-James, 1971). This Hamiltonian consists of a noninteracting part and an interacting one as:

$$\hat{H} = \hat{H}_0 + \hat{H}_{int} \quad (1.4)$$

The noninteracting  $\hat{H}_0$  part in second quantization is:

$$\begin{aligned} \hat{H}_0 = & \underbrace{\sum_{\substack{mn \\ \sigma_m = \sigma_n}} H_{mn}^C \hat{d}_{m\sigma}^\dagger \hat{d}_{n\sigma}}_{\text{central region}} + \underbrace{\sum_{\alpha k} \epsilon_{\alpha k} \hat{n}_{\alpha k}}_{\text{reservoirs}} \\ & + \underbrace{\sum_{\substack{m, \alpha k \\ \sigma_{\alpha k} = \sigma_m}} T_{m\alpha k} \hat{d}_m^\dagger \hat{d}_{\alpha k} + T_{\alpha k m} \hat{d}_{\alpha k}^\dagger \hat{d}_m}_{\text{coupling}} \end{aligned} \quad (1.5)$$

where  $\alpha$  labels each reservoir and the quantum numbers  $m, n, k$  of the general basis of spin-orbitals are the contraction for an orbital and a spin quantum number, based on the notation in reference (Stefanucci & Van Leeuwen, 2010) and explained in A, so that:

$$m = s_m \sigma_m; \quad n = s_n \sigma_n; \quad k = s_k \sigma_k. \quad (1.6)$$

In equation (1.5) the sum is restricted to matrix elements where  $\sigma_m = \sigma_n$  in the central region  $C$  and  $\sigma_{\alpha k} = \sigma_m$  for the coupling because the one-body interactions in the noninteracting Hamiltonian  $\hat{H}_0$  involved are independent of spin.

In the other hand, the Hartree-Fock-like interaction:

$$\hat{H}_{int} = \frac{1}{2} \sum_{\substack{ijmn \\ \sigma_i = \sigma_n \\ \sigma_j = \sigma_m}} v_{ijmn} \hat{d}_i^\dagger \hat{d}_j^\dagger \hat{d}_m \hat{d}_n \quad (1.7)$$

where the interaction is restricted to wavefunctions localized in the central region and the matrix elements  $v_{ijmn}$  are:

$$v_{ijmn} = \int d\mathbf{x} d\mathbf{x}' \varphi_i^*(\mathbf{x}) \varphi_j^*(\mathbf{x}') v(\mathbf{x}, \mathbf{x}') \varphi_m(\mathbf{x}') \varphi_n(\mathbf{x}) \quad (1.8)$$

In equations (1.7) and (1.8), as in equations (1.5) and (1.6), the quantum numbers of the general basis of spin-orbitals are the contraction for an orbital and a spin quantum number, as explained in A, so that:

$$i = s_i \sigma_i; \quad j = s_j \sigma_j; \quad m = s_m \sigma_m; \quad n = s_n \sigma_n. \quad (1.9)$$

From (1.8), because the interaction is independent of spin ( $v(\mathbf{x}, \mathbf{x}') = v(\mathbf{r}, \mathbf{r}')$ ), we conclude that  $v_{ijmn}$  is zero if  $\sigma_j \neq \sigma_m$  or  $\sigma_i \neq \sigma_n$ . Thus, (1.7), being  $\sigma_i = \sigma_n = \sigma$  and  $\sigma_j = \sigma_m = \sigma'$ , reduces to:

$$\hat{H}_{int} = \frac{1}{2} \sum_{\substack{s_i s_j s_m s_n \\ \sigma \sigma'}} v_{s_i s_j s_m s_n} \hat{d}_{s_i \sigma}^\dagger \hat{d}_{s_j \sigma'}^\dagger \hat{d}_{s_m \sigma'} \hat{d}_{s_n \sigma} \quad (1.10)$$

where we have expanded the spin-orbital quantum numbers as in (1.9). The interacting part is not quadratic in the creation and annihilation  $\hat{d}$ -operators, because it's not a one-body operator, but a two-body one, and an approximation is needed. In this case, the one used is the Hartree-Fock approximation, but any mean-field approximation, as is the case of DFT, works in the same manner. The approximation will be developed in section 1.3.

It's easy to rewrite the noninteracting part of the Hamiltonian in first quantization  $\hat{\mathcal{H}}_0$  as:

$$\begin{aligned} \hat{\mathcal{H}}_0 = & \underbrace{\sum_{\substack{mn \\ \sigma_m = \sigma_n}} H_{\alpha k}^C |m\rangle \langle n|}_{\text{central region}} + \underbrace{\sum_{\alpha k} \epsilon_{\alpha k} |\alpha k\rangle \langle \alpha k|}_{\text{reservoirs}} \\ & + \underbrace{\sum_{\substack{m, \alpha k \\ \sigma_m = \sigma_{\alpha k}}} (T_{m \alpha k} |m\rangle \langle \alpha k| + T_{\alpha k m} |\alpha k\rangle \langle m|)}_{\text{coupling}} \end{aligned} \quad (1.11)$$

The interaction part in first quantization can be rewritten as:

$$\hat{\mathcal{H}}_{int} = \frac{1}{2} \sum_{\substack{ijmn \\ \sigma_i = \sigma_n \\ \sigma_j = \sigma_m}} v_{ijmn} |i, j\rangle \langle n, m| \quad (1.12)$$

## 1.2 GREEN'S FUNCTION

The central quantity of our formalism is the one-body Green's function, whose corresponding operator in Second Quantization is given by the next expression in terms of the second quantization Lippmann-Schwinger operators, which diagonalize the full Hamiltonian of the entire problem:

$$\hat{G}_1(\mathbf{x}, z; \mathbf{x}', z') = \frac{1}{i} \mathcal{T} \left\{ \hat{\psi}_H(\mathbf{x}, z) \hat{\psi}_H^\dagger(\mathbf{x}', z') \right\} \quad (1.13)$$

Where the time-contour ordering operator  $\mathcal{T}$  orders the operators according to the Keldysh contour (Stefanucci & Van Leeuwen, 2010). Variable  $\mathbf{x}$  denotes the position-spin coordinate so that  $(\mathbf{x}) = (\mathbf{x}, \sigma)$ . From now on, subscript 1 of the Green's function will be suppressed.

The form of the Green's function suitable for the calculations, however, is given by its grand canonical ensemble average along the Keldysh contour:

$$\begin{aligned}
G(\mathbf{x}, z; \mathbf{x}', z') &\equiv \frac{\text{Tr} \left[ e^{-\beta \hat{H}^M} \hat{G}(\mathbf{x}, z; \mathbf{x}', z') \right]}{\text{Tr} \left[ e^{-\beta \hat{H}^M} \right]} \\
&= \frac{1}{i} \frac{\text{Tr} \left[ \mathcal{T} \left\{ e^{-i \int_{\gamma^M} d\bar{z} \hat{H}(\bar{z})} \hat{\psi}_{k\sigma, H}(\mathbf{x}, z) \hat{\psi}_{k\sigma, H}^\dagger(\mathbf{x}', z') \right\} \right]}{\text{Tr} \left[ e^{-\beta \hat{H}^M} \right]}
\end{aligned} \tag{1.14}$$

The statistical average performed after the second equality in (1.2) is explained in appendix H.1 (see equation (H.19)).

In the case of the field operators we know that they are constant over the entire contour  $\gamma^M$  (fig. H.1 based on the theory in (Stefanucci & Van Leeuwen, 2010)), which means:

$$\hat{\psi}(\mathbf{x}, z \in \gamma^M) = \hat{\psi}(\mathbf{x}); \quad \hat{\psi}^\dagger(\mathbf{x}, z \in \gamma^M) = \hat{\psi}^\dagger(\mathbf{x}); \tag{1.15}$$

Taking into account the (anti)commutation relation for the scattering state operators:

$$\left[ \hat{\psi}(\mathbf{x}), \hat{\psi}^\dagger(\mathbf{x}') \right]_{\mp} = \delta(\mathbf{x} - \mathbf{x}') \tag{1.16}$$

Looking at the first line in equation (1.3) and setting  $\mathbf{x}' = x$ ,  $z' = z^+$ , we can write the average of the density operator  $n(\mathbf{x}, z) = \pm i G(\mathbf{x}, z; \mathbf{x}, z^+)$ :

$$n(\mathbf{x}, z) = \frac{\text{Tr} \left[ e^{-\beta \hat{H}^M} \hat{\psi}_H^\dagger(\mathbf{x}, z^+) \hat{\psi}_H(\mathbf{x}, z) \right]}{\text{Tr} \left[ e^{-\beta \hat{H}^M} \right]} \tag{1.17}$$

and, based on the form of the current operator:

$$\hat{j}(\mathbf{x}, z) = \frac{1}{2m} \left[ \hat{\psi}^\dagger(\mathbf{x}, z) \left( \nabla \hat{\psi}(\mathbf{x}, z) \right) - \left( \nabla \hat{\psi}^\dagger(\mathbf{x}, z) \right) \hat{\psi}(\mathbf{x}, z) \right] \tag{1.18}$$

it's ensemble average results in:

$$\begin{aligned}
\vec{j}(\mathbf{x}, z) &= \frac{\text{Tr} \left[ e^{-\beta \hat{H}^M} \hat{j}(\mathbf{x}, z) \right]}{\text{Tr} \left[ e^{-\beta \hat{H}^M} \right]} \\
&= \pm \left( \frac{\nabla - \nabla'}{2m} G(\mathbf{x}, z; \mathbf{x}', z^+) \right) \Big|_{\mathbf{x}'=x}
\end{aligned} \tag{1.19}$$

Expression (1.5) is useful to write the Green's function operator in first quantization, which will be denoted with calligraphic letters,  $\hat{\mathcal{G}}(z, z')$  as:

$$\hat{\mathcal{G}}(z, z') = \int dx d\mathbf{x}' |\mathbf{x}\rangle G(\mathbf{x}, z; \mathbf{x}', z') \langle \mathbf{x}'| \quad (1.20)$$

where the matrix elements of  $\hat{\mathcal{G}}(z, z')$  are:

$$\langle \mathbf{x} | \hat{\mathcal{G}}(z, z') | \mathbf{x}' \rangle = G(\mathbf{x}, z; \mathbf{x}', z') \quad (1.21)$$

In the general basis, which can be typically an LCAO, the element  $j, i$  of the Green's function is calculated as:

$$G_{ji}(z, z') = \frac{1}{i} \frac{\text{Tr} \left[ e^{-\beta \hat{H}^M} \mathcal{T} \left\{ \hat{d}_{j,H}(z) \hat{d}_{i,H}^\dagger(z') \right\} \right]}{\text{Tr} \left[ e^{-\beta \hat{H}^M} \right]} \quad (1.22)$$

It's remarkable that both expressions of the Green's function, the Lippmann-Schwinger scattering eigenstates based  $G(\mathbf{x}, z; \mathbf{x}', z')$  in (1.14) and the general basis based  $G_{ji}(z, z')$  in (1.22) represent just different matrix elements of the Green's function operator in first quantization  $\hat{\mathcal{G}}(z, z')$ . When expanding the Lippmann-Schwinger operators in  $G(\mathbf{x}, z; \mathbf{x}', z')$ :

$$\begin{aligned} G(\mathbf{x}, z; \mathbf{x}', z') &= \sum_{ji} \varphi_j(\mathbf{x}) G_{ji}(z, z') \varphi_i^*(\mathbf{x}') \\ &= \sum_{ji} \langle \mathbf{x} | j \rangle G_{ji}(z, z') \langle i | \mathbf{x}' \rangle \end{aligned} \quad (1.23)$$

which, compared with (1.11), reveals:

$$\hat{\mathcal{G}}(z, z') = \sum_{ji} |j\rangle G_{ji}(z, z') \langle i| \quad (1.24)$$

and

$$\langle j | \hat{\mathcal{G}}(z, z') | i \rangle = G_{ji}(z, z') \quad (1.25)$$

Because of the generality of the expressions, it is preferable to work with operator  $\hat{\mathcal{G}}(z, z')$  than with its matrix elements in the basis of the  $\hat{\psi}$ -operators or the  $\hat{d}$ -operators, to leave the equations invariant and avoid these to depend on the representation. If we take the equations of motion of  $G$ , known as Kadanoff-Baym Equations (Stefanucci & Van Leeuwen, 2010; Myöhänen, Stan, Stefanucci, & Van

Leeuwen, 2009), for noninteracting (and interacting) particles extracted from the Martin-Schwinger hierarchy:

$$\begin{aligned} \iota \frac{d}{dz_1} G(\mathbf{x}_1, z_1; \mathbf{x}_2, z_2) - \int d\mathbf{x}_3 dz_3 h(\mathbf{x}_1, z_1; \mathbf{x}_3 z_3) G(\mathbf{x}_3, z_3; \mathbf{x}_2, z_2) \\ = (\delta(\mathbf{x}_1 - \mathbf{x}_2) \delta(z_1, z_2)) \end{aligned} \quad (1.26)$$

$$\begin{aligned} -\iota \frac{d}{dz_2} G(\mathbf{x}_1, z_1; \mathbf{x}_2, z_2) - \int d\mathbf{x}_3 dz_3 G(\mathbf{x}_1, z_1; \mathbf{x}_3 z_3) h(\mathbf{x}_3, z_3; \mathbf{x}_2, z_2) \\ = (\delta(\mathbf{x}_1 - \mathbf{x}_2) \delta(z_1, z_2)) \end{aligned} \quad (1.27)$$

where  $h(\mathbf{x}_1, z_1; \mathbf{x}_3 z_3) \equiv \delta(z_1, z_2) \langle \mathbf{x}_1 | \hat{h}(z_1) | \mathbf{x}_2 \rangle$ . Equations (1.26) and (1.27) are the expression in the position-spin representation of the more general operator equations:

$$\left[ \iota \frac{d}{dz_1} - \hat{h}(z_1) \right] \hat{G}(z_1, z_2) = \delta(z_1, z_2) \quad (1.28)$$

and

$$\hat{G}(z_1, z_2) \left[ -\iota \overleftarrow{\frac{d}{dz_2}} - \hat{h}(z_2) \right] = \delta(z_1, z_2) \quad (1.29)$$

The procedure to convert the equations of motion to the operator form as in equations (1.28) and (1.29) is general, so that one can construct the operator in first quantization for the  $n$ -particle Green's function, as we do for the two-body Green's function  $G_2$  in section 1.3.

Because we are interested in the time-dependent ensemble average of one-body operators, the time evolution of any of these is described by the real-time-axis defined lesser Green's function, with  $t' > t$ :

$$G_{ji}^<(t, t') = \mp \iota \frac{\text{Tr} \left[ e^{-\beta \hat{H}^M} \hat{d}_{i,H}^\dagger(t') \hat{d}_{j,H}(t) \right]}{\text{Tr} \left[ e^{-\beta \hat{H}^M} \right]} = \mp \iota \sum_k \rho_k \langle \Psi_k | \hat{d}_{i,H}^\dagger(t') \hat{d}_{j,H}(t) | \Psi_k \rangle \quad (1.30)$$

where the  $\mp$  sign stands for bosons/fermions, and the  $|\Psi_k\rangle$ 's are the quasi-particle eigenstates of the interacting Hamiltonian explained in next section. The real time  $\hat{d}$ -operators are in the Heisenberg picture instead of the Keldysh contour one.

### 1.3 MEAN FIELD THEORY: HARTREE-FOCK METHOD

Mean Field Theories have an associated Kadanoff-Baym Equation for the Green's Function. All the results described for the Hartree-Fock Method are general for Mean

Field Theories and have their corresponding counterparts with more sophisticated DFT functionals.

Interparticle interactions correlate the motion of a particle to the motion of all the other ones. For the two-body interactions considered in equation (1.10), at most two particles change their state. Under this approximation, a particle can scatter at most with another particle and, after the scattering event, the two particles end up in new states.

If the Hamiltonian includes interactions up to only two-body ones, as is the case of (1.10), the two particles whose interaction is represented by  $\hat{G}_2(\mathbf{x}_1, z_1, \mathbf{x}_2, z_2; \mathbf{x}'_1, z'_1, \mathbf{x}'_2, z'_2)$  feel the presence of all other particles but they are insensitive to their mutual position. Then, the probability amplitude for the first particle to go from  $(\mathbf{x}'_1; \mathbf{1}, z'_1)$  to  $(\mathbf{x}_1, z_1)$  and the second particle to go from  $(\mathbf{x}'_2; \mathbf{2}, z'_2)$  to  $(\mathbf{x}_2, z_2)$  is simply the product of the probability amplitudes of the two separate events.

The interacting part  $\hat{H}_{int}$  (equation (1.10)) of the Hamiltonian is not a one-body operator. However, there exist different mean-field approximations which allow to get suitable single-particle expressions, as is the case of Hartree-Fock.

In E we show that the ensemble average of the interaction part of the Hamiltonian is proportional to the two-body Green's function  $G_2(\mathbf{x}_1, z_1, \mathbf{x}_2, z_2; \mathbf{x}'_1, z'_1, \mathbf{x}'_2, z'_2)$ . We now want to develop a suitable approximation to treat the two-body interaction part as a one-body operator. Similar to the noninteracting equations 1.26 and 1.27, the Kadanoff-Baym equations for the one-body Green's function  $G(\mathbf{x}_1, z_1; \mathbf{x}_2, z_2)$  of interacting systems are (Myöhänen et al., 2009; Stefanucci & Van Leeuwen, 2010):

$$\begin{aligned} \left[ i \frac{d}{dz_1} - h(\mathbf{x}_1, z_1) \right] G(\mathbf{x}_1, z_1; \mathbf{x}_2, z_2) &= (\delta(\mathbf{x}_1 - \mathbf{x}_2) \delta(z_1, z_2)) \\ &\pm i \int d\mathbf{x}_3 dz_3 v(\mathbf{x}_1, z_1; \mathbf{x}_3, z_3) G_2(\mathbf{x}_1, z_1, \mathbf{x}_3, z_3; \mathbf{x}_2, z_2, \mathbf{x}_3, z_3^+) \end{aligned} \quad (1.31)$$

$$\begin{aligned} G(\mathbf{x}_1, z_1; \mathbf{x}_2, z_2) \left[ -i \frac{\overleftarrow{d}}{dz_2} - h(\mathbf{x}_2, z_2) \right] &= (\delta(\mathbf{x}_1 - \mathbf{x}_2) \delta(z_1, z_2)) \\ &\pm i \int d\mathbf{x}_3 dz_3 v(\mathbf{x}_2, z_2; \mathbf{x}_3, z_3) G_2(\mathbf{x}_1, z_1, \mathbf{x}_3, z_3^-; \mathbf{x}_2, z_2, \mathbf{x}_3, z_3) \end{aligned} \quad (1.32)$$

where both the zero-body Green's function  $G_0 \equiv \mathbb{1}$  (multiplying the  $(\delta(\mathbf{x}_1 - \mathbf{x}_2) \delta(z_1, z_2))$ ) and the two-body Green's function  $G_2$  appear, as stated by the Martin-Schwinger Hierarchy for the one-body Green's function  $G_1$ .

The Hartree-Fock Method approximates the two-body Green's functions presents in (1.31) and (1.32) by one-body Green's functions. Inserting approximation (1.33)

into the equations of motion (1.31) and (1.32), we get (1.34) and (1.35), which do not depend anymore on the two-body Green's function:

$$\begin{aligned} G_2(\mathbf{x}_1, z_1, \mathbf{x}_2, z_2; \mathbf{x}'_1, z'_1, \mathbf{x}'_2, z'_2) &\sim G_{2,HF}(\mathbf{x}_1, z_1, \mathbf{x}_2, z_2; \mathbf{x}'_1, z'_1, \mathbf{x}'_2, z'_2) \\ &\equiv G(\mathbf{x}_1, z_1; \mathbf{x}'_1, z'_1)G(\mathbf{x}_2, z_2; \mathbf{x}'_2, z'_2) \pm G(\mathbf{x}_1, z_1; \mathbf{x}'_2, z'_2)G(\mathbf{x}_2, z_2; \mathbf{x}'_1, z'_1) \end{aligned} \quad (1.33)$$

$$\begin{aligned} \left[ i \frac{d}{dz_1} - h(\mathbf{x}_1, z_1) \right] G(\mathbf{x}_1, z_1; \mathbf{x}_2, z_2) &= (\delta(\mathbf{x}_1 - \mathbf{x}_2)\delta(z_1, z_2)) \\ &+ \int d\mathbf{x}_3 dz_3 \Sigma(\mathbf{x}_1, z_1; \mathbf{x}_3, z_3) G(\mathbf{x}_3, z_3; \mathbf{x}_2, z_2) \end{aligned} \quad (1.34)$$

$$\begin{aligned} G(\mathbf{x}_1, z_1; \mathbf{x}_2, z_2) \left[ -i \frac{\overleftarrow{d}}{dz_2} - h(\mathbf{x}_2, z_2) \right] &= (\delta(\mathbf{x}_1 - \mathbf{x}_2)\delta(z_1, z_2)) \\ &+ \int d\mathbf{x}_3 dz_3 G(\mathbf{x}_2, z_2; \mathbf{x}_3, z_3) \Sigma(\mathbf{x}_3, z_3; \mathbf{x}_2, z_2) \end{aligned} \quad (1.35)$$

where the  $\pm$  sign in (1.33) stands for bosons/fermions. We have implicitly defined the self-energy  $\Sigma$ :

$$\begin{aligned} \Sigma(\mathbf{x}_1, z_1; \mathbf{x}_3, z_3) &= (\delta(\mathbf{x}_1 - \mathbf{x}_3)\delta(z_1, z_3))qV_H(\mathbf{x}_1, z_1) \\ &+ w(\mathbf{x}_1, z_1; \mathbf{x}_3, z_3)G(\mathbf{x}_1, z_1; \mathbf{x}_3, z_3^+) \end{aligned} \quad (1.36)$$

with

$$\begin{aligned} V_H(\mathbf{x}_1, z_1) &= \pm \frac{v}{q} \int d\mathbf{x}_3 dz_3 v(\mathbf{x}_1, z_1; \mathbf{x}_3, z_3) G(\mathbf{x}_3, z_3; \mathbf{x}_3, z_3^+) \\ &= \int d\mathbf{x}_3 v(\mathbf{x}_1, \mathbf{x}_3, z_1) n(\mathbf{x}_3, z_1) \end{aligned} \quad (1.37)$$

where we use  $v(\mathbf{x}_1, z_1; \mathbf{x}_3, z_3) = \delta(z_1, z_3)v(\mathbf{x}_1, \mathbf{x}_3, z_1)$  and  $\pm iG(\mathbf{x}_3, z_1; \mathbf{x}_3, z_3^+) = n(\mathbf{x}_3, z_1)$ , the density at point  $\mathbf{x}_3$  in the position-spin representation and at time  $z_1$  in the Keldysh contour.

Inserting (1.37) in the equation of motion for the Green's function (Stefanucci & Van Leeuwen, 2010):

$$\begin{aligned}
 & i \frac{d}{dz_1} G(\mathbf{x}_1, z_1; \mathbf{x}_2, z_2) \\
 & - \int d\mathbf{x}_3 dz_3 [h(\mathbf{x}_1, z_1; \mathbf{x}_3, z_3) + qV_H(\mathbf{x}_1, z_1)(\delta(\mathbf{x}_1 - \mathbf{x}_3)\delta(z_1, z_3)) \\
 & + v(\mathbf{x}_1, z_1; \mathbf{x}_3, z_3)G(\mathbf{x}_1, z_1; \mathbf{x}_3, z_3^+)] G(\mathbf{x}_3, z_3; \mathbf{x}_2, z_2) \\
 & = i \frac{d}{dz_1} G(\mathbf{x}_1, z_1; \mathbf{x}_2, z_2) - \int d\mathbf{x}_3 dz_3 [h(\mathbf{x}_1, z_1; \mathbf{x}_3, z_3) \\
 & + \Sigma(\mathbf{x}_1, z_1; \mathbf{x}_3, z_3^+)] G(\mathbf{x}_3, z_3; \mathbf{x}_2, z_2) = (\delta(\mathbf{x}_1 - \mathbf{x}_2)\delta(z_1, z_2))
 \end{aligned} \tag{1.38}$$

simplified by the use of the self-energy as:

$$\text{with } \Sigma(\mathbf{x}_1, z_1; \mathbf{x}_3, z_3^+) = \delta(z_1, z_3)E(\mathbf{x}_1, \mathbf{x}_3, z_1).$$

We have to notice that the quantity

$$qV_H(\mathbf{x}_1, z_1)(\delta(\mathbf{x}_1 - \mathbf{x}_3)\delta(z_1, z_3)) \tag{1.39}$$

is local both in time and space, while the quantity

$$\begin{aligned}
 & v(\mathbf{x}_1, z_1; \mathbf{x}_3, z_3)G(\mathbf{x}_1, z_1; \mathbf{x}_3, z_3^+) \\
 & = \delta(z_1, z_3)v(\mathbf{x}_1, \mathbf{x}_3)G(\mathbf{x}_1, z_1; \mathbf{x}_3, z_3^+)
 \end{aligned} \tag{1.40}$$

is local in time (because of the  $\delta$ -function) but is not local in space. However, this supposes no additional complication for the equivalence with the noninteracting Green's function. Defining the Hartree-Fock potential as:

$$\begin{aligned}
 V_{HF}(\mathbf{x}_1, \mathbf{x}_2, z) & = \left[ \delta(\mathbf{x}_1 - \mathbf{x}_2)V_H(\mathbf{x}_1, z) + \frac{i}{q}v(\mathbf{x}_1, \mathbf{x}_2)G(\mathbf{x}_1, z; \mathbf{x}_2, z^+) \right] \\
 & = \frac{1}{q} \left[ \delta(\mathbf{x}_1 - \mathbf{x}_2) \int dx v(\mathbf{x}_1, x)n(\mathbf{x}, z) \pm v(\mathbf{x}_1, \mathbf{x}_2)n(\mathbf{x}_1, \mathbf{x}_2, z) \right]
 \end{aligned} \tag{1.41}$$

where

$$n(\mathbf{x}_1, \mathbf{x}_2, z) = \pm iG(\mathbf{x}_1, z; \mathbf{x}_2, z^+) \tag{1.42}$$

is the time-dependent one-particle density matrix, where the  $\pm$  sign stands for bosons/fermions. Introducing, also, the Hartree-Fock potential operator in first quantization:

$$\hat{V}_{HF}(z) = \int d\mathbf{x}_1 d\mathbf{x}_2 |\mathbf{x}_1\rangle V_{HF}(\mathbf{x}_1, \mathbf{x}_2, z) \langle \mathbf{x}_2| \tag{1.43}$$

concluding that (1.41) is the matrix element (1, 2) in the position representation by bracketing between  $\langle \mathbf{x}_1 |$  and  $|\mathbf{x}_2\rangle$  of:

$$\left[ i \frac{d}{dz_1} - \hat{h}(z_1) - q \hat{\mathcal{V}}_{HF}(z_1) \right] \hat{\mathcal{G}}(z_1, z_2) = \delta(z_1, z_2) \quad (1.44)$$

which has exactly the same structure as the equation of motion of a noninteracting Green's function. This is a completely general result: given an equation of the form (1.38).

Now we are able to define the operator:

$$\hat{\mathcal{E}} = \int d\mathbf{x}_1 d\mathbf{x}_2 |\mathbf{x}_1\rangle E(\mathbf{x}_1, \mathbf{x}_3, z_1) \langle \mathbf{x}_2| \quad (1.45)$$

and comparing with (1.38), which is the bracket with  $\langle \mathbf{x}_1 |$  and  $|\mathbf{x}_2\rangle$  of the extended interacting version of the noninteracting (1.28) with the interaction operator in (1.43):

$$\left[ i \frac{d}{dz_1} - \hat{h}(z_1) - \hat{\mathcal{E}}(z_1) \right] \hat{\mathcal{G}}(z_1, z_2) = \delta(z_1, z_2) \quad (1.46)$$

More generally, any approximation to  $G_2$  leading to an equation like (1.46) is a mean-field approximation, which discards the direct interaction between the particles. The corresponding mean-field  $G$  has the same structure as that of a noninteracting  $G$ . This fact allows us to extend the results of (P. Hyldgaard, 2012; Per Hyldgaard, 2008) for the nonequilibrium statistical operator in noninteracting systems to interacting systems under a mean-field approximation, local in time, as is the case of Hartree-Fock or DFT.

As we noticed in the first paragraph of this chapter, the interacting potential operator  $\hat{\mathcal{E}}$  has a sufficiently general form to encompass any Mean Field Theory, as is the case of DFT, not only Hartree-Fock.

## 1.4 STEADY-STATE FORMALISM

### 1.4.0.1 Equations of motion

For steady state, which we consider here, the Green's functions depend only on the time difference  $t - t'$ , which we can Fourier transform to energy. By Fourier transforming (1.34), under the steady-state condition, we get the Keldysh-Kadanoff-Baym equation of motion for the Green's function in the energy (or frequency) domain:

$$[E - h(\mathbf{x}_1)]G^R(\mathbf{x}_1, \mathbf{x}_2; E) = + \int d\mathbf{x}_3 \Sigma^R(\mathbf{x}_1, \mathbf{x}_3; E)G^R(\mathbf{x}_3, \mathbf{x}_2; E) + \delta(\mathbf{x}_1 - \mathbf{x}_2) \quad (1.47)$$

and from reference (Myöhänen et al., 2009) we also have the Keldysh-Kadanoff-Baym equation of motion for the lesser Green's function:

$$\begin{aligned} [E - h(\mathbf{x}_1)] G^<(\mathbf{x}_1, \mathbf{x}_2; E) - \int d\mathbf{x}_3 \Sigma^R(\mathbf{x}_1, \mathbf{x}_3; E) G^<(\mathbf{x}_3, \mathbf{x}_2; E) \\ = \int d\mathbf{x}_3 \Sigma^<(\mathbf{x}_1, \mathbf{x}_3; E) G^A(\mathbf{x}_3, \mathbf{x}_2; E) \end{aligned} \quad (1.48)$$

By expanding the operator equation (H.11) in the position representation, we get the equivalent integral formulation of (1.48), we have:

$$G^<(\mathbf{x}_1, \mathbf{x}_2; E) = \int d\mathbf{x}_3 \int d\mathbf{x}_4 G^R(\mathbf{x}_1, \mathbf{x}_3; E) \Sigma^<(\mathbf{x}_3, \mathbf{x}_4; E) G^A(\mathbf{x}_4, \mathbf{x}_2; E) \quad (1.49)$$

where the lesser self-energy is defined as:

$$\Sigma^<(\mathbf{x}_1, \mathbf{x}_3; E) = \mp i f(E - \mu) \Gamma(\mathbf{x}_1, \mathbf{x}_3; E) \quad (1.50)$$

where  $f$  is the Fermi distribution function and  $\bar{f}$  its complementary, defined in (H.6).

In Hartree-Fock the Keldysh-Kadanoff-Baym equation can be written by Fourier transforming equation (1.38)

$$\begin{aligned} \left[ E - \int d\mathbf{x}_3 (h(\mathbf{x}_1, \mathbf{x}_3; E) + \Sigma_{HF}(\mathbf{x}_1, \mathbf{x}_3; E)) \right] G(\mathbf{x}_1, \mathbf{x}_2; E) \\ - \int d\mathbf{x}_3 \Sigma_c^{R/A}(\mathbf{x}_1, \mathbf{x}_3; E) G(\mathbf{x}_3, \mathbf{x}_2; E) = \delta(\mathbf{x}_1 - \mathbf{x}_2) \end{aligned} \quad (1.51)$$

The Hartree-Fock self energy  $\Sigma_{HF}^{R/A}$ , derived from equations (1.41) and (1.43) is:

$$\Sigma_{HF}^{R/A}(\mathbf{x}_1, \mathbf{x}_2; E) = qV_{HF}(\mathbf{x}_1, \mathbf{x}_2) \quad (1.52)$$

in the long-time limit steady state the Hartree-Fock potential  $V_{HF}^{R/A}(\mathbf{x}_1, \mathbf{x}_2)$  does not depend on time nor energy, so does not the associated the self-energy. Because of its definition,  $\Sigma_{HF}$  is real.

The correlation self energy takes into account all the effects beyond Mean-Field (HF) and has the structure shown in (H.4) (Stefanucci & Van Leeuwen, 2010; Stefanucci & Almladh, 2004).

The embedding self-energy is not yet present, because it is an artifact of the partition, a tool to represent the effects of the leads connected to the central region  $C$ .

Equations (1.49) and (1.51) are the key ingredients to solve the steady state transport problem in quantum devices. However, the position-spin representation is not the most tractable.

## 1.4.0.2 NEGF Transport matrix formulation

Changing the basis from the position-spin representation to the general basis of the  $\varphi(\mathbf{x})$  as in (1.13), the Green's function matrix in the frequency (or energy) domain satisfies the matrix equation:

$$\sum_k (E^+ S_{ik} - H_{ik}) G_{kj}^R(E) = \delta_{ij} \quad (1.53)$$

where  $E^+ = E + i\eta$  where  $\eta$  is a positive infinitesimal and where the quantity  $S_{ik}$  is introduced multiplying the energy eigenvalue  $E$  because of the generalization of the eigenvalue problem to a nonorthogonal basis. We have implicitly defined the overlap matrix elements  $S_{ik}$  for nonorthogonal basis, which is the case for LCAO:

$$S_{ij} = \int d^3r \varphi_i^*(\mathbf{x}) \varphi_j(\mathbf{x}) \quad (1.54)$$

Equation (1.53) involves infinite matrix whose elements are the matrix ones in the basis formed by the orbital functions  $\varphi(\mathbf{x})$ , which in our case correspond to a linear combination of atomic orbitals (LCAO). By partitioning the space into a central region  $C$  and different electrodes connected to it and disconnected between them, following the Caroli partition scheme (Datta, 1995; Caroli et al., 1971), we represent the Hamiltonian in equation (1.4) as a block partitioned matrix:

$$H = \begin{pmatrix} H_{11} & 0 & 0 & \dots & H_{1C} \\ 0 & H_{22} & 0 & \dots & H_{2C} \\ 0 & 0 & H_{33} & \dots & H_{3C} \\ \cdot & \cdot & \cdot & \cdot & \cdot \\ \cdot & \cdot & \cdot & \cdot & \cdot \\ \cdot & \cdot & \cdot & \cdot & \cdot \\ H_{C1} & H_{C2} & H_{C3} & \dots & H_{CC} \end{pmatrix} \quad (1.55)$$

In the same way as the Hamiltonian, the self-energy and the Green's function matrices are also partitioned in blocks for the central region  $C$  and the reservoirs labelled  $\alpha = 1, 2, \dots$ . Each block is a matrix, and corresponds to the projection of the full matrix onto the subspace of localized functions  $\varphi_i(\mathbf{x})$  for this reservoir or onto the subspace of the central region  $C$ .

For practical purposes, in this section we will restrict the problem to the case of two reservoir electrodes  $L/R$ , which is the minimum example to illustrate the nonequilibrium quantum transport physics. The Hamiltonian (1.55) results:

$$H = \begin{pmatrix} H_{LL} & H_{LC} & H_{LR} \\ H_{CL} & H_{CC} & H_{CR} \\ H_{RL} & H_{RC} & H_{RR} \end{pmatrix} \quad (1.56)$$

Rewriting (1.53) in matrix form:

$$\begin{pmatrix} E^+ S_{LL} - H_{LL} & E^+ S_{LC} - H_{LC} & E^+ S_{LR} - H_{LR} \\ E^+ S_{CL} - H_{CL} & E^+ S_{CC} - H_{CC} & E^+ S_{CR} - H_{CR} \\ E^+ S_{RL} - H_{RL} & E^+ S_{RC} - H_{RC} & E^+ S_{RR} - H_{RR} \end{pmatrix} \times \begin{pmatrix} G_{LL}^R & G_{LC}^R & G_{LR}^R \\ G_{CL}^R & G_{CC}^R & G_{CR}^R \\ G_{RL}^R & G_{RC}^R & G_{RR}^R \end{pmatrix} = \begin{pmatrix} \mathbb{1}_{LL} & 0 & 0 \\ 0 & \mathbb{1}_{CC} & 0 \\ 0 & 0 & \mathbb{1}_{RR} \end{pmatrix} \quad (1.57)$$

Typically the inter-electrode blocks of the Hamiltonian and the overlap matrices  $H_{LR}$ ,  $H_{RL}$ ,  $S_{LR}$  and  $S_{RL}$  are negligible, and thus the solution for the matrix Green's function  $G_{CC}^R$  results:

$$G_{CC}^R = \frac{1}{[E^+ S_{CC} - H_{CC} - \Sigma_L^R(E) - \Sigma_R^R(E)]} \quad (1.58)$$

where the quantity  $S_{CC}$  is introduced multiplying the energy eigenvalue  $E$ , as in (1.53), because of the generalization of the eigenvalue problem to a nonorthogonal basis. The embedding self-energies are the expansions in the  $\varphi_i(\mathbf{x})$  orbitals of the operators in (F.27):

$$\begin{aligned} \Sigma_L^R(E) &= (E^+ S_{CL} - H_{CL}) g_{LL}^R (E^+ S_{LC} - H_{LC}) \\ \Sigma_R^R(E) &= (E^+ S_{CR} - H_{CR}) g_{RR}^R (E^+ S_{RC} - H_{RC}) \end{aligned} \quad (1.59)$$

where the unperturbed Green's functions of the leads is the conversion to a nonorthogonal basis of (F.21):

$$\begin{aligned} g_{LL}^R &= \frac{1}{[E^+ S_{LL} - H_{LL}]} \\ g_{RR}^R &= \frac{1}{[E^+ S_{RR} - H_{RR}]} \end{aligned} \quad (1.60)$$

Equation (1.60) expresses the Green's function in the molecule in terms of the Hamiltonian matrix elements in the same region, with the coupling to the left and right electrode included rigorously in terms of the self-energy operators  $\Sigma_L^R(E)$  and  $\Sigma_R^R(E)$ . Note again that due to the short-range nature of the basis set, only the finite block of  $g_{LL(RR)}^R$  is needed for the calculation of  $\Sigma_{L(R)}^R(E)$  corresponding to the orbital basis in the left(right) electrode that have non-negligible  $L(R)$  overlap with the orbital basis in the extended molecule. So the calculation of  $G_{CC}^R$  involves matrix operations only on finite matrices. The matrix self-energy operator can be taken as the matrix elements of a non-local operator in real space, as defined in equations (F.19) and (F.20).

As we have deduced in appendix F.1, the lesser/greater Green's function matrix is the representation in the general basis of the  $\varphi_i(\mathbf{x})$  of (F.25):

$$G^<(E) = G^R(E)\Sigma^<(E)G^A(E) \quad (1.61)$$

Because of the decomposition of the embedding self-energy between the different contacts defined in (F.18) and the definition for the reservoir  $\alpha$  lesser self-energy operator in (F.26), we can rewrite the lesser Green's function matrix as:

$$\Sigma^<(E) = \Sigma_L^<(E) + \Sigma_R^<(E) = i\Gamma_L(E)f(E - \mu_L) + i\Gamma_R(E)f(E - \mu_R) \quad (1.62)$$

since there is no “lesser” self-energy operator associated with V xc . And we can express the correlation function in terms of the distribution in each electrodes:

$$G^<(E) = i[G^R(E)\Gamma_L(E)G^A(E)]f(E - \mu_L) + i[G^R(E)\Gamma_R(E)G^A(E)]f(E - \mu_R) \quad (1.63)$$

where the products within the brackets are matrix products. Every physical observable of interest can be computed from the matrix correlation function  $G_{ij}^<$ .

But often it is more useful to compute the terminal current directly from the matrix Green's function and the matrix self-energy operators. This can be achieved by defining a current in the position representation, as in reference (Caroli et al., 1971):

$$I(\mathbf{x}, \mathbf{x}'; E) = \frac{e}{\hbar} [H(\mathbf{x}_1)G^<(\mathbf{x}_1, \mathbf{x}_2; E) - G^<(\mathbf{x}_2, \mathbf{x}_1; E)H(\mathbf{x}_2)] \quad (1.64)$$

whose diagonal elements give the divergence of the current density:

$$I(\mathbf{x}, \mathbf{x}; E) = \nabla \cdot \vec{J}(\mathbf{x}; E) \quad (1.65)$$

Converting from the position representation to the suitable matrix representation in the basis of the  $\varphi_i(\mathbf{x})$  orbitals:

$$I = \frac{e}{\hbar} \int dE [H, G^<]_- \quad (1.66)$$

Again we have made the transformation from the position representation to the general basis of the  $\varphi_i(\mathbf{x})$  operators, getting the matrix equation involving the Hamiltonian and correlation function matrices. From here on the usual derivation using the matrix notation, often used in second quantization, can be carried through without

change providing us the final form for the current through each terminal (Xue, Datta, & Ratner, 2002; Datta, 1995, 2005):

$$I_{L(R)} = \frac{e}{h} \int dE \text{Tr} [\Gamma_{L(R)} [f(E - \mu_{L(R)}) A(E) + iG^<(E)]] \quad (1.67)$$

where the replacement of the spectral function operator  $\hat{A}(E)$  by its definition in (F.24), expanded in the  $\varphi_i(\mathbf{x})$  basis, results in:

$$I_{L(R)} = \frac{e}{h} \int dE \text{Tr} [\Gamma_L(E) G^R(E) \Gamma_R(E) G^A(E)] [f(E - \mu_L) - f(E - \mu_R)] \quad (1.68)$$

where the rate operator matrices for both leads are:

$$\begin{aligned} \Gamma_L(E) &= i(\Sigma_L^R(E) - [\Sigma_L^R(E)]^\dagger), \\ \Gamma_R(E) &= i(\Sigma_R^R(E) - [\Sigma_R^R(E)]^\dagger) \end{aligned} \quad (1.69)$$

#### 1.4.1 Transient solution

The equal time lesser Green's function matrix (Stefanuucci & Van Leeuwen, 2010)

can be calculated from the matrix equations of motion (F.1) and (F.2) by setting  $z = t_-$  and  $z' = t'_+$ , subtracting the former from its adjoint, the latter, and setting  $t' = t$ :

$$\begin{aligned} i \frac{d}{dt} - [h(t), G^<(t, t)]_- \\ = [G^R \cdot \Sigma_{em}^< + G^< \cdot \Sigma_{em}^A + G^\dagger \star \Sigma_{em}^\dagger] (t, t) + \text{H.c.} \end{aligned} \quad (1.70)$$

where  $G^\dagger, \Sigma^\dagger$  are functions whose expressions are detailed in appendix H.

$$\begin{aligned} -iG^<(t, t) &= \int \frac{dE}{2\pi} f(E - \mu) \sum_\alpha \left\{ A_\alpha(E + V_\alpha) \right. \\ &+ V_\alpha \left[ e^{i(E+V_\alpha-h_{eff})t} G^R(E) A_\alpha(E + V_\alpha) + \text{H.c.} \right] + V_\alpha^2 e^{-ih_{eff}t} G^R(E) A_\alpha(E + V_\alpha) G^A(E) e^{ih_{eff}^\dagger t} \left. \right\} \end{aligned} \quad (1.71)$$

where  $h_{eff} = h + \Sigma_{em}$  and the partial spectral function  $A_\alpha(E)$  for each reservoir is

$$A_\alpha(E) = G^R(E) A_\alpha(E + V_\alpha) G^A(E), \quad (1.72)$$

satisfying

$$A(E) = \sum_{\alpha} A_{\alpha}(E). \quad (1.73)$$

## THEORY

## 2.1 ABSTRACT

Nonequilibrium Electron Transport through metallic contacts at the nanoscale has been studied theoretically and with experiments. However, not only Nonequilibrium Transport, but mechanical phenomena appear in such devices. These appear due to the exchange of particles with the reservoirs, tractable through the grand canonical ensemble[1]. If present, Nonequilibrium Quantum Transport also contributes to the forces on atoms, as is the case of Electromigration. These forces cause the transfer of atoms between metallic electrodes and surfaces mediated by an applied bias voltage (Salgado and Palacios, 2019).

## 2.2 INTRODUCTION

As we learned in freshman physics, specifically in Ch. 8 of Feynman's Lectures on Physics (Feynman, 1964), the force between the plates of an isolated parallel-plate condenser, with fixed charge in each plate, is equal to the change in electrostatic internal energy of the condenser, which is attractive because of the attraction of opposite charges:

$$U(Q) = \frac{Q^2}{2C}; \quad F\Delta z = -\frac{Q^2}{2C^2}\Delta C \quad (2.1)$$

where  $C$  is the capacitance and  $Q$  the charge on each plate. However, if the condenser is supposed to be held by a battery at a constant potential difference  $V$  between the plates, where the charge is not fixed anymore, but determined as  $Q = VC$ , the internal energy and the force become:

$$U(V) = \frac{CV^2}{2}; \quad F\Delta z = \frac{V^2}{2}\Delta C \quad (2.2)$$

where the force is repulsive, which must be wrong, and opposite to the one in (2.1). The error committed in (2.2) is that we have not taken into account the work done by the condenser on the battery. To keep the potential drop between the plates constant as these move, changing the capacitance, a charge  $\Delta Q = V\Delta C$  must be supplied to the condenser by the battery, at the potential of the electrodes, so that the work done by the condenser to keep the potential constant is  $W_e = V\Delta Q = V^2\Delta C$ . The

mechanical work  $W_m$  plus this electrical work  $W_e$  make the change in the particle exchanging open-system energy of the condenser:

$$\begin{aligned} W_m + W_e &= F\Delta z + V^2\Delta C = \frac{V^2}{2}\Delta C \\ F\Delta z &= -\frac{V^2}{2}\Delta C \end{aligned} \quad (2.3)$$

so that we recover the attractive force in (2.1). As we will see in next sections, something similar happens to quantum devices, not only with an applied bias voltage, but also with a temperature gradient between the electrodes.

The formulation of the problem rests on an open-boundary model described by the NEGF. We implemented this framework at the DFT level in a LCAO basis. The DFT-Hamiltonian for the infinite open system works as the Lippmann-Schwinger (LS) Hamiltonian in equation (2.7) for the scattering of electrons through the device, as described by Hyldgaard in references (Per Hyldgaard, 2008; P. Hyldgaard, 2012) following Herschfield's work in (Herschfield, 1993). The LS eigenstates diagonalizing (2.7) form the density matrix tractable through DFT. The open system boundary conditions allow the device to exchange electrons with the reservoirs. The grand canonical ensemble energy, whose negative gradient describes the forces (Eq.4), is the Grand Potential  $\Omega$  described in section 2.3.1, instead of the Internal Energy  $U$ , calculated from the Hamiltonian  $\hat{H}$ , valid for isolated systems.

The remaining question concerns the mechanism for the dissipation of this energy to occur. Instead of reproducing it by the creation of any phonons in the crystalline lattice, the work associated to the inelastic displacement of the atoms caused by the forces derived as the gradient of the canonical grand potential  $\Omega$  explains this dissipation.

## 2.3 EQUATIONS

### 2.3.1 Canonical Grand-Potential $\Omega$

The conversion between  $\hat{H}$  and  $\hat{\Omega}$  is performed as the classical Legendre transformation from the internal energy  $U(N, S)$  to the canonical grand-potential  $\Omega(\{\mu_\alpha\}, T)$  in equation (2.4)(P. Hyldgaard, 2012; Per Hyldgaard, 2008), where  $\alpha$  labels the different reservoirs connected to the system at a chemical potential  $\mu_\alpha$  and an inverse temperature  $\beta_\alpha = 1/(k_B T)$ , where  $k_B$  is the Boltzmann constant and  $T$  the temperature. Subtracting the Gibbs free energy  $Y = Y^Q + Y^E$ , given by the nonequilibrium statistical operator, also called Gibbs free energy operator,  $\hat{Y} = \hat{Y}^Q + \hat{Y}^E$ , where  $Q$  stands for charge and  $E$  for energy, described in section 2.3.2, we have:

$$\begin{aligned} \Omega(\{T_\alpha\}, \{\mu_\alpha\}) &= U(S, \{N_\alpha\}) \\ &\quad - Y^Q(\{\mu_\alpha\}, \{N_\alpha\}) - Y^E(\{T_\alpha\}, \{S_\alpha\}) \end{aligned} \quad (2.4)$$

where  $\alpha$  labels the different reservoirs connected to the system. In (2.4) there appear the common thermodynamic variables: chemical potential  $\mu$ , number of particles

$N$ , the temperature  $T$  and entropy  $S$ . The detailed structure of the energies  $Y^Q$  and  $Y^E$  will be discussed in section 2.3.2 from the structure of its associated operators.

It is important to notice that the canonical grand potential  $\Omega$  can't be calculated for infinite systems like the ones we are dealing with. Instead of it, grand potential energy variations  $\Delta\Omega$  appeared in the vicinity of the scattering region can be calculated. Only in the proximity of the scattering region the perturbations on the electronic density are considered to be non-negligible, and thus this grand potential differences are enough to reproduce the physics related to the scattering event.

The conversion to second quantization one-body operators:

$$\hat{\Omega} = \hat{H} - \hat{Y}^Q - \hat{Y}^E = \hat{H} - \hat{Y} \quad (2.5)$$

From now on, second quantization operators will be denoted with modern letters,  $\hat{Y}$ , while first quantization operators will be denoted by calligraphic ones,  $\hat{\mathcal{Y}}$ .

The energies are calculated as the ensemble averages of one-body operators described in equation (H.23) of appendix H.1.

$$\Omega = \langle \hat{\Omega} \rangle; \quad U = \langle \hat{H} \rangle; \quad Y = \langle \hat{Y} \rangle; \quad (2.6)$$

### 2.3.2 Nonequilibrium statistical operator

Throughout this work we always work with (non)interacting systems whose scattering Hamiltonian in second quantization can be expressed as a one-body operator, quadratic in the  $\hat{\psi}$ -operators for the scattering eigenstates which diagonalize it, as:

$$\hat{H}(\mathbf{x}', t'; \mathbf{x}, t) = \sum_{\alpha k \sigma} \epsilon_{\alpha k \sigma} \hat{\psi}_{\alpha k \sigma}^\dagger(\mathbf{x}, t) \hat{\psi}_{\alpha k \sigma}(\mathbf{x}', t') \quad (2.7)$$

where  $\alpha$  labels the different reservoirs from which electrons are injected, while  $k$  is a generic label for the eigenstates in each reservoir and  $\sigma$  separates both spin components.

On the basis for the one-body operators constituted by the Green's function, it is easy to write the nonequilibrium statistical operator or Gibbs Free Energy Operator for open systems which interchange particles with one or various reservoirs at a chemical potential  $\mu_\alpha$  (J. E. Han, 2007; J. E. Han & Heary, 2007; Dutt, Koch, Han, & Le Hur, 2011; Jong E. Han, Dirks, & Pruschke, 2012; Jong E. Han & Li, 2013). The calculation of thermodynamic forces rests on the derivatives of this operator:

$$\hat{Y}^Q(\mathbf{x}', t'; \mathbf{x}, t) = \sum_{\alpha k \sigma} \mu_\alpha \hat{\psi}_{\alpha k \sigma}^\dagger(\mathbf{x}, t) \hat{\psi}_{\alpha k \sigma}(\mathbf{x}', t') \quad (2.8)$$

In a similar fashion, it has been deduced (Ness, 2014, 2017) an expression for the nonequilibrium statistical operator  $\hat{Y}^E$  in the presence of a temperature gradient

between two electrodes  $L/R$ , which treats the energy flow between the electrodes instead of the particle interchange. Compared to (2.8), it becomes:

$$\hat{Y}^E(\mathbf{x}', t'; \mathbf{x}, t) = \sum_{\alpha k \sigma} \frac{\beta_\alpha - \langle \beta \rangle_C}{\langle \beta \rangle_C} \epsilon_{\alpha k \sigma} \hat{\psi}_{\alpha k \sigma}^\dagger(\mathbf{x}, t) \hat{\psi}_{\alpha k \sigma}(\mathbf{x}', t') \quad (2.9)$$

where the  $\epsilon_{\alpha k \sigma}$  are the energy eigenvalues of the particles deep inside each reservoir, as for the Hamiltonian,  $\beta_\alpha = 1/(k_B T_\alpha)$  is the inverse temperature at which the particles are injected from each reservoir  $\alpha$  and  $\langle \beta \rangle_C$  is the inverse temperature promediated in the central or scattering region by means of the central region  $C$  partial number of particles injected from each lead as described in equation (F.31) from section F.1:

$$\langle \beta \rangle_C = \frac{\sum_\alpha \beta_\alpha N_\alpha}{\sum_\alpha N_\alpha} \quad (2.10)$$

As suggested by Ness (Ness, 2014, 2017), in the presence of both, interchange of particles with the reservoirs and a temperature gradient between them, (2.8) has to be rewritten as:

$$\hat{Y}^Q(\mathbf{x}', t'; \mathbf{x}, t) = \sum_{\alpha k \sigma} \frac{\beta_\alpha}{\langle \beta \rangle_C} \mu_\alpha \hat{\psi}_{\alpha k \sigma}^\dagger(\mathbf{x}, t) \hat{\psi}_{\alpha k \sigma}(\mathbf{x}', t') \quad (2.11)$$

Of course, if there is no temperature gradient between the reservoirs, equation (2.11) reduces to (2.8).

As stated by Ness (Ness, 2014, 2017), at thermal equilibrium,  $\beta_\alpha = \langle \beta \rangle_C$  for all  $\alpha$  and thus,  $\hat{Y}^E$  vanishes. However, at chemical equilibrium, with a single chemical potential  $\mu_\alpha = \mu^{eq}$ ,  $\hat{Y}^Q$  does not vanish. It is important to recall that  $\hat{Y}^Q$  exists because of the presence of any particle reservoirs which provide particles at a fixed chemical potential, while  $\hat{Y}^E$  exists only because of the presence of a temperature gradient  $\beta_\alpha - \langle \beta \rangle_C$  between the reservoirs and the central or scattering region  $C$ .

From equations (2.7), (2.8), (2.9) and (2.11) we deduce that both  $\hat{Y}^Q$  and  $\hat{Y}^E$  commute with the Hamiltonian, since the three operators share the basis of the scattering eigenstates. The three operators are closely related to the density operators  $\hat{N}_\alpha(\mathbf{x}', t'; \mathbf{x}, t)$  of the number of particles injected from each lead  $\alpha$ :

$$\hat{N}_\alpha(\mathbf{x}', t'; \mathbf{x}, t) = \sum_{k \sigma} \hat{\psi}_{\alpha k \sigma}^\dagger(\mathbf{x}, t) \hat{\psi}_{\alpha k \sigma}(\mathbf{x}', t') \quad (2.12)$$

where the  $\hat{\psi}_{\alpha k \sigma}(\mathbf{x}', t')$  denote the eigenstates coming from reservoir  $\alpha$ , satisfying:

$$\hat{N} = \sum_\alpha \hat{N}_\alpha \quad (2.13)$$

When there is only a single reservoir with a common chemical potential  $\mu$  for the system molecule-reservoir, the expression (2.8) reduces to:

$$\hat{Y}^Q(\mathbf{x}', t'; \mathbf{x}, t) = \sum_{k\sigma} \mu \hat{\psi}_{k\sigma}^\dagger(\mathbf{x}, t) \hat{\psi}_{k\sigma}(\mathbf{x}', t') = \mu \hat{N}(\mathbf{x}', t'; \mathbf{x}, t) \quad (2.14)$$

while (2.9) vanishes, because  $\langle \beta \rangle_C = \beta$ :

$$\hat{Y}^E(\mathbf{x}', t'; \mathbf{x}, t) = \sum_{k\sigma} \frac{\beta - \langle \beta \rangle_C}{\langle \beta \rangle_C} \epsilon_{k\sigma} \hat{\psi}_{k\sigma}^\dagger(\mathbf{x}, t) \hat{\psi}_{k\sigma}(\mathbf{x}', t') = \hat{0} \quad (2.15)$$

From now on, the spin label  $\sigma$  will be neglected, but all operators may have two different spin components, for example  $\hat{Y} = \{\hat{Y}_+, \hat{Y}_-\}$ , which satisfy the same equations.

In first quantization, the number operator is related to the lesser Green's function as  $\hat{N}(\mathbf{x}, t) = \pm i \hat{\mathcal{G}}^<(t; t^+)$ . The lesser/greater Green's functions can be expressed in the position representation:

$$\hat{\mathcal{G}}^{\lessgtr}(t, t') = \int dx dx' |\mathbf{x}\rangle G^{\lessgtr}(\mathbf{x}, t; \mathbf{x}', t') \langle \mathbf{x}'| \quad (2.16)$$

or in the general basis representation:

$$\hat{\mathcal{G}}^{\lessgtr}(t, t^+) = \sum_{ji} |j\rangle G_{ji}^{\lessgtr}(t, t^+) \langle i| \quad (2.17)$$

Where the real time lesser/greater Green's function operator  $\hat{\mathcal{G}}^{\lessgtr}(t, t')$  in the steady-state long-time limit can be extracted from the convolution (Stefanucci & Almladh, 2004; Myöhänen et al., 2009; Stefanucci & Van Leeuwen, 2010)

$$\lim_{t, t' \rightarrow \infty} \hat{\mathcal{G}}^{\lessgtr}(t, t') = \int dt_1 dt_2 \hat{\mathcal{G}}^R(t, t_1) \Sigma^{\lessgtr}(t_1, t_2) \hat{\mathcal{G}}^A(t_2, t') \quad (2.18)$$

and setting  $t' = t^+$ . The lesser/greater self-energy  $\Sigma^{\lessgtr}(t_1, t_2)$  in equation (2.18) is defined in appendix F.1.

When Fourier transforming, because the convolution only depends on time differences, it reduces to a simple product of operators:

$$\hat{\mathcal{G}}^{\lessgtr}(E) = \hat{\mathcal{G}}^R(E) \Sigma^{\lessgtr}(E) \hat{\mathcal{G}}^A(E) \quad (2.19)$$

which can be rewritten as a sum of partial spectral lesser/greater Green's function operators as:

$$\begin{aligned}\hat{\mathcal{G}}^{\lessgtr}(E) &= \sum_{\alpha} \hat{\mathcal{G}}_{\alpha}^{\lessgtr}(E) \\ \hat{\mathcal{G}}_{\alpha}^{\lessgtr}(E) &= \hat{\mathcal{G}}^R(E) \hat{\Sigma}_{\alpha}^{\lessgtr}(E) \hat{\mathcal{G}}^A(E)\end{aligned}\quad (2.20)$$

This result is enough to calculate steady-state quantities, instead of solving the Kadanoff-Baym equations.

With operator  $\hat{\mathcal{Y}}$ , we get the key ingredient to calculate thermodynamic forces from now on. Because the nonequilibrium statistical operator for particle exchange  $\hat{\mathcal{Y}}^Q$  is proportional to the number operator corresponding to each reservoir:

$$\hat{\mathcal{Y}}^Q = \sum_{\alpha} \hat{\mathcal{Y}}_{\alpha}^Q = \sum_{\alpha} \frac{\beta_{\alpha}}{\langle \beta \rangle_C} \mu_{\alpha} \hat{n}_{\alpha} = \sum_{\alpha} \frac{\beta_{\alpha}}{\langle \beta \rangle_C} \mu_{\alpha} \int_{-\infty}^{\infty} dE \frac{1}{2\pi i} \hat{\mathcal{G}}_{\alpha}^{<}(E) \quad (2.21)$$

while the nonequilibrium statistical operator for heat exchange  $\hat{\mathcal{Y}}^E$  is:

$$\hat{\mathcal{Y}}^E = \sum_{\alpha} \hat{\mathcal{Y}}_{\alpha}^E = \sum_{\alpha} \frac{\beta_{\alpha} - \langle \beta \rangle_C}{\langle \beta \rangle_C} \int_{-\infty}^{\infty} E dE \frac{1}{2\pi i} \hat{\mathcal{G}}_{\alpha}^{<}(E) \quad (2.22)$$

and, of course:

$$\hat{\mathcal{Y}} = \hat{\mathcal{Y}}^Q + \hat{\mathcal{Y}}^E \quad (2.23)$$

Equations (2.23) for the nonequilibrium statistical operator is valid, not only for noninteracting systems (Per Hyldgaard, 2008; P. Hyldgaard, 2012), but for interacting ones under a mean-field description (Hartree-Fock, DFT), whose Green's function, after the self-consistency is reached, satisfies an equation of motion like (1.46) in appendix 1.3, analogous to the noninteracting (1.28), but including a one-body, local in time, approximation for the interactions.

Since the non-equilibrium density matrix is given by

$$\hat{\rho}^{ne} = \frac{1}{2\pi i} \int_{-\infty}^{\infty} dE \hat{\mathcal{G}}^{<}(E) \quad (2.24)$$

the non-equilibrium contributions to the grand canonical potential given by Eqs. (2.21) and (2.22) can now be calculated as

$$Y^Q = \sum_{\alpha} Y_{\alpha}^Q = \sum_{\alpha} \frac{\beta_{\alpha}}{\beta} \mu_{\alpha} \frac{1}{2\pi i} \int_{-\infty}^{\infty} dE \text{Tr} \left[ \hat{\mathcal{G}}_{\alpha}^{<}(E) \right], \quad (2.25)$$

$$Y^E = \sum_{\alpha} Y_{\alpha}^E = \sum_{\alpha} \frac{\beta_{\alpha} - \bar{\beta}}{\beta} \frac{1}{2\pi i} \int_{-\infty}^{\infty} dE E T r \left[ \hat{G}_{\alpha}^{<}(E) \right] \quad (2.26)$$

Here we have used the fact that

$$\hat{G}^{<} \hat{A}_{\alpha} = \hat{G}_{\alpha}^{<} \hat{A}_{\alpha} = \hat{G}_{\alpha}^{<}$$

which can be easily demonstrated taking into account that

$$\hat{G}_{\beta}^{<} \hat{A}_{\alpha}(E) = \delta_{\alpha\beta} \hat{G}_{\beta}^{<}(E)$$

and noting that  $\hat{G}_{\alpha}^{<}(E)$  is the projector on the occupied subspace of  $\hat{A}_{\alpha}(E)$ .

### 2.3.3 Forces

There are different methods to calculate forces on atoms in quantum chemistry and condensed matter physics. Using DFT-methods based on a linear combination of atomic orbitals (LCAO from now on) to describe the problem is a common practice, because of the dependence of the wavefunctions on the atomic coordinates. This dependence is propagated from the wavefunctions to the functional evaluations. Calculating the derivatives of the functionals with respect to the atomic coordinates is then reduced to a careful application of the chain rule. By doing this, the generalized gradient of the functional, also called the jacobian matrix (which has only one row or column), and the matrix of the second derivatives, the hessian matrix, can be calculated. The generalized gradient or jacobian in conjunction with the total energy (extracted from the grand potential  $\Omega$ ) are the key ingredients to perform DFT-based Molecular Dynamics calculations, by means of algorithms like BFGS (Peng, Ayala, Schlegel, & Frisch, 1996) or Berny (Vreven, Morokuma, Farkas, Schlegel, & Frisch, 2003). Eventually, the hessian matrix is useful to calculate transition geometries or saddle points.

If a LCAO is used to describe the operators in the DFT-calculation, the equilibrium positions of the total number  $P$  of atoms are calculated by minimizing functional  $\Omega(\beta, \mu)$  with respect to the basis centers, located on the atomic positions, instead of the internal energy  $U(S, N)$ , as for closed systems.

The  $3P$ -dimensional gradient of the  $\Omega$  functional gives the generalized grand canonical ensemble force  $\mathbf{F}_{\mathbf{R}_i}^{GCE}$  acting on atom  $i$  until they reach equilibrium, when the gradient or jacobian becomes vector  $\vec{0}$ . The force on atom  $i$  is the negative of the 3-D gradient  $\nabla_i = \frac{\partial}{\partial \mathbf{R}_i}$  with respect to the  $\mathbf{R}_i = (x_i, y_i, z_i)$  coordinates:

$$\begin{aligned} \mathbf{F}_{\mathbf{R}_i}^{GCE} &= - \left\langle \frac{\partial}{\partial \mathbf{R}_i} \hat{\Omega}(\{\beta_{\alpha}\}, \{\mu_{\alpha}\}, \{\mathbf{R}_j\}) \right\rangle \\ &= - \left\langle \frac{\partial}{\partial \mathbf{R}_i} \left[ \hat{H}(\{\mathbf{R}_j\}) - \hat{Y}(\{\beta_{\alpha}\}, \{\mu_{\alpha}\}, \{\mathbf{R}_j\}) \right] \right\rangle \end{aligned} \quad (2.27)$$

where indices  $i, j$  go over the  $P$  atoms. The concatenation of the  $P$  3D-vectors forms the  $3P$ -dimensional jacobian vector of derivatives useful for the geometry optimization calculations described in section 2.3.4. In case of any of the three spatial coordinates for atom  $i$  is frozen, not subject to the minimization, it will be not included in the jacobian.

### 2.3.4 Analytical derivatives

In this section we present the details of the actual implementation of the equations discussed above using as an example Eq. (2.25). Differentiating with respect to the coordinate  $\mathbf{R}_i$ , which can be the  $x, y$  or  $z$  component of the  $i$ th atom:

$$\begin{aligned} \frac{\partial}{\partial \mathbf{R}_i} Y^Q &= \sum_{\alpha} \frac{\beta_{\alpha}}{\beta} \mu_{\alpha} \int_{-\infty}^{\infty} dE \frac{\partial}{\partial \mathbf{R}_i} \text{Tr} \left[ \hat{\mathcal{G}}_{\alpha}^{\leq}(E) \right] \\ &= \sum_{\alpha} \frac{\beta_{\alpha}}{\beta} \mu_{\alpha} \int_{-\infty}^{\infty} dE \text{Tr} \left[ \frac{\partial}{\partial \mathbf{R}_i} \hat{\mathcal{G}}_{\alpha}^{\leq}(E) \right]. \end{aligned}$$

Now taking into account the expression for  $\hat{\mathcal{G}}_{\alpha}^{\leq}(E)$  in:

$$\begin{aligned} \hat{\mathcal{G}}^{\leq} &= \sum_{\alpha} \hat{\mathcal{G}}_{\alpha}^{\leq} \\ \hat{\mathcal{G}}_{\alpha}^{\leq} &= \hat{\mathcal{G}}^R \hat{\Sigma}_{\alpha}^{\leq} \hat{\mathcal{G}}^A. \end{aligned} \tag{2.28}$$

and applying the chain rule:

$$\begin{aligned} \frac{\partial}{\partial \mathbf{R}_i} \hat{\mathcal{G}}_{\alpha}^{\leq}(E) &= \frac{\partial}{\partial \mathbf{R}_i} \left[ \hat{\mathcal{G}}^R(E) \hat{\Sigma}_{\alpha}^{\leq}(E) \hat{\mathcal{G}}^A(E) \right] \\ &= \frac{\partial}{\partial \mathbf{R}_i} \left[ \hat{\mathcal{G}}^R(E) \right] \hat{\Sigma}_{\alpha}^{\leq}(E) \hat{\mathcal{G}}^A(E) \\ &\quad + \hat{\mathcal{G}}^R(E) \underbrace{\frac{\partial}{\partial \mathbf{R}_i} \left[ \hat{\Sigma}_{\alpha}^{\leq}(E) \right]}_0 \hat{\mathcal{G}}^A(E) \\ &\quad + \hat{\mathcal{G}}^R(E) \hat{\Sigma}_{\alpha}^{\leq}(E) \frac{\partial}{\partial \mathbf{R}_i} \left[ \hat{\mathcal{G}}^A(E) \right] \end{aligned}$$

Notice that

$$\frac{\partial \hat{\Sigma}_{\alpha}^{\leq}(E)}{\partial \mathbf{R}_i} = 0$$

since the self-energy can always be taken independent of the moving coordinates of the central region when connecting the electrode sufficiently far away. In this regard one decision to make concerns the size of this central region, i.e., the actual Hamiltonian  $H$ . Even if the atomic coordinates of the reservoir are considered fixed, energy changes may occur outside the central region since the electronic perturbation can propagate into the reservoir. The only way to guarantee this is by making the central

region larger and larger until convergence in the size is achieved. Alternatively, depending on how many atoms are included in the central region, it may be necessary to calculate the perturbation on the electronic density of the first layers of the electrodes and update their self-energy accordingly in the self-consistency.

Now we represent the operators on a generic non-orthogonal basis where the retarded and advanced Green's function operators become matrices

$$\mathcal{G}^{R(A)}(E) = \left[ (E \pm i\eta)\mathcal{S} - (\mathcal{H} + \Sigma^{(\dagger)}(E)) \right]^{-1},$$

where

$$\Sigma(E) = \sum_{\alpha} \Sigma_{\alpha}(E).$$

We apply now the differentiation rule for inverse matrices:

$$\frac{\partial}{\partial \mathbf{X}} [\mathcal{K}]^{-1} = [\mathcal{K}]^{-1} \left[ \frac{\partial}{\partial \mathbf{X}} \mathcal{K} \right] [\mathcal{K}]^{-1}$$

to obtain

$$\begin{aligned} & \frac{\partial}{\partial \mathbf{R}_i} \left[ \mathcal{G}^{R/A}(E) \right] \\ &= \mathcal{G}^{R/A}(E) \left[ (E \pm i\eta) \frac{\partial \mathcal{S}}{\partial \mathbf{R}_i} - \frac{\partial \mathcal{H}}{\partial \mathbf{R}_i} \right] \mathcal{G}^{R/A}(E). \end{aligned} \quad (2.29)$$

Also notice that we have used the fact that

$$\frac{\partial \Sigma(E)}{\partial \mathbf{R}_i} = 0$$

in Eq. (2.29) which further simplifies the evaluation.

As anticipated in previous section, interactions will be described in the framework of HF or DFT. Localized atomic orbitals are a standard choice in many codes and are appropriate to partition the infinite system into the central part and the reservoirs (D Jacob & Palacios, 2011). Theoretical chemistry codes such as Gaussian (**g16**) or our quantum transport code based on it, ANT.Gaussian (J. J. Palacios, Pérez-Jiménez, Louis, & Vergés, 2001; D Jacob & Palacios, 2011) use gaussian-type orbital basis. These are convenient since analytical expressions are available for the matrix elements of one-body operators such as the electron-nuclear interaction  $V_{e-N}$ , the kinetic energy  $T$  (which adds to the noninteracting Hamiltonian  $H_0 = V_{e-N} + T$ ), the overlap  $S$ , and also the two-body integrals necessary to construct the electron-electron interaction matrices  $V_{e-e} = J + K$  (in the H-F approximation). To calculate the forces, first (and second) analytical derivatives of the matrix elements are also available with respect to the coordinates of the atomic centers on which the basis elements are centered:

$$\frac{\partial}{\partial \mathbf{R}_i} O_{jk}; \quad O = V_{e-N}, T, S, J, K... \quad (2.30)$$

where  $O$  can be any of the matrices which represent the operators in the problem.

In steady-state, the Gibbs Free Energy for each lead considered in equilibrium with it's chemical potential  $\mu_{L,R}$  can be calculated from the density of states of the electrodes  $\hat{D}_{L,R}(E) = \frac{1}{2\pi i} G_{L,R}(E)$ :

$$\langle \hat{Y}_\alpha^Q \rangle = \mu_\alpha \int_{-\infty}^{\infty} dE \frac{1}{2\pi i} G_\alpha(E) = \mu_\alpha \hat{N}_\alpha \quad (2.31)$$

In the central region there is no unique chemical potential to be considered, but the charge can be separated by means of the partial spectral density matrix in 2 contributions

$$\langle \hat{Y}_C^Q \rangle = \sum_{\alpha=L,R} \mu_\alpha \int_{-\infty}^{\infty} dE E \frac{1}{2\pi i} G_{\alpha,ij}^<(E) \quad (2.32)$$

In the central region  $C$ , there may exist isolated states which do not cross to any of the reservoirs. Because of this fact, these states do not contribute to the work done by the reservoirs on the system and need not to be included in the calculation of  $\hat{Y}_C^Q$ .

then given as:

## 2.4 RESULTS

We perform calculations on atomistic systems in equilibrium and out of equilibrium like the one depicted fig. 4.1. The equilibrium geometries are reached following the gradient of the canonical grand potential  $\Omega$ , and correspond to its minima with respect to the coordinates of each atom.

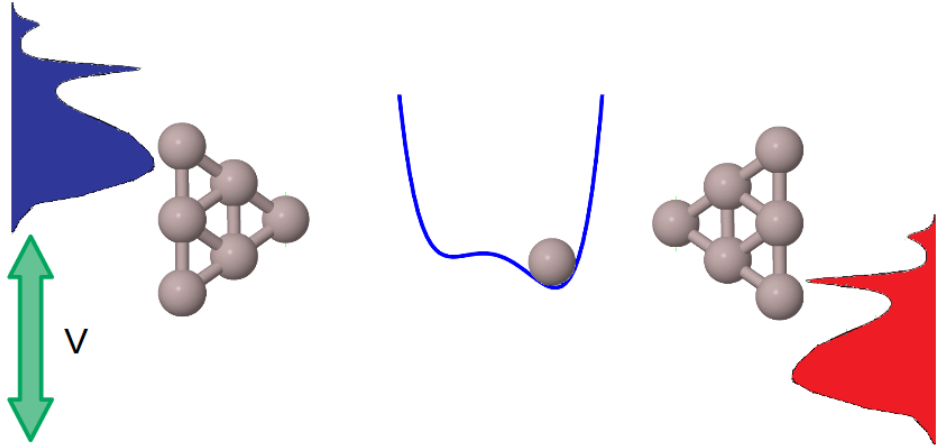


Figure 2.1: Toy representation of an atomic contact between whose two tips an atom can be moved by means of bias or temperature, following the gradient of the canonical grand potential  $\Omega$

### 2.4.1 Atom adsorption onto a single electrode: checking the method

How can we check that our method is correct? By comparing the results obtained for the canonical grand potential  $\Omega$  of an adatom chemisorbing on an infinite chain (system (b) in fig. 2.2) with the ones obtained for the adatom chemisorbing on a finite but big chain, by calculating the internal energy  $U$  (system (a) in fig. 2.2).

Because we are dealing with infinite systems (system (b) in fig. 2.2), it is not correct to speak about the total canonical grand potential, but canonical grand potential differences calculated for the selected region of the system on which the perturbation is not negligible. Along the infinite reservoirs used, the perturbation due to the chemisorption of an adatom is considered to vanish.

#### 2.4.1.1 Noninteracting electrons

For a finite chain of atoms populated by noninteracting electrons (system (a) in fig. 2.2), therefore, electron-hole symmetric, the internal energy vs. position curve for the chemisorption of an adatom can be calculated at any chemical potential. It can be calculated at  $\mu = 0$ , which is the neutral condition. But it can be also calculated at  $\mu = \mu_L$ , the chemical potential of the LUMO, or  $\mu = \mu_H = -\mu_L$  (because of the electron-hole symmetry), the chemical potential of the HOMO.

If we compare the canonical grand potential  $\Omega$  vs. position curves for such a chemisorption at any chemical potential (blue, green and yellow lines in fig. 2.3), the results must approach those of the internal energy  $U$  vs. position for a finite but big chain (dotted blue line in fig. 2.3). If the finite chain is taken increasingly long, both results must match. However, if only the Hamiltonian and the internal energy  $U$  are calculated for the first atoms of infinite chains (purple, brown and red lines in fig. 2.3), the result must differ from the reference one, as shown in fig. 2.3.

Depending on how many atoms are included in the central region  $C$  in the Caroli partition scheme, it will be necessary or not to calculate the perturbation on the electronic density in the first layers of the source reservoir  $S$ . The projection of the Gibbs free energy operator can be calculated as:

$$\hat{\mathcal{Y}}_{SS}^Q = \mu \int_{-\infty}^{\infty} dE \frac{1}{2\pi i} \hat{\mathcal{G}}_{SS}(E) \quad (2.33)$$

where  $\hat{\mathcal{G}}_{SS}(E)$  and its matrix form  $G_{SS}(E)$  are calculated in (F.29) and (F.28) respectively.

Because only one electrode is involved, its chemical potential  $\mu$  is common for the whole system, and the projection of the Gibbs free energy operator in the central region can be calculated as:

$$\hat{\mathcal{Y}}_{CC}^Q = \mu \int_{-\infty}^{\infty} dE \frac{1}{2\pi i} \hat{\mathcal{G}}_{CC}^<(E) \quad (2.34)$$

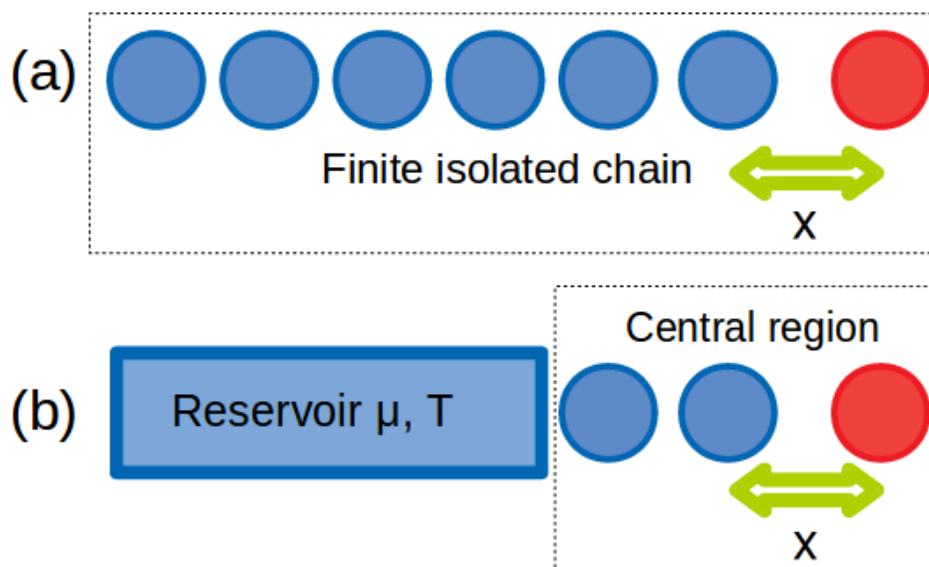


Figure 2.2: Two different systems to be compared. System (a) is a finite chain to whose tip the red adatom can be chemisorbed, developing the internal energy  $U$  vs. position  $x$  curve. System (b) is an infinite chain, modelled by a 1D-reservoir, to whose tip the red adatom can be also chemisorbed, developing, in this case, the canonical grand potential  $\Omega$  vs. position  $x$  curve.

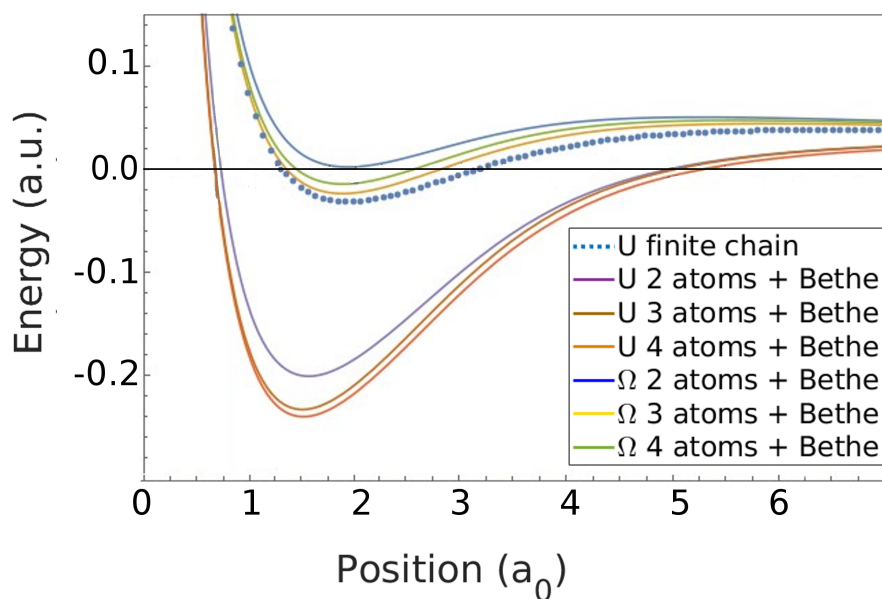


Figure 2.3: Energy-distance curves for the adsorption of an adatom on the tip of a chain. The blue dotted line represents the internal energy  $U$  curve for the adsorption on a finite 20-atom chain. The purple, brown and red lines, which lie far below the dotted one, represent the internal energies  $U$  of 2-, 3- and 4-atom chains connected to an infinite reservoir chain providing the open boundary conditions, which are not correct. The blue, red and yellow lines, which approach progressively the dotted one, represent the canonical grand potential  $\Omega$  of 2-, 3- and 4-atom chains connected to an infinite reservoir chain providing the open boundary conditions, which are correct.

### 2.4.1.2 *Interacting electrons*

Following the same philosophy as in section 2.4.1.1, it is convenient to compare the results for the grand potential  $\Omega$  vs. position curves of interacting systems with the ones obtained for the internal energy  $U$  vs. position of isolated but big systems. As a reference, we have used the LCAO based Gaussian chemistry code (M. J. Frisch, Trucks, Schlegel, Scuseria, Robb, Cheeseman, Scalmani, Barone, Mennucci, Petersson, Nakatsuji, Caricato, Li, Hratchian, Izmaylov, Bloino, Zheng, Sonnenberg, Hada, Ehara, Toyota, Fukuda, Hasegawa, Ishida, Nakajima, Honda, Kitao, Nakai, Vreven, Montgomery, Jr., et al., 2009).

For our purpose, the reference calculation performed by Gaussian consists of a 20-atom single-orbital isolated chain under unrestricted Hartree-Fock (UHF) from which one apex atom is extracted. While the chemical bond between the atom and the chain resists, the system remains in a singlet or restricted Hartree-Fock (RHF) solution (see fig. 2.4). However, when the chemical bond breaks, an unpaired electron jumps to the atom, leaving also an UHF density matrix in the chain (see fig. 2.4).

To be compared with the 20-atom isolated chain, we choose a 6-atom chain, treated as the central region  $C$ , connected to an infinite reservoir at a fixed chemical potential, from which it can take as many electrons as it needs. In this 6-atom central region, we calculated both, the internal energy  $U$  and the grand potential  $\Omega$ .

While separating the apex atom from the rest of the chain, the transition from the RHF density to the UHF one occurs, forcing an abrupt charge rearrangement in the central region, which forces the reservoir to inject electrons into it. Before the breakup of the bond, the central region contains a tip accumulating charge. However, after the breakup, it contains not only a tip, but also an isolated atom, accumulating more charge. In the case of the isolated chain, it implies a charge defect along the rest of the chain, except for both apex, which accumulate charge. In the case of the infinite chain, however, no charge-per-atom defect appears.

When calculating the internal energy of the central region for the infinite system, this charge accumulation implies an abrupt increment of the internal energy, which is shown in fig. 2.4. But from the reference calculation, we know that this increment in the internal energy is compensated with the charge defect in the rest of the chain. The work done on the rest of the chain is what the internal energy of the central region does not take into account, in analogy to the classical case in section 2.2. However, the Gibbs free energy solves this problem, equilibrating the energy imbalance and recovering the energy vs. position profile for the grand potential, as can be seen in fig. 2.4.

The curves in 2.4 were calculated with Hydrogen atoms modelled by the STO-3G basis (Gordon, Binkley, Pople, Pietro, & Hehre, 1982). All the curves are calculated through the Hartree-Fock Method.

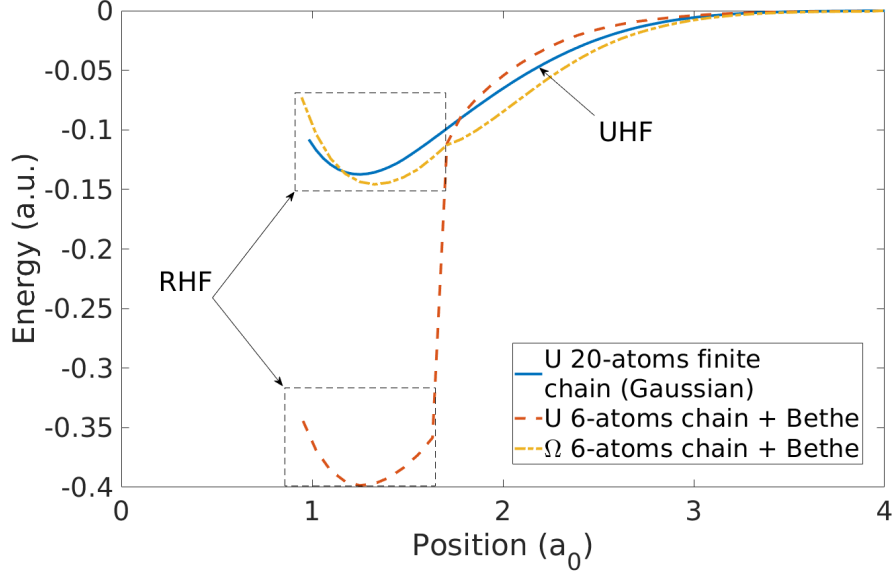


Figure 2.4: Energy-distance curves for the adsorption of an adatom on the tip of a chain. The blue line represents the internal energy  $U$  curve for the adsorption on a finite 20-atom chain. The red discontinuous line represents the internal energies  $U$  of a 6-atom chain connected to an infinite reservoir providing the open boundary conditions. The yellow dotted line, which approaches the blue one, represents the canonical grand potential  $\Omega$  of a 6-atom chain connected to an infinite reservoir providing the open boundary conditions.

#### 2.4.2 Two electrodes

The Gibbs Free Energy for each lead considered in equilibrium with its chemical potential  $\mu_{L,R}$  can be calculated from the Green's function or the density of states of the electrodes:

$$\hat{y}_{\alpha\alpha}^Q = \mu \int_{-\infty}^{\infty} dE \frac{1}{2\pi i} \hat{G}_{\alpha\alpha}(E); \quad \alpha = L, R \quad (2.35)$$

where we use the subscript  $\alpha\alpha$  to point that this is the projection in the partition  $\alpha$  of the operators and matrices, in contrast to the single subscript  $\alpha$  which, in case of the lesser Green's function  $G_{\alpha}^{<}$  in the central region, labels the incoming density from reservoir  $\alpha$  onto the central region  $C$  and projected into it, as will be used in (2.36).

In the central region there is no unique chemical potential to be considered, but the charge can be separated by means of the partial spectral density matrix in two contributions

$$\hat{y}_{CC}^Q = \sum_{\alpha=L,R} \mu_{\alpha} \int_{-\infty}^{\infty} dE E \frac{1}{2\pi i} \hat{G}_{\alpha}^{<}(E) \quad (2.36)$$

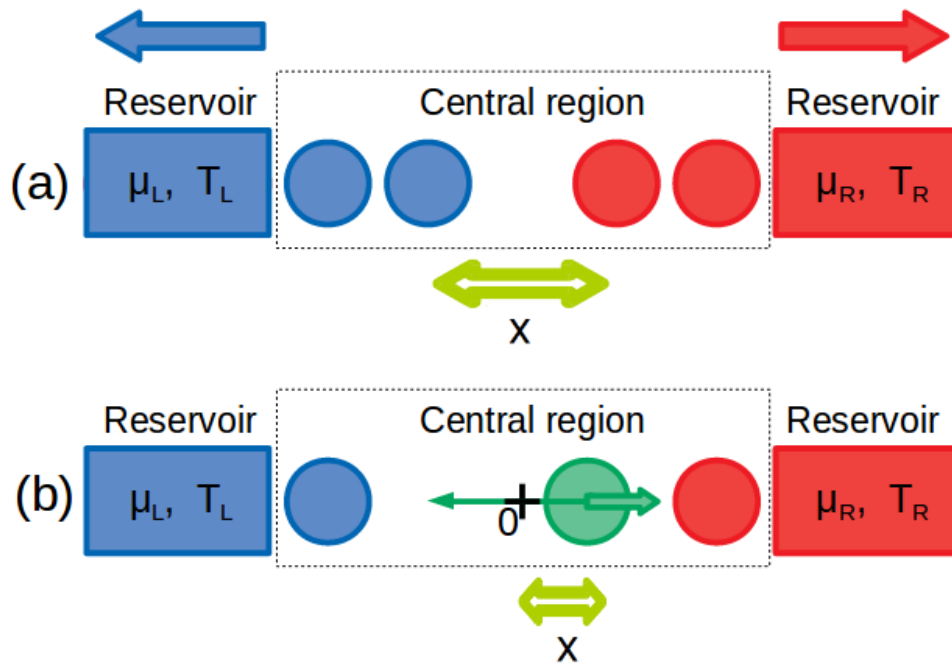


Figure 2.5: Energy-distance curves for the adsorption of an adatom on the tip of a chain. The blue dotted line represents the internal energy  $U$  curve for the adsorption on a finite 20-atom chain. The purple, brown and red lines, which lie far below the dotted one, represent the internal energies  $U$  of 2-, 3- and 4-atom chains connected to an infinite reservoir chain providing the open boundary conditions, which are not correct. The blue, red and yellow lines, which approach progressively the dotted one, represent the canonical grand potential  $\Omega$  of 2-, 3- and 4-atom chains connected to an infinite reservoir chain providing the open boundary conditions, which are correct.

It is worth noting that the isolated states do not contribute to the work performed by the reservoirs. Thus, it is enough to consider the left/right incoming eigenstates contained in  $\hat{G}_{L/R}^<(E)$  for the calculation of the Gibbs free energy.

### 2.4.3 Attraction between the plates of a quantum capacitor

To check that the two plates of a quantum atomic capacitor (fig. 2.5) also attract when a bias is applied between both, as occurs in the classical macroscopic capacitor treated in section 2.2. Calculations at different biases have been performed to check that the higher the applied bias, the stronger the attraction between the plates. The results are depicted in fig. 2.6.

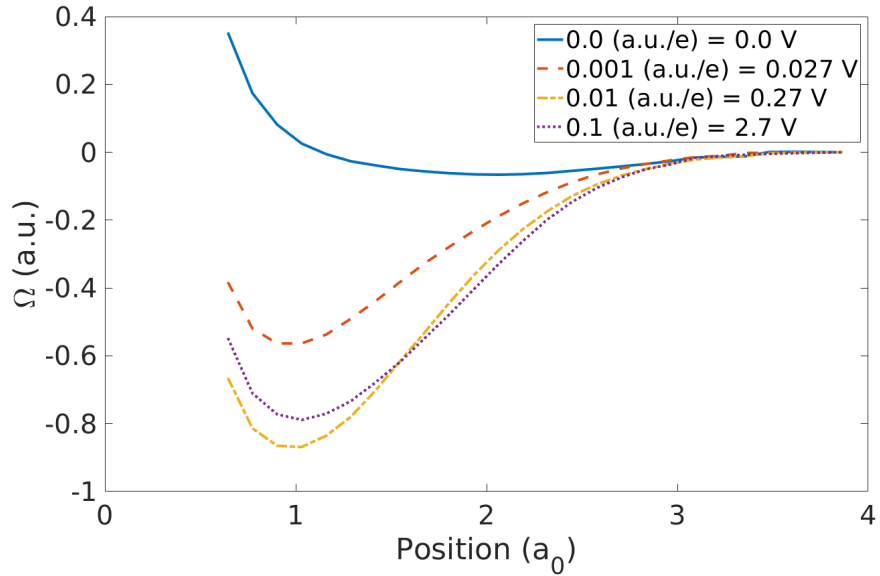


Figure 2.6: Energy curves for the separation of the two plates of a quantum 1D atomic capacitor consisting of two semiinfinite chains. The tip-tip distance is represented in the horizontal axis, while the vertical one represents the calculated canonical grand potential  $\Omega$ .

### 2.4.4 Electromigration of an atom between two electrodes

If we consider an atom moving between two symmetric chains connected to reservoirs, even at equilibrium bias and temperature, with interacting electrons subject to the Hamiltonian  $H$  in equation (1.5) there appear thermodynamic forces due to the exchange of particles with the reservoirs. The model consists of two diatomic single-orbital tips with two vacancies between them. Thus, the tip-tip distance is three times the lattice parameter of the chains. While moving the atom between both tips, we can calculate the internal energy  $U$  vs. position and the grand potential  $\Omega$  vs. position curves, as in fig. 2.7.

#### 2.4.4.1 Equilibrium

Even when both electrodes have the same chemical potential  $\mu$ , there appear thermodynamical forces which are typically attractive between both electrodes, as expected from the classical counterpart explained in section 2.2. The equilibrium thermodynamic forces which result from the gradient of the canonical grand potential  $\Omega$  help the central atom maintaining the bond between both tips, as can be seen in fig. 2.7. If only the internal energy  $U$  of the central region were considered, the atom would fall onto one of the electrodes, breaking the contact between both.

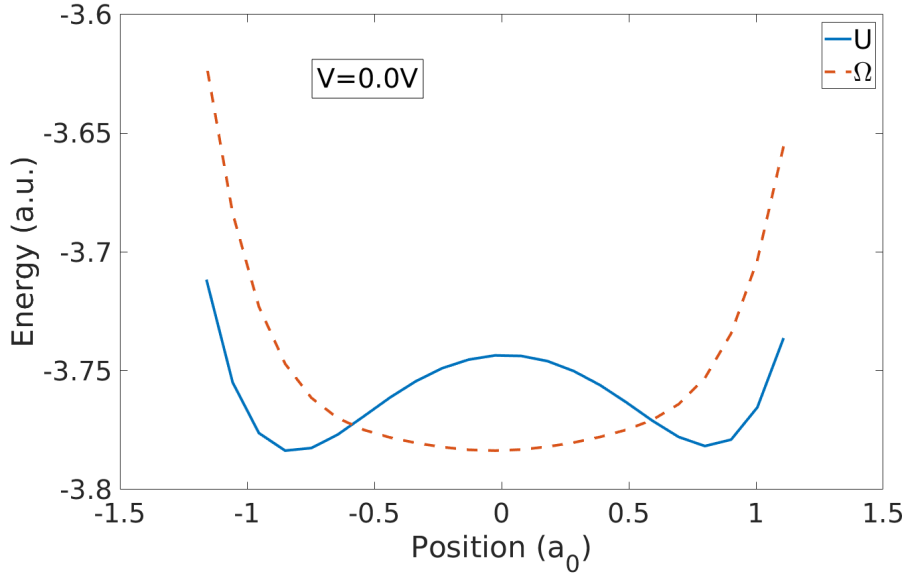


Figure 2.7: Energy curves for an atom moving between two diatomic single-orbital tips with two vacancies between them. The tip-tip distance is three times the lattice parameter of the chains. The blue curve represents the internal energy  $U$  vs. position, while the red dashed curve represents the grand potential  $\Omega$  vs. position curves.

If we look at fig. 2.7, we can check that while the internal energy  $U$  shows two symmetric minima, which coincide with the adsorption minima on each of the tips conforming the electrodes, the grand potential  $\Omega$  shows a single minimum equidistant to both tips. The physical interpretation of this fact is that, while the internal energy behaviour would have broken the contact, the action of the Gibbs free energy  $Y$  on the canonical grand potential  $\Omega$  helps the system to maintain the bond stable, kept by the presence of the thermodynamic forces.

#### 2.4.4.2 Nonequilibrium bias

By applying different voltages to the same system, we get the results in fig. 2.8. We observe that in equilibrium the atom stays between the two tips, but, even with small voltages, a potential barrier appears between the two tips and the atom chemisorbs onto one of them. To eject drastically the atom from one tip, voltages above  $2V$  are needed. The capability to eject atoms from one tip to another is expected to be easier for materials with a noticeable electron-hole asymmetry. Atoms with a higher density of states for electrons (under the Fermi level) will chemisorb to the negative

electrode, while atoms with a higher density of states for holes (above the Fermi level) will chemisorb to the positive one.

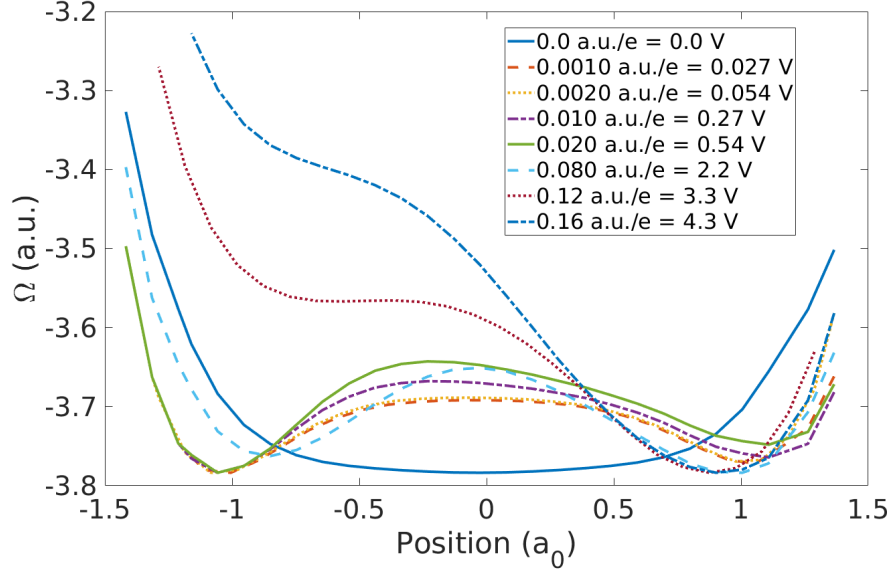


Figure 2.8: Energy curves for an atom moving between two diatomic single-orbital tips with two vacancies between them. Thus, the tip-tip distance is three times the lattice parameter of the chains. All the curves represent the grand potential  $\Omega$  vs. position curves at different applied voltages.

#### 2.4.4.3 Nonequilibrium temperature

In the same system, if a temperature gradient is applied, instead of a voltage drop, there appear also forces according to the definition of the Gibbs free energy operator for a temperature gradient  $\hat{Y}^E$  in (2.9). Temperature gradients along contacts have been applied between the ranges ( $10K - 10K = 0K$ ), ( $20K - 10K = 10K$ ) ... ( $100K - 10K = 90K$ ). The results for the calculations are shown in fig. 2.9.

#### 2.4.5 Alternative formulation in terms of the current operator

As suggested by Han (J. E. Han, 2007), the nonequilibrium statistical operator for the exchange of particles can be rewritten in the case of noninteracting systems which are neutral at zero chemical potential  $N(\mu = 0) - Z = 0$  connected to two reservoirs  $L/R$ , at low biases in the linear response regime (small  $V$ ,  $|I| \propto |V|$ ), in terms of the current operator as:

$$\hat{Y}_I^Q \equiv V \hat{y} = V \left[ \hat{y}_0 - \frac{1}{e} \frac{i}{-\hat{\mathcal{L}} + \eta} \hat{I} \right] \quad (2.37)$$

where  $e$  is the electron charge,  $\eta$  is a small positive constant,  $\hat{y}_0 = \frac{1}{2} \sum_k (\hat{c}_{Lk}^\dagger \hat{c}_{Lk} - \hat{c}_{Rk}^\dagger \hat{c}_{Rk})$  is the difference between the number operators before the connection is es-

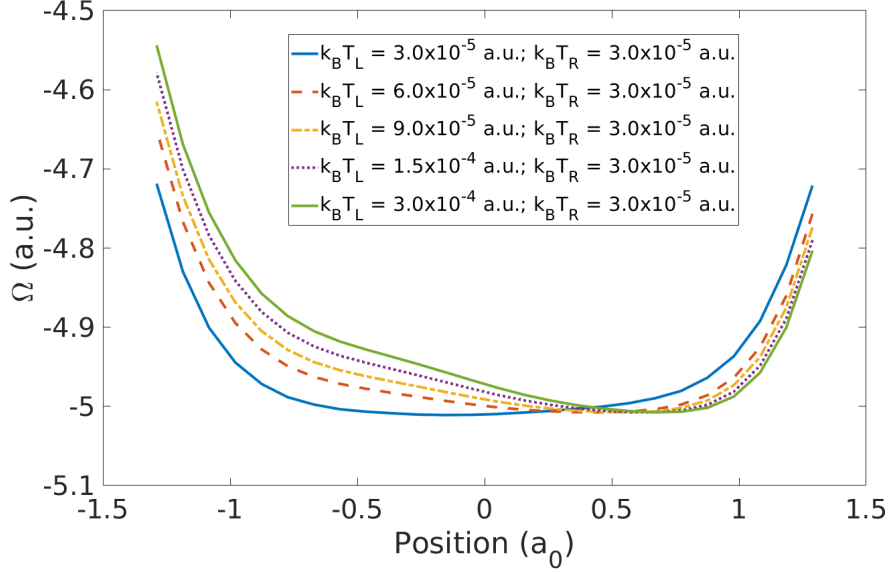


Figure 2.9: Energy curves for an atom moving between two diatomic single-orbital tips with two vacancies between them. The tip-tip distance is three times the lattice parameter of the chains. All the curves represent the grand potential  $\Omega$  vs. position curves at different applied temperature gradients.

tablished, being the  $\hat{c}_{\alpha k}$ 's the bare field operators for the disconnected system. The Liouvillian  $\check{\mathcal{L}}$  is the superoperator which performs the commutation with the Hamiltonian as  $\check{\mathcal{L}}\hat{O} = [\hat{H}, \hat{O}]_-$ . The current operator can be calculated as the commutation of the Hamiltonian with the lesser Green's function operator  $\hat{I} = [\hat{H}, \hat{G}^<]_-$ , for example. The comparison of the results for the ensemble average of operator  $\hat{Y}^Q$  and Han's expression  $\hat{Y}_I^Q$  (2.37) and the conventional one (2.8) are shown in figure 2.10 by separating a symmetric atomic 1D-contact at different applied voltages. The parameters of the model for the LCAO basis are non-realistic, thus, the applied voltages may be. Because of the charge neutrality condition at  $\mu = 0$ , the value of  $\langle \hat{Y}^Q \rangle$  is zero for all distances. As shown in figure 2.10, both results coincide for small voltages and currents. Applying bigger voltages undermines the linear response condition, by which  $|I| \propto |V|$ .

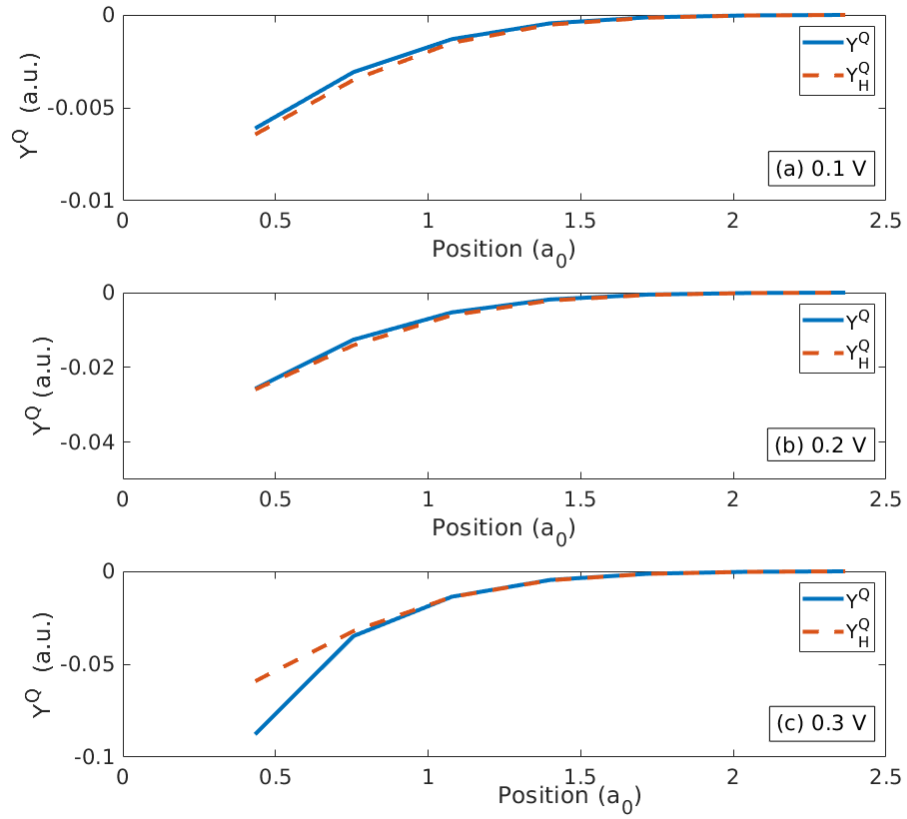


Figure 2.10: Variation of the ensemble average  $\langle \hat{Y}^Q \rangle$  with the distance for a symmetric atomic 1D-contact. The blue lines display the voltage based conventional expression  $\langle \hat{Y}^Q \rangle$  while the red discontinuous ones represent  $\langle \hat{Y}_I^Q \rangle$ . Results for voltages of 0.1V, 0.2V and 0.3V are shown in subfigures (a), (b) and (c) respectively.

## NEGFY CODE

---

### 3.1 ABSTRACT

NEGFY code is a quantum chemistry program used to solve the electronic structure of atoms, molecules, crystals and molecular junctions based on the Nonequilibrium Green's Function Formalism in its matrix form on a basis of Gaussian Orbitals as done by the code ANT.G, originally developed by JJ. Palacios at the University of Alicante. Its Hartree-Fock and DFT implementations to build the Hamiltonian are based primarily on the Quantum Chemistry codes ERKALE (Lehtola, Hakala, Sakko, & Hämäläinen, 2012), originally developed by Susi Lehtola at the University of Helsinki, and Libint (Kenny, Janssen, Valeev, & Windus, 2008), originally developed by Eduard Valeev at Virginia Tech. The DFT functionals are implemented through library (Marques, Oliveira, & Burnus, 2012).

### 3.2 DESCRIPTION

The NEGFY code is a numerical implementation of the evaluation of forces in first-principles non-equilibrium quantum transport calculations. Unlike closed systems, where this evaluation is carried out in the microcanonical ensemble, open systems, both in and out of equilibrium, require the evaluation of the Grand Canonical Potential (generalized to non-equilibrium situations) and its derivatives with respect to the atomic coordinates. NEGFY code uses gaussian-based localized atomic orbitals as a basis set in the actual calculations.

The NEGFY code encompasses in a practical implementation the theory explained in chapters 1, 2. In chapter 2 few proof-of-principle examples are presented which show the feasibility of these calculations and illustrate some of the issues faced in these type of calculations. As a practical case, we show how a finite bias can induce electromigration of atoms between metallic tips. Chapters 4, 6 display other usages of the code that prove the feasibility of the method.

The code can be downloaded from:

<https://github.com/carlos-sg/negfy>

### 3.3 RESULTS

The curves in 3.1 were calculated with Hydrogen atoms modelled by the STO-3G basis (Gordon et al., 1982) and the Hartree-Fock Method, but the immense variety of functionals present in libxc (Marques et al., 2012) can be used.

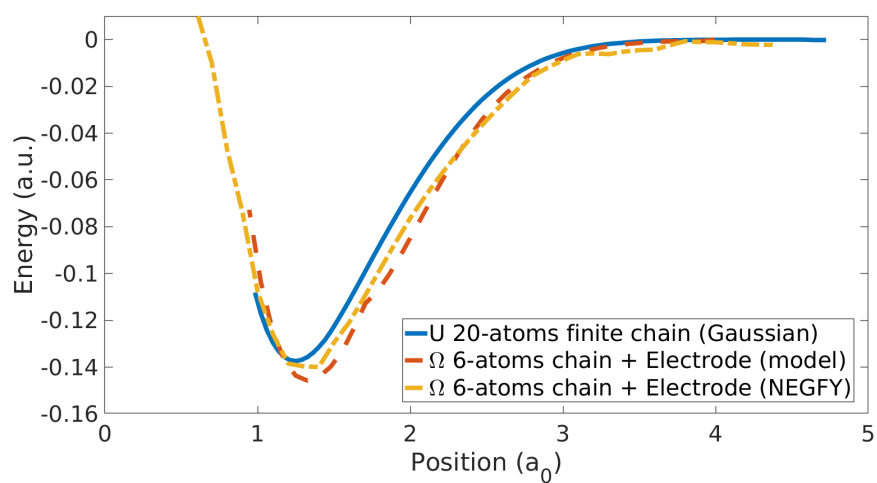


Figure 3.1: Energy-distance curves for the adsorption of an adatom on the tip of a chain. The blue line represents the internal energy  $U$  curve for the adsorption on a finite 20-atom chain. The red discontinuous line represents the canonical grand potential  $\Omega$  of a 6-atom chain connected to an infinite reservoir providing the open boundary conditions as calculated with a simple model. The yellow dotted line, which approaches the blue one, represents also the canonical grand potential  $\Omega$  of a 6-atom chain connected to an infinite reservoir, but calculated with NEGFY code.

## HYDROGEN ADSORPTION FROM GRAPHENE WITH A PLATINUM STM TIP

---

### 4.1 ABSTRACT

By using the STM tip to manipulate hydrogen atoms with atomic precision, it is possible to tailor the magnetism of selected graphene regions. DFT calculations for open systems to simulate the tip-surface device were performed in (González-Herrero et al., 2016).

### 4.2 INTRODUCTION

To understand the chemisorption phenomenon of Hydrogen on graphene, the nature of the chemical bonds involved in the process has to be unravelled. Not only the Hydrogen Carbon bond, but the bond between the Hydrogen atom and the Platinum tip apex atom are relevant. The first, for the adsorption of Hydrogen on graphene, and the last, for the adsorption of Hydrogen on the STM Platinum tip, as been published in (González-Herrero et al., 2016). The hexagonal lattice of graphene is formed by carbon atoms which are connected by means of  $sp^2$  hybridized orbitals. This electronic structure results in three  $\sigma$  orbitals contained in the graphene plane forming  $120^\circ$  angles between each other and one  $\pi$  orbital in the axis perpendicular to the graphene. For the Hydrogen atom to be chemisorbed, the  $\pi$  bonds need to be broken to form a new  $\sigma$  bond. The physical mechanism which allows such a transition is the local deformation of the crystallographic structure by a carbon atom moving out of the graphene plane, thus transforming the  $sp^2$  hybridization to  $sp^3$  hybridization. Not only the Carbon atom, which binds directly to the Hydrogen atom, but the three surrounding ones move up to favor the process. DFT calculations performed with SIESTA [Moaied] reveal a Carbon-Hydrogen distance of  $1.20 \text{ \AA}$ , with the central carbon moved  $0.35 \text{ \AA}$  upwards and the three surrounding around  $0.08 \text{ \AA}$ . The  $sp^3$  hybridization advantages the elongation of the hydrogenated graphene, and thus the lift of the Carbon atoms. The DFT calculated adsorption energy of the Hydrogen on graphene is around  $1.6 \text{ eV}$ . The other process which needs to be taken into account is the Hydrogen adsorption at the platinum STM tip, widely studied in quantum electrochemistry. The bond formed between the Platinum tip apex atom and the Hydrogen is formed by the  $5d^9$  and  $6s^1$  shells of the Platinum atom and the  $1s^1$  shell of the Hydrogen one. The calculated adsorption energy of the Hydrogen at the Platinum tip apex is around  $2.8 \text{ eV}$ , by means of DFT calculations using the Gaussian QC code. A result of  $1.20 \text{ \AA}$  arises for the Platinum - Hydrogen distance. Because of the difference between the adsorption energies for Hydrogen on graphene and on the Platinum tip, it can be inferred that the only obstacle to adsorb the Hydrogen from the graphene to the tip is the vacuum barrier. This vacuum barrier can be suppressed by approaching progressively the tip to the deposited Hydrogen until both energy min-

ima merge. When retracting, the vacuum barrier builds up, but the Hydrogen adsorbs completely on the Platinum tip because of the higher adsorption energy value, with which the graphene one cannot compete, which makes the total energy decrease. In our calculations, performed through the Matrix form of the Green's Function Method implemented in ANT.G, with the help of the DFT method implemented in Gaussian, only the electrons from the 5s 2, 5p 6, 5d 9 and 6s 1 shells of Platinum were treated explicitly, while the shells below these were replaced by Effective Core Potentials (ECP), as is the case of the LanL2DZ basis in the Gaussian QC code. In the case of Hydrogen, the same type of basis set reproduces the complete electronic structure without need of ECP potentials. Finally, the bonding Carbon atom was treated with the complete basis set LanL2DZ describing the six electrons, while the other carbon atoms were described by the minimum basis set CRENBS, in which only the 2s 2 and 2p 2 shells are treated explicitly, with the others replaced by an ECP potential. The functional used to describe the minimum total energy state of the system was the unrestricted BLYP, which leads to proper results for both, organic and metallic and non-metallic elements.

#### 4.3 EXPERIMENTAL ATOMIC H MANIPULATION

Choosing the appropriate tunneling parameters atomic H can be removed, laterally moved, and even deposited on graphene surfaces with atomic precision. The role played by the STM tip is to selectively modify the binding energy landscape of H atoms to produce the required H manipulation, see Sect. 10 for DFT calculations on the H extraction. To selectively remove H atoms from the graphene sample we approached the STM tip towards the sample. This can be done by continuously increasing, under feedback control, the setpoint tunneling current on top of the selected H atom until it is desorbed, or by switching the feedback off and slightly decreasing the tip-sample distance on top of it. It is also possible to completely remove all H atoms from a graphene region by imaging it at high currents. The precise tunneling values for the manipulation depend on each specific tip apex, but for the same tip apex those values are very reproducible. As a rough guide, for removing H atoms it is usually enough to approach the STM tip by 1-2 Å. The deposition of H atoms is done by applying negative sample voltages pulses. In order to deposit H atoms, we first need to pick them up from the graphene surface, so the tip can act as an H reservoir. Then by applying negative sample voltages pulses the H atoms are deposited on the selected graphene region under the tip position (see Fig. S13). Again, the voltage threshold for H deposition might vary from tip to tip, but values of around -5 V are usually enough for H deposition. Finally, small positive sample voltages enable the lateral manipulation of H atoms.

#### 4.4 THEORETICAL METHODOLOGY H ON GRAPHENE

The hexagonal lattice of graphene is formed by carbon atoms which are connected by means of sp<sup>2</sup> hybridized orbitals. This electronic structure results in three  $\sigma$  orbitals contained in the graphene plane forming 120° angles between each other and one  $\pi$  orbital in the axis perpendicular to the graphene. For the Hydrogen atom to

be chemisorbed, the  $\pi$  bonds need to be broken to form a new  $\sigma$  bond. The physical mechanism which allows such a transition is the local deformation of the crystallographic structure by a carbon atom moving out of the graphene plane, thus transforming the  $sp^2$  hybridization to a local  $sp^3$  hybridization (17,18).

In order to study the geometrical and electronic structure of the different defects in graphene we use the first principles density functional (47, 48) SIESTA code (49, 50) which uses localized orbitals as basis functions (51). We use a double basis set, non-local norm conserving pseudopotentials and for the exchange correlation functional we use the local density approximation (LDA). The results have been checked with generalized gradient approximation (GGA) (52) calculations. The calculations are performed with stringent criteria in the electronic structure convergence (down to  $10^{-5}$  in the density matrix), 2D Brillouin zone sampling (up to 1600 k-points), real space grid (energy cut-off of 400 Ryd) and equilibrium geometry (residual forces lower than  $3 \times 10^{-2}$  eV/Å). Due to the rapid variation of the density of states at the Fermi level, we used a polynomial smearing method (53). To study defects we use the super cell approximations in the way that we end up with an interaction between defects in the repeated unit cell. To minimize this interaction we use unit cells of different size and, in addition, we use "skewed" unit cells in a way that the lattice vector do not coincide with graphene symmetry directions therefore interactions along the zig-zag and armchair chains of atoms are minimized, see Fig. S15.

#### 4.5 10. PT TIP MANIPULATION OF H

To understand why a Pt STM tip can perform the manipulations shown in Fig. 4 of the main manuscript, we have carried out DFT calculations for a model system as the one shown in Fig. S19 where a pyramidal Pt tip approaches a H atom adsorbed on graphene. The calculated adsorption energy of a H atom on the Pt tip apex is around 2.8 eV. Because of the difference between the adsorption energy for H on graphene (around 1 eV) and that on the Pt tip, it can be inferred that H prefers to adsorb on the Pt tip, the only obstacle being the desorption barrier. This barrier can be suppressed by approaching progressively the tip to the deposited H. Figure S19 shows the evolution of the binding energy curve of the H atom in between the tip and graphene. When the tip gets closer both adsorption energy minima merge at some point. When retracting the tip, the desorption barrier builds up again, but now with the H adsorbed on the Pt tip (see also movie S1). The blue and red arrows indicate the spin density on the atoms as in the main text. The Pt tip apex also develops a magnetic moment, but we have not depicted it for clarity. The manipulation of H with the Pt tip has been modelled through the DFT+ Green's function methodology as implemented in ANT.G (54-56). The DFT part in this code is performed by Gaussian (57). Only the electrons from the 5s 2, 5p 6, 5d 9 and 6s 1 shells of Pt were treated explicitly, while the shells below these were replaced by Effective Core Potentials (ECP), as is the case of the LanL2DZ basis set in the Gaussian code. In the case of H, the same type of basis set reproduces the complete electronic structure without the need of ECP potentials. Finally, the bonding Carbon atom was treated with the complete basis set LanL2DZ describing the six electrons, while the other carbon atoms were described by the minimum basis set CRENS in which only the 2s 2 and 2p 2 shells are treated explicitly, with the

others replaced by an ECP potential. The functional used was BLYP, which typically leads to proper results for covalent and metallic bonds in both organic and metallic elements. The functional used was BLYP (58), which typically leads to proper results for covalent and metallic bonds in both organic and metallic elements, complemented with dispersion forces through the GD3 Grimme implementation (59).

and graphene as a function of tip-sample distance. See movie S1 for the complete sequence.

#### 4.6 CONCLUSIONS

STM manipulation plays a key role in the development and tuning of novel materials with impressive properties. Quantum Transport and Molecular Dynamics are a small building block necessary for this amazing field.

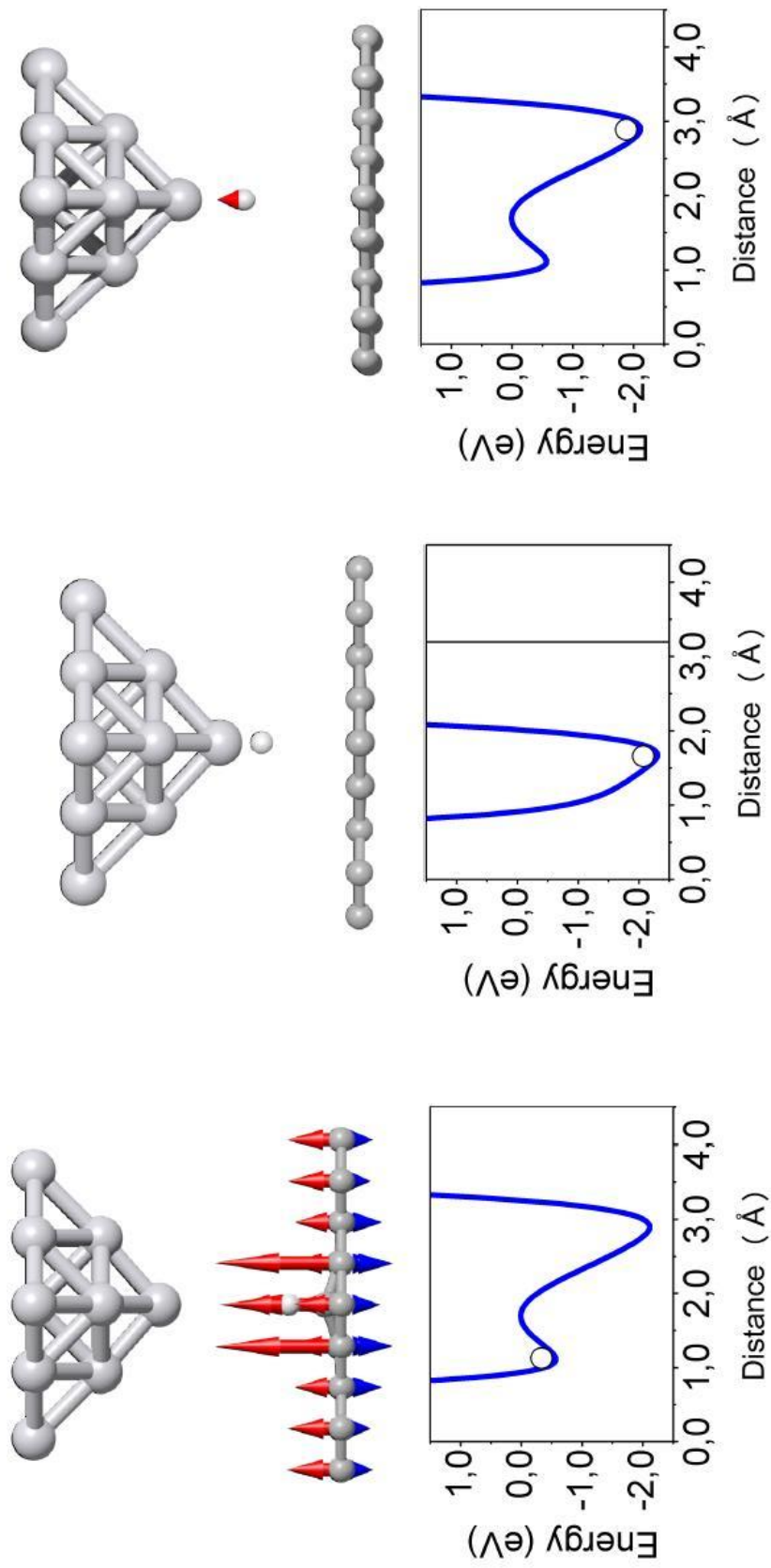


Figure 4.1: DFT calculation of the binding energy of the H atom in between the tip and graphene as a function of tip-sample distance. See movie S1 for the complete sequence

## ELECTRONIC TRANSPORT IN GADOLINIUM ATOMIC-SIZE CONTACTS

## 5.1 ABSTRACT

Fabrication, transport measurements, and density functional theory (DFT) calculations of atomic size contacts made out of gadolinium (Gd) are reported in this chapter, as been published in (Olivera et al., 2017). Gd is known to have local moments mainly associated with  $f$  electrons. These coexist with itinerant  $s$  and  $d$  bands that account for its metallic character. Here we explore whether and how the local moments influence electronic transport properties at the atomic scale. Using both Scanning Tunneling Microscope (STM) and lithographic Mechanically Controllable Break Junction (MCBJ) techniques under cryogenic conditions, we study the conductance of Gd when only few atoms form the junction between bulk electrodes made out of the very same material. Thousands of measurements show that Gd has an average lowest conductance, attributed to single-atom contact, below  $\frac{2e^2}{h}$ .

Our density functional theory (DFT) calculations show that for one dimensional chains a large spin splitting in the  $d$ -manifold emerges, in comparison with their bulk counterparts. We also analyze the electronic transport for model nanocontacts using the non-equilibrium Green's function formalism in combination with DFT. We obtain an overall good agreement with the experimental results and show that the contribution to the electronic transport from the  $f$ -manifold is negligible and that from the  $d$ -manifold is marginal.

## 5.2 INTRODUCTION

Quantum transport plays a key role in the electrical response of atomic scale contacts, giving rise to new phenomena differing from the bulk behavior of the different materials (Alexei Igorevich Yanson, 2001; N. Agraït & van Ruitenbeek, 2003; Naidyuk & Yanson, 2008). The central assumptions that permit to have a first guess of the conductance of an atomic scale contact are two. First, the conductance of the system is determined by the elastic transmission of the electrons at the Fermi level (Landauer formalism) and, second, the number of transmission channels that appear in the Landauer formula is determined by the chemical valence of the atoms (Scheer et al., 1998).

After three decades of exploration of electronic transport in atomic scale contacts, many materials with different physical properties have been studied. The groups that are relatively well understood include noble metals, such as Au (Agraït, Rodrigo, & Vieira, 1993) and Pt (R. H. M. Smit & van Ruitenbeek, 2001),  $sp$  metals, such as Al (Scheer, Joyez, Esteve, Urbina, & Devoret, 1997; Sánchez-Portal, Untiedt, Soler, Sáenz, & Agraït, 1997) and Zn (Häfner, Konrad, Pauly, Cuevas, & Scheer, 2004), ferromagnetic  $3d$  transition metals, such as Fe, Co and Ni (M. Reyes Calvo et al.,

2009), superconductors, such as Pb (Alexei Igorevich Yanson, 2001; M Müller, Salgado, Néel, Palacios, & Kröger, 2016; Cuevas et al., 1998), and even semi-metals such as Bi (Sabater et al., 2013; Pernau, Pietsch, & Scheer, 2014). Some metals like Ir (R. H. M. Smit & van Ruitenbeek, 2001), Pt (R. H. M. Smit & van Ruitenbeek, 2001) and Au (A. I. Yanson, Rubio Bollinger, Van Den Brom, Agraït, & Van Ruitenbeek, 1998; Ohnishi, Kondo, & Takayanagi, 1998) form single-stranded chains of atoms. Still, despite of all this effort, some important families remain to be covered.

In this context, while atomic contacts with  $s$ ,  $p$ , and  $d$  electrons have been widely explored, systems with partially filled  $f$  shells remain pretty much an uncharted territory (with a few exceptions (Marc Müller et al., 2010; Jammalamadaka et al., 2015)). On the other hand, there has been an interest to unveil the role of magnetism in the electronic transport in atomic-sized contacts. Later attempts in  $d$  materials have shown Kondo screening of the magnetic moments at such scale (Madhavan, Chen, Jamneala, Crommie, & Wingreen, 1998; M. Reyes Calvo et al., 2009; M. R. Calvo, Jacob, & Untiedt, 2012).  $f$  materials are therefore also good candidates to study the influence of the  $f$  decoupled magnetic moments on the transport electrons, mainly of  $s - p$ , and maybe  $d$  character.

Gd is a rare earth metal that belongs to the lanthanide group with the electronic configuration  $[\text{Xe}] 4f^7 5d^1 6s^2$ . It is a trivalent metal (Gschneidner & Eyring, 1978) that in bulk is a strong ferromagnet with  $T_C = 293.2 \text{ K}$  (H. E. Nigh & Spedding, 1963) with hexagonal close-packed (hcp) structure. It presents interesting properties, such as very high neutron absorption (Leinweber et al., 2006) and a pronounced magnetocaloric effect (Gschneidner Jr, Pecharsky, & Tsokol, 2005). Regarding other types of experimental measurements on rare earths, studies of electron-magnon interaction on point contacts made out of Gd, holmium (Ho), and terbium (Tb) (Akimenko & Yanson, 1980) as well as electronic structure measurements with photo-electron spectroscopy (Bovensiepen, 2007) have been performed. There are few experimental works about electronic transport on rare earth atomic-size contacts. Some of them (Berg, 2014; Marc Müller et al., 2010; Jammalamadaka et al., 2015) reported measurements on nanocontacts made out of metals such as yttrium (Y), cerium (Ce), dysprosium (Dy), and Gd by using the notched-wire MCBJ technique (N. Agraït & van Ruitenbeek, 2003).

Concerning calculations on lanthanide materials, not much has been published for atomic-scale contacts but their bulk properties have been widely studied. Calculations of the magnetic moment (R. Ahuja & Brooks, 1994; Kurz, Bihlmayer, & Blügel, 2002) of bulk Gd compare well with the measured  $7.63 \mu_B$  (H. E. Nigh & Spedding, 1963), where approximately  $7 \mu_B$  come from the  $4f^7$  orbital. As a result, the remaining  $0.63 \mu_B$  belong to the conduction electrons. Exchange interaction studies on Gd can be found elsewhere (Goodings, 1962). Moreover, several groups have calculated the electronic band structure (Temmerman & Sterne, 1990) from where the electronic density of states (DOS) as well as its projection on different orbitals has been inferred (I. Turek & Blügel, 2003; C. Santos & Eyert, 2004; Duan et al., 2007).

Here we present a combined experimental-theoretical work with two independent experimental techniques along with using DFT calculations. With STM we obtain a higher amount of statistical data than what can be obtained with lithographed MCBJ, which offers samples with much higher temporal stability. DFT calculations of both

electronic structure and transport properties have been carried out to give more insight into the interpretation of the experimental results.

### 5.3 EXPERIMENTS

Atomic-size contacts are the narrowest experimentally accessible junctions between bulk electrodes made out of the same material

(Gimzewski & Möller, 1987) (see inset in Fig. 5.1). In this work we investigate nanocontacts made out of pure metallic Gd. In order to study electronic transport on nanocontacts, we use STM (Binnig, Rohrer, Gerber, & Weibel, 1982) and lithographic MCBJ (Moreland & Ekin, 1985; Van Ruitenbeek et al., 1996) techniques, independently. With both techniques we record the electrical current through nanocontacts under fixed applied DC bias voltage when changing the contact geometry.

We use the STM technique in contact mode and we read the current from a low-noise amplifier with a gain factor of 5. With piezoelectric materials we control the distance between bulk electrodes with atomic precision ( $\sim 1$  pm) under cryogenic conditions (liquid helium bath). Samples consist of two wires of  $\sim 1$  mm diameter and cross-shaped arranged in order to avoid multi-contact locations. With this technique we build atomic contacts in a straightforward way, that is bringing into and out of contact the bulk wire-shaped electrodes by applying electrical DC sawtooth pulses to the piezos mentioned above.

Gd gets quickly oxidized in contact with air. In order to avoid contact with environmental compounds and to preserve the purity of these materials we use the following methods. For STM experiments, we mount samples inside a custom-made controlled atmosphere chamber. Gd wire-shaped samples have 99.9% purity and 0.5 mm diameter. We use argon gas (99.999% pure) as surrounding atmosphere before closing the STM under high vacuum conditions ( $10^{-8}$  mbar reached with turbo-molecular pumping). Besides, right before starting pumping, a ceramic (i.e. insulator and non-magnetic) knife is used for scratching the outer layer of Gd wires that are afterwards brought into contact. After pumping at room temperature, the STM is inserted into a bath cryostat filled with liquid helium (He). Then, when samples reach equilibrium with liquid He temperature, we measure the conductance as a function of distance when approaching or retracting the electrodes, so called conductance (creating/breaking) traces.

For comparison, we use the MCBJ technique (Van Ruitenbeek et al., 1996) in which a motor moves the pushing rod of a three-point bending mechanism with micrometric precision. This rod bends the sample from the rear side of the substrate right below the nano-junction location. The fabrication process of the latter will be explained below. The movement of the rod is reversible, so that atomic contacts can be created and broken repeatedly and the electronic transport through them is measured in the same way as with the STM technique.

In MCBJ experiments, we ensure the purity of Gd samples from the technique principle itself. As substrate we use 250 m thick gently polished bronze foil covered by a  $\approx 2$  m thick polyimide layer serving for planarization, electrical isolation and as sacrificial layer. Electron-beam lithography is performed in a scanning tunneling microscope equipped with a pattern generator to expose a PMMA-based two layer resist

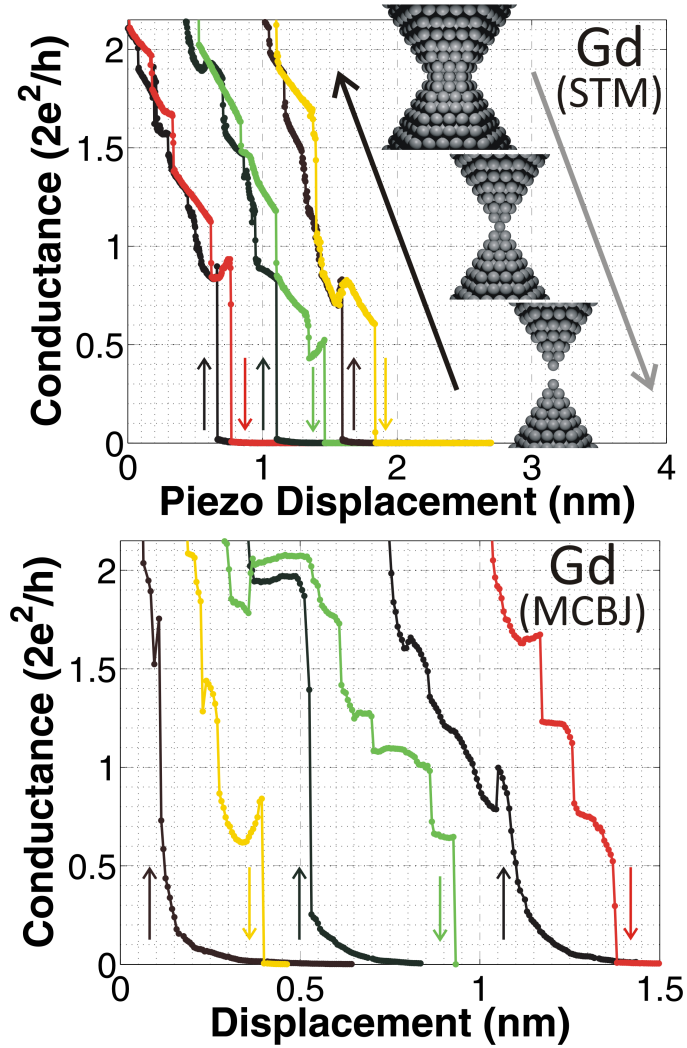


Figure 5.1: Typical conductance traces for atomic size contacts made out of Gd. Bright/dark curves stand for breaking/creating contacts as arrows indicate. Upper plot: Measurements taken with STM technique in equilibrium with liquid He bath and at  $10^{-8}$  mbar. All traces have been taken at 100 mV bias voltage. Inset: artistic representation of nanocontacts; hcp ball-stacking is pictured, where balls represent atoms. Lower plot: Measurements taken with lithographic MCBJ technique in equilibrium with liquid He bath and at  $10^{-5}$  mbar. Red and green traces and their return traces have been taken at 5 mV bias voltage, yellow curve has been taken at 10 mV.

after development. Gd pellets with 99.9% purity are thermally evaporated from a W boat, that avoids alloy formation. The evaporation speed is adjusted to have minimal mechanical strain in the film. The sample fabrication is completed by lift-off in acetone and reactive ion etching in an isotropic oxygen plasma to reduce the polyimide thickness and thereby suspending a Gd bridge of length  $\approx 2 \mu\text{m}$ , width  $\approx 100 \text{ nm}$  and thickness  $\approx 75 \text{ nm}$ . In order to avoid possible oxide coming from pristine Gd pellets, we cover the substrate for the first couple of evaporated nanometres of material. After evaporation, a subsequent final etching with oxygen plasma (Reactive Ion

Etching (RIE)) is performed to suspend nano-bridge. The sample is then mounted to a three-point bending mechanism anchored to a cryostat insert, pumped to a moderate high vacuum of  $10^{-5}$  mbar, and cooled down to liquid He temperature. The MCBJ contact is broken for the first time, when 4.2 K are reached. By this way, the few nanometres thick outer layer of Gd oxide at the sample protects the pure Gd nano-junction before MCBJ measurements start.

For both techniques, we record the electrical conductance as a function of distance between bulk electrodes (Agraït et al., 1993), obtaining the conductance traces (see Fig. 5.1). We focus on the last stages before breaking the contacts into the vacuum tunnel regime and the first ones when establishing metallic atomic-size contacts. The resulting conductance is in the order of  $\frac{2e^2}{h}$ , as expected for a quantum conductor with a few channels, and shows abrupt changes as a function of the electrode distance that reflect variations in the atomic configuration of the nanocontact (see Fig. 5.1). With STM technique we manage to create stable low-noise traces of conductance at a rate of about 10 traces per second. This allows us to obtain significant statistical data in a relatively brief period of time. The MCBJ technique enables mechanically more stable contacts than with the STM, but its rate of recording conductance traces is limited to about one trace per minute. We make histograms of conductance (A. I. Yanson & van Ruitenbeek, 1997) out of the measured traces with STM and MCBJ (see Fig. 5.2).

Thousands of conductance traces with deep indentations (beyond  $100 \frac{2e^2}{h}$ ) are recorded along with electro-migrative fast ( $\approx 0.5$  s) DC pulses of 10 V that are applied to randomly chosen atomic-size contacts.  $\frac{2e^2}{h}$  is the conductance quantum where  $e$  is the elementary charge and  $h$  is Planck's constant. A conductance of  $100 \frac{2e^2}{h}$  corresponds to a nanoconstriction with more than 100 atoms in cross section.

We have recorded conductance traces for different electrode configurations. Every configuration comes from geometrical reconstruction of bulk electrodes by strong indentation of electrodes with STM technique (beyond  $100 \frac{2e^2}{h}$ ). With MCBJ, a smaller amount of data is obtained (see caption at Fig. 5.2), therefore less variety of traces of conductance is achieved. Different families of conductance traces for this last technique are obtained moving back the pushing rod until reaching conductances beyond  $50 \frac{2e^2}{h}$ .

In Fig. 5.1 we show typical conductance traces. In the STM case For the STM technique (upper plot), we show a series of measurements few seconds spaced between them where deep indentations are performed. We observe that the last plateau always falls at conductance values visibly smaller than  $\frac{2e^2}{h}$ . The same observation applies for MCBJ measurements (lower plot). We see that the plateau shapes are negatively inclined, i.e. revealing lower conductance upon further stretching, as previously observed for some materials such as Pb (Cuevas et al., 1998), but different from the observations of other soft metals, like Au. However, some of the last plateaus reveal rising conductance upon stretching, as systematically observed for example in the case of Al (Scheer et al., 1997; Sánchez-Portal et al., 1997; Cuevas et al., 1998). Both effects, the falling and the rising last plateaus, are observed with both measurement techniques and are therefore attributed to intrinsic properties of Gd contacts. Another observation that appears in the traces recorded with both techniques is that upon creating the contact in most cases the conductance of the first contacts is higher than the

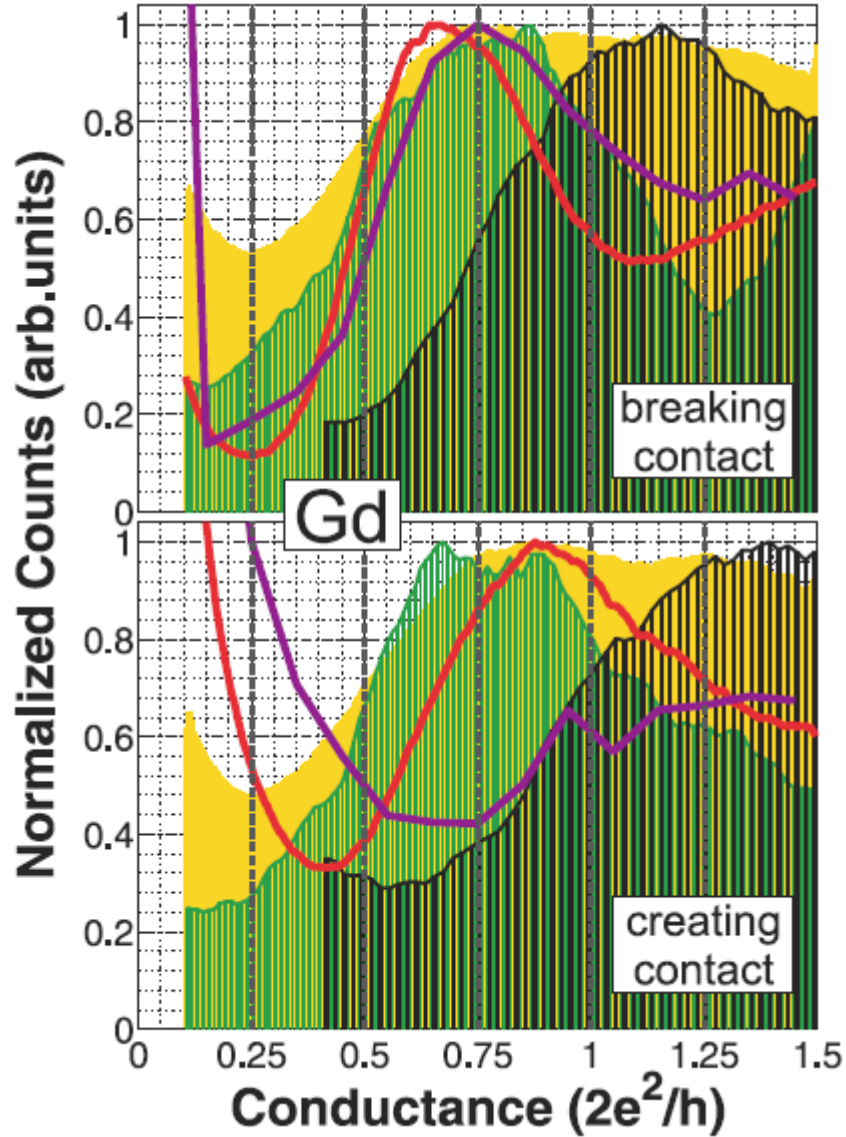


Figure 5.2: Histograms of conductance calculated from conductance traces for Gd atomic-size contacts. Upper/lower plot stands for breaking/closing contact mode. Same colors for upper and lower plot stand for a set of traces with electrodes that have not been modified with deep indentations (i.e. less than  $\approx 20 \frac{2e^2}{h}$ ). The different colors illustrate the variability in the histograms between contacts, or for different choices of depth of indentations. All measurements have been taken with STM technique at 100 mV bias voltage in equilibrium with liquid He bath and  $10^{-8}$  mbar, except the purple curve, that has been taken with MCBJ technique, where a bias voltage of 10 mV has been applied. For STM histograms few (from 1 to 10) thousands of traces are considered. For MCBJ  $\approx 500$  traces are included.

conductance of the last contact before breaking in the preceding trace. Furthermore, the backlash between breaking and creating the next contacts is somewhat larger in MCBJ technique, presumably because of the elastic deformation of the suspended

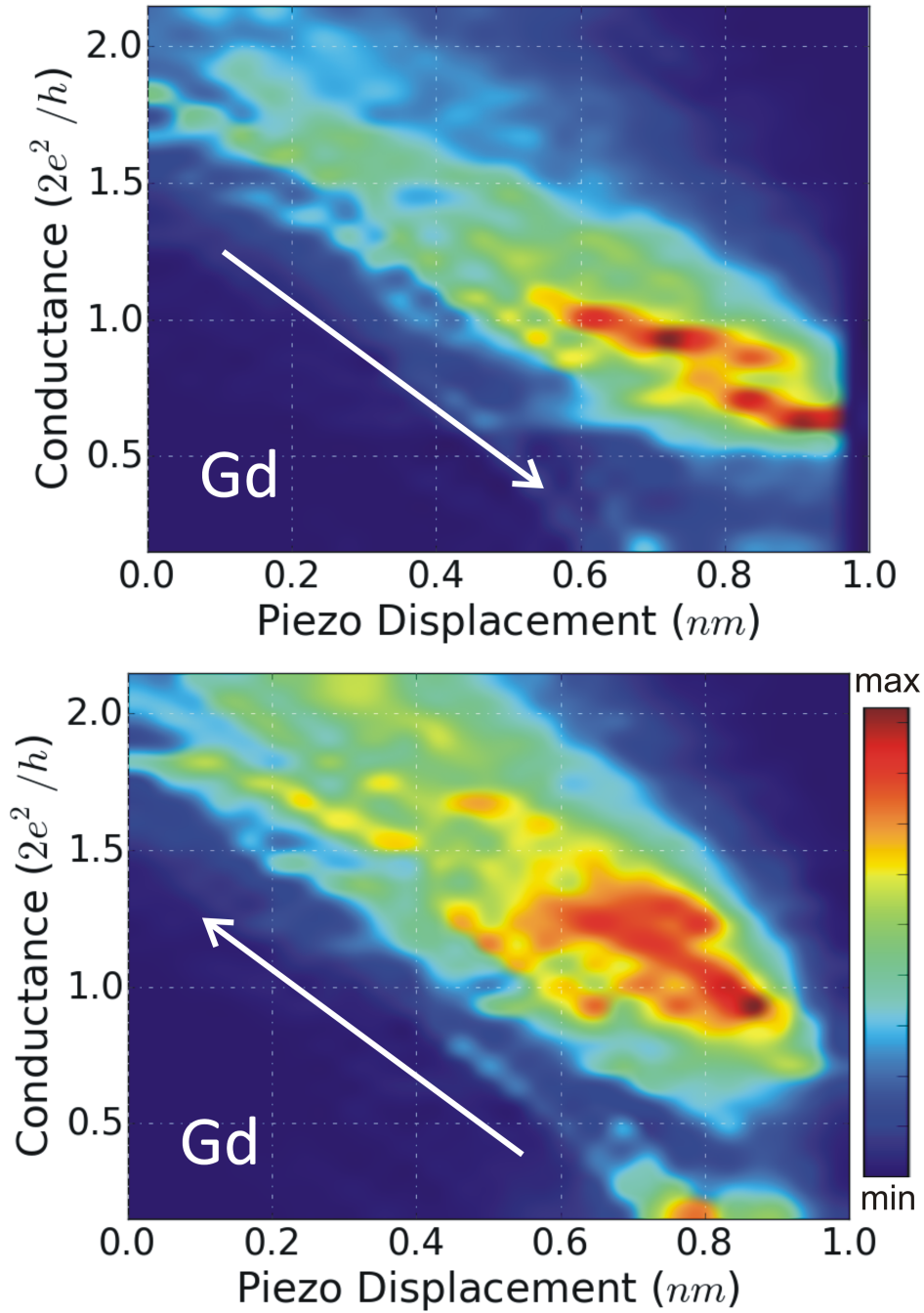


Figure 5.3: (Linear color scale) Overlapped Gd conductance traces measured with STM. Breaking contact (left-sided plot) and creating contact (right-sided plot) situations are shown. Traces are centered to 1 nm when  $0.01 \frac{2e^2}{h}$  is reached from higher/lower to lower/higher conductance values for breaking/creating contacts. Total number of traces are 2524 and 2511 for breaking and creating contact cases, respectively.

nanobridge. As a final remark, we have checked that these materials do not form long atomic chains when stretching.

Our results agree with those of Berg *et al.* (Berg, 2014) who reported values of  $(0.60 \pm 0.23) \frac{2e^2}{h}$  and  $(0.83 \pm 0.32) \frac{2e^2}{h}$  for the last plateau right before breaking (746 curves) and first one after creating (568 curves) the contact, respectively, of Gd notched-wire MCBJs 4.2 K. More details on the unpublished work by Berg *et al.* is given in the supplemental material. Similarly, low conductance values were also observed for Dy ( $(0.87 \pm 0.27) \frac{2e^2}{h}$  from 528 breaking traces). Reported measurements on nanocontacts made out of Dy (Marc Müller *et al.*, 2010) showed a non-trivial change of conductance as a function of the value of the external magnetic field. We observe similar but weaker magnetostrictive effect for some lithographic Gd MCBJ samples, in our case changing from sample to sample (see figure S1 at supplemental material).

From every set of traces with electrode indentations that have not reached conductance values above  $\approx 20 \frac{2e^2}{h}$ , we build up histograms. Some of them are shown in Fig. 5.2. For most well-studied metals (Au, Pt, Ni. . .) the position of the lowest maximum in the conductance histograms is very reproducible from experiment to experiment, although slight differences in the relative height and shape of the peaks have been reported (Agraït *et al.*, 1993; R. H. M. Smit & van Ruitenbeek, 2001; M. Reyes Calvo *et al.*, 2009). In the case of Gd the position of such histogram peaks shows a lower reproducibility, which we attribute to different configurations of the electrodes. At Fig. 5.2 we show five independent histograms (solid line, full color and vertical striped line patterns facilitate the identification of each one of them). We want to remark the strong resemblance between red (STM) and purple (MCBJ) breaking histograms. On the other hand, for MCBJ closing histograms, the first peak is located at higher conductance values suggesting that first MCBJ contacts are thicker than first contacts created with the STM. The yellow curve shows a very wide histogram, its corresponding traces were obtained with deeper indentations, meaning that a greater random rearrangement of the electrode tips was achieved. The black curve shows higher conductance values for both breaking and creating histograms. The contacts that account for this result were poorly sharpened, as could be noticed from the high slope of the conductance *vs.* displacement curves (Untiedt, Rubio, Vieira, & Agraït, 1997), meaning therefore that thicker tips are considered.

In addition, the last value of conductance before breaking contacts is well below that observed for other magnetic metals such as, e.g., Ni (M. Reyes Calvo *et al.*, 2009) where a mean value of conductance of  $\approx 1.5 \frac{2e^2}{h}$  is found.

In order to gain further insight into the evolution of conductance traces, we have constructed intensity maps as a function of both the conductance and the displacement of the electrodes for our measured data, shown in Fig. 5.3. This time, we collect all the conductance traces that we have measured with STM with indentations mostly up to  $20 \frac{2e^2}{h}$  and plot them in a two-dimensional histogram. In order to highlight the atomic-size contact area, we center the traces at the same value of piezo displacement for a chosen conductance value (see figure caption). This way of representing data permits to check the dispersion of data at the low conductance stages unveiling the dependence of the most probable conductance on the applied strain. At the right-sided edge of the represented cloud of data a dispersion of  $\approx 0.25 \frac{2e^2}{h}$  is clearly apparent, one quarter less than in the case of the conductance histograms in Fig. 5.2. For the closing curves the highest density is observed for the conductance  $(0.9 \pm 0.3) \frac{2e^2}{h}$ ,

while for the opening traces the distribution splits up into two branches, one ending with a conductance of  $(0.9 \pm 0.3) \frac{2e^2}{h}$  at slightly shorter distance and one ending at  $(0.65 \pm 0.20) \frac{2e^2}{h}$  at the rightmost extremity of the cloud. This finding indicates that longer contacts with lower conductance are formed when opening. With the calculations presented in the next section we will interpret the longer constrictions as dimeric configurations where two atoms in series form the constriction, while the shorter ones are single-atom or monomeric atomic configurations in which a single atom is surrounded by thicker electrodes to both sides. As we will discuss below, this may be unexpected, because of the presence of a  $s$  band at the Fermi energy, that normally contributes with one open channel per spin.

#### 5.4 THEORY

Density functional theory (DFT) calculations are initially carried out with the LAPW code ELK. Correlations in the  $f$  orbitals are treated using the DFT+U method in the Yukawa scheme (Bultmark, Cricchio, Grånäs, & Nordström, 2009) in the fully localized limit, to account for the strong correlations within the  $f$ -manifold. No correlations are introduced in the  $s$ ,  $p$ , and  $d$  manifolds due to their delocalized nature, well accounted for by more conventional functionals. Spin-orbit coupling is treated in the non-collinear formalism. Within this framework, the bulk lattice constant matches the experimental one within 3% deviation. To gain insight into the electronic structure in the constriction, we calculate the electronic structure of one-dimensional Gd chains and compare the differences driven by the reduced dimensionality. Chain structures are optimized in the lattice parameter.

The magnetic structure strongly changes upon reducing the dimensionality from bulk to a one-dimensional chain (Fig. 5.4). Whereas the bulk structures yield a total magnetic moment of  $\mu^{\text{bulk}} = 7.61\mu_B$ , one-dimensional chains show larger moments of  $\mu^{\text{chain}} = 8.9\mu_B$ . The projected density of states reveals that, whereas bulk structures have spin polarization mainly coming from the  $f$  levels plus a small contribution from  $s$  ones (not shown), chains show a stronger polarization in the  $d$  manifold arising from a stronger Stoner instability (see Fig. 5.4). This translates into energy differences between antiferromagnetic and ferromagnetic configurations,  $J = E_{AF} - E_{FE}$ , in chain structures which are much larger than the ones expected for bulk. Specifically we get  $J = 0.5$  eV, favoring a fairly stable ferromagnetic configuration. Notice that the strong exchange coupling in chains can be understood as a consequence of the direct  $d - d$  exchange coupling, whereas in bulk  $d$  magnetism barely appears in our calculations.

Transport calculations for Gd atomic contacts are also carried out. We have chosen simplified models with pyramidal forms growing along the  $\langle 111 \rangle$  direction for both sides of the nanocontacts (see inset at Fig. 5.1). The electron reservoirs, which make the nanocontact an open quantum system, are chosen to be Au electrodes. Au electrodes reduce the computational cost without introducing artifacts in the actual conductance of the model nanocontacts when these contain a large enough number of Gd atoms. The results presented below correspond to the minimum number of Gd atoms that needs to be considered (contacts with a larger number of Gd atoms have been studied, not finding significant differences). The transport methodology

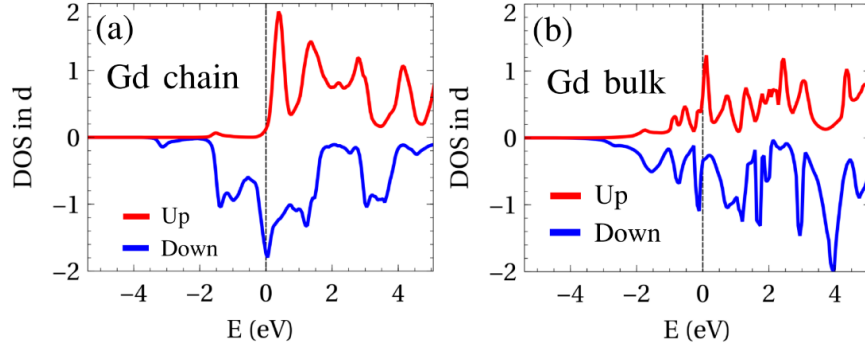


Figure 5.4: Spin resolved projected density of states onto the  $d$ -levels of Gd, in chain (a) and bulk (b) structures. Chain structures show net spin polarization in the  $d$ -manifold, apart from the one due to  $f$ -electrons. In comparison, bulk structures do not show polarization in the  $d$ -manifold, being the magnetism almost entirely due to localized  $f$ -levels.

is the well-known DFT-based non-equilibrium Green’s function formalism as implemented in the package ANT.G (JJ Palacios, Pérez-Jiménez, Louis, & Vergés, 2001; J. J. Palacios, Pérez-Jiménez, Louis, SanFabián, & Vergés, 2002; Louis, Vergés, Palacios, Pérez-Jiménez, & SanFabián, 2003; D Jacob & Palacios, 2011; David Jacob & Palacios, 2006). This software uses the DFT functionality of Gaussian09 (M. Frisch et al., 2009) to construct the one-particle Hamiltonian of the system. This Hamiltonian constitutes the basis for the implementation of the NEGF method through the Landauer-Keldysh formalism, which allows the simulation of open quantum systems connected to electron reservoirs.

The NEGF-DFT method implemented in ANT.G operates in the framework of linear combination of atomic orbitals (LCAO). Therefore, as a necessary first check, we need to compare with the well-grounded results of ELK. The basis “Stuttgart RSC 1997 ECP” has been used for Gd (Bergner, Dolg, Küchle, Stoll, & Preuß, 1993; Kaupp, Schleyer, Stoll, & Preuss, 1991; Dolg, Stoll, Preuss, & Pitzer, 1993) in the LCAO-DFT calculations for chain and nanocontact structures. This basis set includes ECP (energy-consistent pseudopotentials) to describe the interaction with the core-electrons. Due to the lack of a DFT+U implementation in the LCAO codes used, instead we make use of the hybrid functional HSE06 (Heyd & Scuseria, 2004) which also captures the strongly correlated nature of the  $f$ -levels. In this hybrid functional developed for metals the exchange energy term is split into short-range and long-range components and the Hartree-Fock long range is neglected but compensated by the PBE long range.

We compare the results obtained in two schemes for the DOS of the one-dimensional infinite chain (see Fig. 5.5). The LCAO calculations are performed with the code CRYSTAL14 (Dovesi et al., 2014) using the same basis set and functional as for the transport calculations shown below. We note that the spin splittings are slightly bigger in the LCAO method (around 20%) which also leads a more peaked resonance structure in the DOS. These differences can be traced back to the exact exchange present in the HSE06 functional calculations, which affect the four  $s$ ,  $p$ ,  $d$ , and  $f$  manifolds. In comparison, in the LAPW method, correlations included with the DFT+U scheme

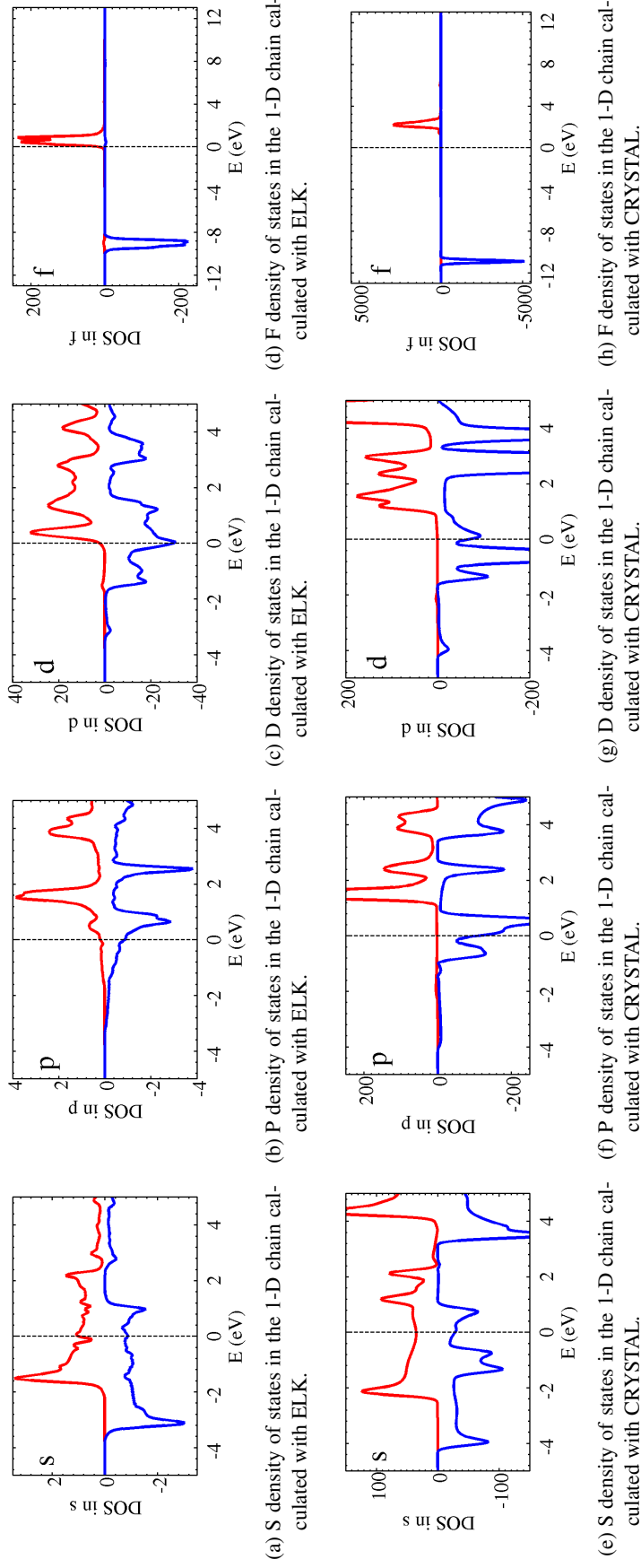


Figure 5.5: Spin resolved density of states of Gd in chain structures calculated with ELK (LAPW) projected onto the manifolds  $s$  (a),  $p$  (b),  $d$  (c) and  $f$  (d). Same cases calculated with CRYSTAL14 (LCAO) ( $s$  (e),  $p$  (f),  $d$  (g) and  $f$  (h)).

are introduced in the localized  $f$ -manifold but not in the delocalized  $s, p, d$  manifolds. In spite of these spectral differences, the magnetic moment calculated with both methods yields a similar value. Nevertheless, differences in the character of the electrons around the Fermi energy, which dominate the electronic transport, may yield different conductance values. By considering different functionals (with and without exact exchange) we have concluded that these differences are not significant in this regard.

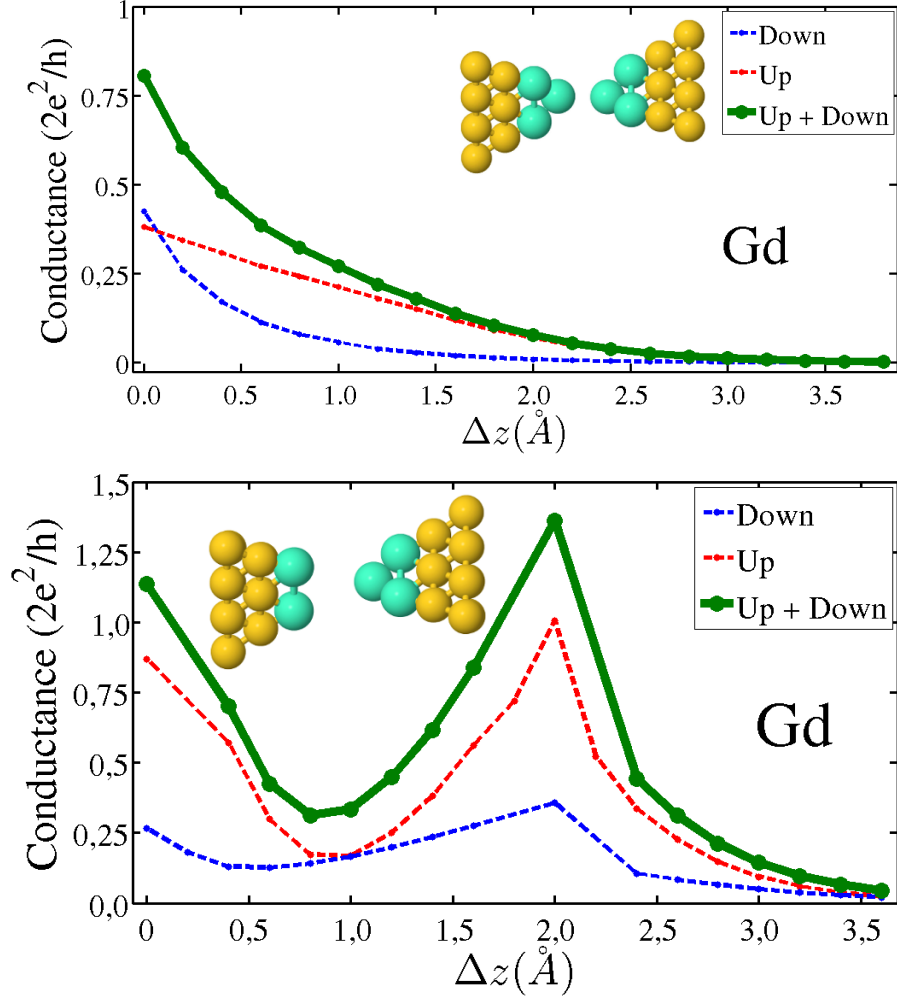


Figure 5.6: Gd  $\langle 111 \rangle$  nanocontact calculated conductance-distance characteristic. Upper plot: two atomically-sharp tips in the  $\langle 111 \rangle$  direction forming a dimeric contact. The distance  $\Delta z$  equals 0 when the distance between both tip apex atoms equals the n.n. distance in bulk. Lower plot: an atomically-sharp tip in the  $\langle 111 \rangle$  direction against a blunt  $\langle 111 \rangle$  one. Both tips touch to form a monomeric contact. The distance  $\Delta z$  equals 0 when the distance between the tip apex atom in the atomically-sharp tip and each tip apex atom in the blunt one equals the n.n. distance in bulk.

In the following, I present the results obtained for the conductance in the LCAO scheme using the HSE06 functional. The calculated conductance-distance characteristics for Gd nanocontacts are shown in Fig. 5.6 for both monomer and dimer configurations (see insets in Fig. 5.6). As anticipated in the discussion of the experimental

results, monomer and dimer configurations are expected to form when breaking the contacts while in most of the cases only monomers are expected to appear when forming the contacts. The piezo displacement is simulated by opposite displacement of the two tips, while keeping their atomic structure intact. Thus, we do not make any distinction between breaking and creating contacts, although a small difference in the average atomic bond distance is expected between the two processes if relaxation were allowed. Relaxation would also permit to simulate the plasticity effects (jumps in conductance), as seen in this type of experiments. This is, however, computationally too costly since a large number of Gd atoms are required and beyond the scope of our discussion here.

As their periodic counterparts (bulk and chains), Gd nanocontacts show a purely ferromagnetic behavior all along the breaking process. Anti-parallel magnetic configurations (between the two tips) show smaller conductance values, but these magnetic states have a higher energy and tend to relax into the ferromagnetic ones. The current is spin-polarized with a dominant contribution from the minority channel (spin-up here in red) for stretched dimeric contacts and from the majority one (spin-down in blue) for monomeric contacts. The calculated total conductance at bulk near-neighbor distance between tip apex atoms (or zero displacement,  $\Delta z = 0$ ) is  $0.80 \frac{2e^2}{h}$  for the dimer and  $1.15 \frac{2e^2}{h}$  for the monomer contacts. Both values, along with the ones nearby for small displacements (representing actual stretched contacts) fall within their tentatively assigned experimental bright spots seen in Fig. 5.3. Notice that, due to lack of relaxation in our calculations, longer displacements may not represent actual atomic configurations since sudden plastic deformations must occur. Even so, for the monomer configuration we obtain an increase of conductance as the tip-tip distance increases which is of purely electronic origin and could be tentatively related to the one often observed in the experiments [see Fig. 5.6(b)].

A deeper insight into the electronic nature of transport can be revealed by analyzing the nature of the eigenchannels (David Jacob & Palacios, 2006) involved in the conductance. In Figs. 5.7a, 5.7b and 5.7c we plot the conductance of the spin up and spin down dominant eigenchannels for three representative examples. We have chosen: (a) a dimer contact at a displacement of  $\Delta = 1.0$  and (b) a monomer contact at a displacement of  $\Delta = 1.0$  and (c)  $\Delta = 2.2$ . In general, the eigenchannels do not show a dominant  $s$  character. For the case (a) they display mostly a  $p_z$  character (minority) or  $sp_z$  character (majority).

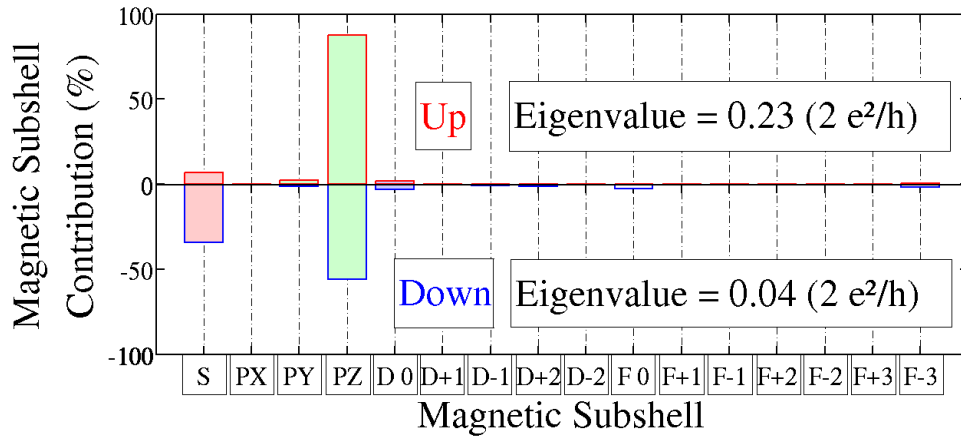
In the monomer case, in addition to the  $sp_z$  hybridization (Cuevas et al., 1998; Scheer et al., 1997), the transition from  $sp_z$ -like eigenchannels at smaller displacements (Fig. 5.7b) to an eigenchannel with a strong  $d$  character for majority spins 5.7c at larger displacements seems to also play a role in the change of the slope of the conductance traces, as seen in 5.6(b). No direct contribution from  $f$  orbitals appears in transport, apart from enhancing the spin polarization in the other subshells, as expected from their localized nature. We finally emphasize that the previous analysis relies on the assumption that the LCAO+HSE method properly captures the electronic structure around the Fermi energy for the rare earth compound, which could change using other DFT schemes. The accuracy of our method is subject therefore to its test by more sophisticated methods, capable of capturing simultaneously the metallic behavior and strongly localized states in these rare earth chains.

In Figs. 5.7a, 5.7b and 5.7c, “Up” electrons correspond to the “minority” spin component while “down” electrons to the “majority” one.

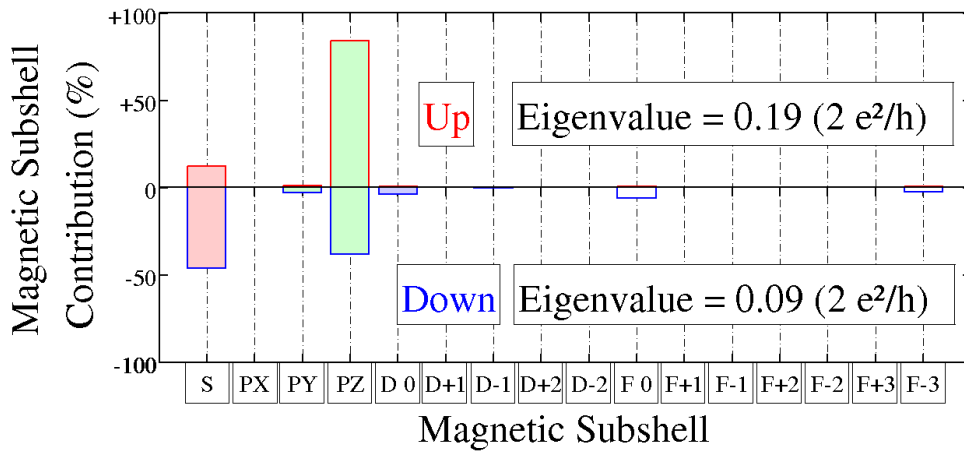
## 5.5 CONCLUSIONS

We have carried out electrical current transport on atomic-size contacts made out of Gd under cryogenic conditions. Unlike the case of 3d ferromagnetic materials and despite the  $d^1$  valence of Gd, their single atom conductance is typically smaller than  $\frac{2e^2}{h}$ . This might be at first sight surprising, because in both cases there is a wide  $s$ -band at the Fermi energy, which normally provides a highly transmissive channel and which, along with an additional contribution coming from the  $d$  channels, may give conductance values above  $\frac{2e^2}{h}$ . However, in the case of Gd, the transmission of all channels are reduced presumably to the position of the Fermi energy close to the edges of the respective bands. The results are reproducible for both STM and MCBJ measurements in many details: lengths of plateaus, shapes of plateaus, position and height of histogram maxima, differences between creating and breaking curves. . . .

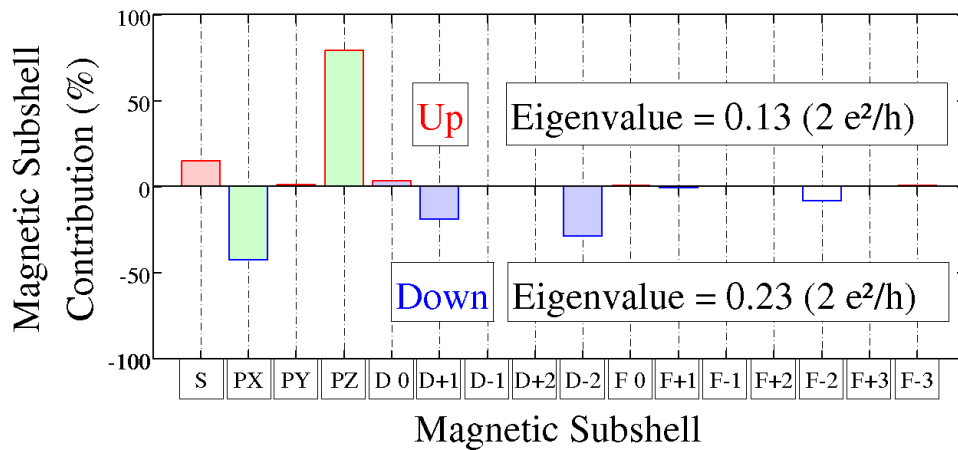
Our DFT calculations show that, apart from the  $f$ -magnetism, the dimensionality reduction of the nanocontacts creates a spin splitting in the  $d$ -manifold, in comparison with bulk structures where the  $d$ -manifold remains nearly unpolarized. Using the non-equilibrium Green function formalism within the LCAO+HSE06 scheme we generically obtain conductance values smaller than  $\frac{2e^2}{h}$ , with differences between monomer and dimer configurations. The analysis of the eigenchannels shows that this is due to a hybridization of the  $s$  and  $p_z$  channels, which apparently reduces the conductance of a pure  $s$  channel. This is also in line with the increasing conductance on the last plateau as the electrodes are pulled apart, which has also been observed in Al atomic contacts and for which the  $sp_z$  hybridization is also known to play a role. In the case of Gd, the  $d$  orbitals also seem to play a role in this conductance rise. Finally, our zero-bias measurements do not seem to be strongly influenced by the large  $f$  local magnetic moments, firstly because  $f$  electrons do not participate in conduction and, secondly, the stable ferromagnetic configuration will avoid electric conductance variations due to magnetic disorder.



(a) Spin resolved principal eigenchannel projected onto all the magnetic shells of a Gd dimeric nanocontact at a tip-tip displacement of 1.0.



(b) Spin resolved principal eigenchannel projected onto all the magnetic shells of a Gd monomeric contact at tip-tip displacement of  $\Delta z = 1.0$ .



(c) Spin resolved principal eigenchannel projected onto all the magnetic shells of a Gd monomeric contact at tip-tip displacement of  $\Delta z = 2.2$ .

Figure 5.7: Spin resolved principal eigenchannels

## 6.1 ABSTRACT

A low-temperature scanning tunneling microscope was used to fabricate atomic contacts on Pb(111). Conductance characteristics of the junctions were simultaneously recorded with forming and subsequent breaking of the contacts. A pronounced hysteresis effect in conductance traces was observed from junctions comprising the clean Pb(111) surface. The hysteretic behavior was less profound in contacts to single Pb atoms adsorbed to Pb(111). Density functional calculations were able to reproduce the experimental results by performing a full ab-initio modeling of plastic junction deformations. A comprehensive description of the experimental findings was achieved by considering different atomic tip apex geometries, as been published in (M. Müller, Salgado, Néel, Palacios, & Kröger, 2016).

## 6.2 INTRODUCTION

Electrical contacts with constrictions at the atomic scale are receiving substantial attention owing to their importance in fundamental and applied sciences. (Nicolás Agrait, Yeyati, & van Ruitenbeek, 2003; Kröger, Néel, & Limot, 2008; Berndt, Kröger, Néel, & Schull, 2010) In particular, molecular spintronics, (Sanvito, 2011) spin caloritronics (Bauer, Saitph, & van Wees, 2012) and thermoelectric effects in nanoscale junctions (Dubí & Di Ventra, 2011) are emerging fields. To these investigations structural and mechanical properties of the junctions are relevant since electron transport depends crucially on the contact geometry. (Wang et al., 2010; Schull, Frederiksen, Arnau, Sánchez-Portal, & Berndt, 2011)

A wealth of experimental and theoretical works has been reported for Au contacts, (Nicolás Agrait et al., 2003) presumably due to their propensity to form monoatomic chains bridging the electrodes. (Ohnishi et al., 1998; A. I. Yanson, Bollinger, van den Brom, Agrait, & van Ruitenbeek, 1998)

By appropriate treatment of Au electrodes in break-junction experiments hysteretic loops were reproducibly observed in conductance-versus-distance traces that were simultaneously recorded with closing and opening of the junctions. (Trouwborst, Huisman, Bakker, Van Der Molen, & Van Wees, 2008) This observation was traced to the elasticity of the electrodes.

To our knowledge this work (Trouwborst et al., 2008) represents the only combination of experimentally observed and theoretically described hysteretic conductance behavior between tunneling and contact regime of single-atom junctions that has been available to date. Other materials that have often been used in contact experiments are Ni, Cu, Pd, Ag, Al and Pt. (Nicolás Agrait et al., 2003)

For some of these materials conductance hysteresis upon opening high-conductance junctions were reported. (N. Agrait, Rodrigo, Rubio, Sirvent, & Vieira, 1994; den

Brom, Yanson, & Ruitenbeek, 1998a; Halbritter et al., 2002; Rodrigo, Suderow, Vieira, Bascones, & Guinea, 2004)

However, investigations of the contact formation and breaking of atom-sized Pb junctions are scarce. In an early work W tips of a scanning tunneling microscope (STM) were approached to Pb(110) and neck formation was investigated at different sample temperatures (Kuipers & Frenken, 1993). Neck heights exceeding 500 nm were reported and their growth was rationalized in terms of mobile surface atoms. In another experiment polycrystalline Pb tips and samples were used to study the conductance of Pb junctions depending on the forces exerted on the electrodes. (N. Agrait et al., 1994) A jump to contact was observed upon approaching the tip to the sample surface. The resulting junction conductance of less than one quantum of conductance,  $G_0 = 2e^2/h$  ( $e$ : elementary charge,  $h$ : Planck constant), was rationalized in terms of constrictions comprising about one atom. In addition, conductance hysteresis was reported after indenting the tip into the substrate, thereby increasing the junction conductance to  $\approx 10 G_0$ , and subsequent retraction of the tip. The contact area was appreciably modified by forming asperities with diameters on the order of 100 nm. In a break junction experiment Pb–Pb contacts were stretched until an abrupt decrease of the conductance occurred from  $\approx 1 - 3 G_0$  to typical tunneling conductances. (Scheer et al., 1998) Tight-binding calculations assuming a simple pyramid-based geometry for the electrodes confirmed conductance values of  $\approx 2.5 G_0$  as a result of electron transport through  $sp_z, p_x, p_y$  orbitals of the Pb atom bridging the electrodes.

In the ballistic electron transport range, STM experiments revealed that contact formation between Pb-covered W tips and thin films of Pb on Ag(111) depended on the film thickness (Becker & Berndt, 2010). While a gradual transition from tunneling to contact was observed for the single Pb wetting layer, the transitions became more abrupt for thicker films. Conductances of contacts comprising the single Pb wetting layer as well as several layers were broadly distributed around  $\approx 2 G_0$ . For Pb(111) films on Si(111) atomically resolved conductance traces were obtained by using Pb-coated PtIr tips. (Kim & Hasegawa, 2015) On-top, bridge, face-centered cubic and hexagonal close-packed sites of the Pb(111) lattice led to different conductances in the range of  $\approx 1 - 1.3 G_0$ .

In a broader context, Pb junctions in electrochemical environments were investigated and the findings compared with density functional calculations revealing the importance of the contact geometry for the conductance. (Xie et al., 2010) Pb junctions exposed to external magnetic fields were probed revealing the influence of the geometry on the superconducting properties. (Rodrigo, Crespo, Suderow, Vieira, & Guinea, 2012) Moreover, atomic Pb wires were grown on a vicinal semiconductor surface and demonstrated to exhibit correlated spin-orbit order. (Brand et al., 2015) In tunneling junctions comprising Pb electrodes the competition of superconducting phenomena and Kondo screening (Franke, Schulze, & Pascual, 2011) as well as tunneling processes into localized subgap states were unraveled. (Ruby, Pientka, et al., 2015)

Here, we present our findings for single-atom contacts fabricated from Pb-covered W tips and a Pb(111) surface in a low-temperature STM experiment. The forming and breaking of junctions was performed on pristine Pb(111) as well as on single Pb adsorbed atoms (adatoms). Simultaneously, the conductance of the junction was

recorded for tip–sample distances in tunneling and contact ranges. Both types of junctions exhibited a rather broad distribution of contact conductances, *i. e.*, from  $1 G_0$  to  $5 G_0$  for Pb(111) and from  $0.7 G_0$  to  $3 G_0$  for Pb adatoms. These distributions are not compatible with the previous tight-binding calculations for a single-atom Pb junction where conductance variations from  $1 G_0$  to  $2.5 G_0$  depending on the distance between the central atom and its first neighbors were reported (Cuevas et al., 1998). In addition, both junctions showed hysteretic behavior. Breaking of the contacts on clean Pb(111) required tip retractions by up to hundreds of pm beyond the jump to contact. Contact regions were imaged prior to and after contact experiments in order to identify surface and tip modifications. The experimental results were corroborated by state-of-the-art ab initio quantum mechanical simulations. The calculations unveiled the important role of relaxations of the tip structure on the contact conductance and the hysteresis width. Atomically sharp and crystalline tips alone were unable to explain the experimental observations. Rather, tip apices terminated by more than one atom had additionally to be considered to comprehensively describe the experimentally observed contact conductances and hysteresis effects.

### 6.3 EXPERIMENTAL

The experiments were performed with an STM operated in ultrahigh vacuum ( $10^{-9}$  Pa). The absence of the superconducting energy gap in spectra of the differential conductance together with the temperature readings from a Si diode indicated a sample temperature of 7.2 K – 7.5 K. Pb(111) was cleaned by  $\text{Ar}^+$  bombardment and annealing. Tips were electrochemically etched from polycrystalline W wire (diameter  $300 \mu\text{m}$ , purity 99.95 %) in a 0.1 M solution of NaOH. In the vacuum recipient the tips were heated close to the W melting temperature. The tip apex was then coated with substrate material by indentation into the Pb(111) surface with an applied voltage of 130 V. A similar procedure was reported previously, which ensured the bulk-like character of the Pb coating by measuring the superconducting energy gap. (Ruby, Heinrich, Pascual, & Franke, 2015)<sup>1</sup> Tip–surface contacts were formed by disabling the feedback loop at a tunneling current of 0.5 nA, at a bias voltage between  $-50$  mV and 50 mV, and approaching the tip by 300–600 pm towards the surface. The tip approach was stopped a few tens of picometers after the first jump to contact. The tip was then retracted by 1 nm. Approach and retraction velocities ranged between  $2 \text{ nm s}^{-1}$  and  $3 \text{ nm s}^{-1}$ . For the contact experiments a specific selection of tips was used. The tip was approached to the surface until a single Pb atom was transferred from the tip to the sample upon contact. Atom transfer from the tip apex to the surface was reported previously for several surfaces (Limot, Kröger, Berndt, Garcia-Lekue, & Hofer, n.d.; Kröger, Jensen, & Berndt, 2007; Kröger et al., 2008; Kröger, Néel, Sperl, Wang, & Berndt, 2009; Berndt et al., 2010) and is due to the strong adhesive forces between the electrodes close to the point of maximum attraction. Such tips were particularly stable and led to reproducible conductance traces and STM images prior to and after contact formation. STM images were recorded at constant current with the bias voltage applied to the sample. For measurements with a time resolution

<sup>1</sup> Experiments were likewise performed with bulk Pb tips. The resulting junctions exhibited virtually identical behavior to the contacts with Pb-covered W tips.

of 20 ns a transimpedance amplifier with a 3 dB cut-off frequency of 14 MHz and an oscilloscope sampling rate of  $50 \text{ MS s}^{-1}$  were used.

#### 6.4 RESULTS AND DISCUSSION

Tip approach to the clean Pb(111) surface gave rise to the evolution of the junction conductance depicted as the black line in Fig. 6.1(a). The tunneling range in the vicinity of the transition to contact ( $-100 \text{ pm} < \Delta z < 0 \text{ pm}$ ) was characterized by an exponential increase of the conductance with an apparent barrier height of  $(5.0 \pm 0.5) \text{ eV}$ . This value is larger than the Pb(111) work function of  $4.05 \text{ eV}$ . (Jacobi, 1988) The deviation is in accordance with the previously reported increase of the apparent barrier height close to contact formation on thin Pb films on Ag(111). (Becker & Berndt, 2010) Indeed, the calculations presented below revealed strong atomic relaxations in the vicinity of the tunneling-to-contact transition, which caused the tip-surface distance to vary more strongly than the tip displacement.

The transition from the tunneling range to the contact range was reflected by an abrupt increase of the junction conductance. Time-resolved measurements of the jump to contact revealed that the transition was abrupt on a time scale of 20 ns. This almost discontinuous tunneling-to-contact transition was used to define  $\Delta z = 0 \text{ pm}$  [Fig. 6.1(a)]. These observations are compatible with the emerging trend reported previously. (Becker & Berndt, 2010) While for a single wetting layer of Pb on Ag(111) the transition from the tunneling to the contact range was gradual, it turned into a more abrupt cross-over region for thicker Pb films. (Becker & Berndt, 2010) Therefore, a jump to contact for bulk Pb may be expected and was observed in our experiments. The conductances just before [ $G_j$ , Fig. 6.1(a)] and after ( $G_c$ ) the jump did not depend on the applied bias voltage in the range of  $-50 \text{ mV}$  to  $50 \text{ mV}$ . Tunneling spectra of the differential conductance were featureless and nearly constant in that voltage interval.

In the subsequent contact range, i. e., for  $\Delta z > 0 \text{ pm}$ , the conductance exhibited a linear increase. Upon tip retraction the junction conductance decreased linearly [gray line in Fig. 6.1(a)] several hundreds of pm beyond the precedent point of contact formation, i. e., the conductance displayed a pronounced hysteretic behavior. The conductance decrease in the contact range ( $\Delta z < 0 \text{ pm}$ ) were reported previously and rationalized in terms of the splitting of Pb  $p$  orbitals at the Fermi level due to elastic distortions of the contact. (Cuevas et al., 1998) During retraction of the tip two-level fluctuations of the conductance were often observed [dashed rectangle in Fig. 6.1(a)]. Data acquisition with high time resolution [inset to Fig. 6.1(a)] revealed that the fluctuations were abrupt changes between two conductance values, which may be attributed to atomic relaxations in the junction. (den Brom, Yanson, & Ruitenbeek, 1998b; Sperl, Kröger, & Berndt, 2010; Néel, Kröger, & Berndt, 2011) Local heating of the junction due to power dissipation in the  $\mu\text{W}$  range is likely to be present. For Au junctions a temperature increase of  $50 \text{ mK}$  was unraveled for this power dissipation. (Lee et al., 2013) On general grounds, in the case of electron and hole injection into pure metal a temperature increase on the order of  $1 \text{ mK}$  may be estimated for the used currents and bias voltages assuming that electrons and holes deposit their energy within the inelastic mean free path. (Flores, Echenique, & Ritchie,

evolution-of-a-junction-comprising-Pb-111-Figure1.pdf

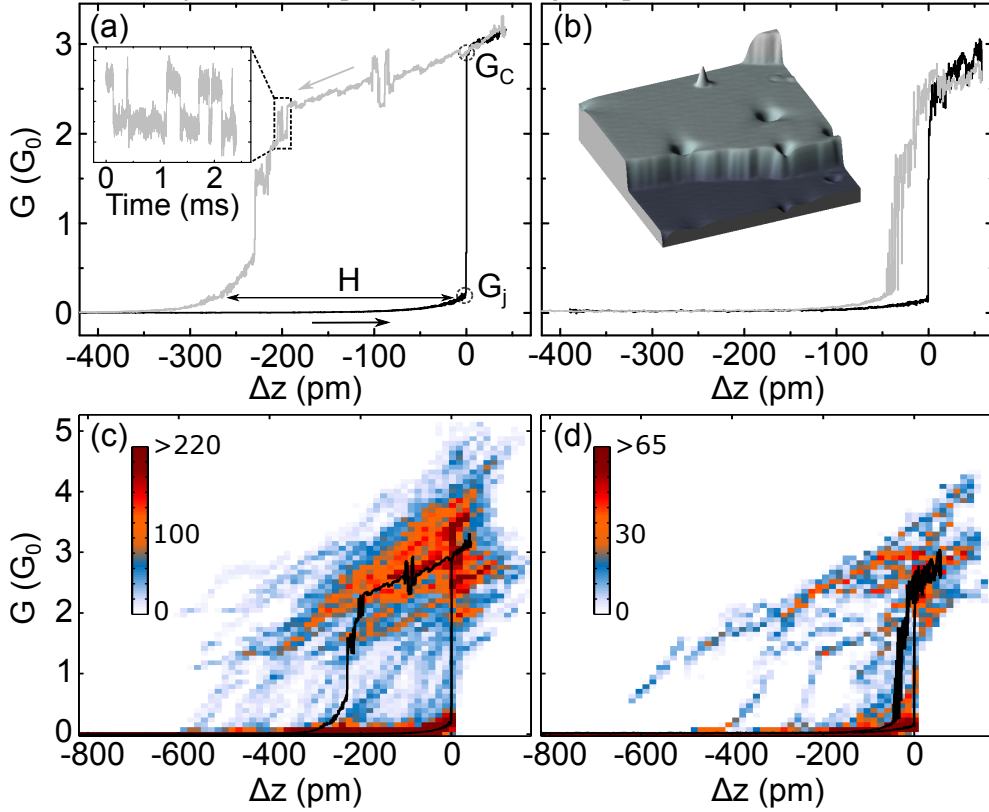


Figure 6.1: (a) Representative conductance evolution of a junction comprising Pb(111) and a Pb-coated W tip acquired at 50 mV. Tip approach (black line) leads to an exponential increase of the conductance in the tunneling range (displacements  $\Delta z < 0$  pm). The abrupt change of the conductance from  $G_j = 0.2 G_0$  to  $G_c = 2.9 G_0$  at  $\Delta z = 0$  pm reflects the formation of the contact. In the probed contact range ( $\Delta z > 0$  pm) the conductance increases linearly. Upon tip retraction (gray line) the conductance decreases linearly and reveals instabilities in the form of, e. g., two-level fluctuations (dashed rectangle). The definition of the hysteresis width,  $H$ , is indicated. Inset: Two-level fluctuations observed in the conductance trace upon tip retraction. (b) As (a) for a contact to a single Pb adatom on Pb(111) with  $G_j = 0.1 G_0$  and  $G_c = 2.2 G_0$ . Inset: Pseudo-three-dimensional representation of an STM image of Pb(111) (0.1 V, 55 pA, 50 nm  $\times$  50 nm). Two terraces are visible. A Pb adatom appears as a protrusion on the upper terrace. Additional structure is due to near-surface voids induced by  $\text{Ar}^+$  bombardment. (Schmid, Hebenstreit, Varga, & Crampin, 1996; Kurnosikov, Adam, Swagten, De Jonge, & Koopmans, 2008) Image processing was performed by Nanotec WSxM. (Horcas et al., 2007) (c), (d) Density plots of all acquired conductance traces [137 for Pb(111), 19 for single Pb adatoms]. The color scale depicts the number of conductance data linearly grouped into bins defined by a regular  $90 \times 90$  grid, which was spanned from  $-1090$  pm to 260 pm and from  $0 G_0$  to  $7 G_0$ . Full lines are the conductance traces shown in (a), (b).

1986) This temperature increase is not sufficient to surpass Ehrlich-Schwoebel barriers (86 meV) (Li, Han, Jia, Xue, & Liu, 2006) and kink energies per atom (61–87 meV) (Arenhold, Surnev, Bonzel, & Wynblatt, 1999) of Pb(111). Therefore, local heating of the junction does not represent the main driving mechanism for the observed junction instabilities. Importantly, after acquiring a typical conductance trace on Pb(111) [Fig. 6.1(a)] STM images of the contact area showed that in most cases a single atom was transferred from the tip to the surfaces. In less frequent cases a Pb dimer was transferred.

Contact experiments on single Pb adatoms were likewise performed. Single Pb atoms were transferred from the tip to the Pb(111) surface, as reported previously for other surfaces. (Limot et al., n.d.; Kröger et al., 2007; Kröger et al., 2008; Kröger et al., 2009; Berndt et al., 2010) The inset to Fig. 6.1(b) shows an STM image of Pb(111) where a single adatom is visible as a protrusion on the upper terrace. The tip approach to a single Pb adatom exhibited an abrupt change of the conductance at the tunneling-to-contact transition and a linear variation of the conductance in the contact range. A hysteresis loop of the conductance was observed for the adatom, too, albeit considerably less pronounced than on clean Pb(111). A representative example is shown in Fig. 6.1(b) in which the conductance hysteresis appears with a width of  $\approx 50$  pm. Imaging the adatom after conductance data acquisition showed that no material had been transferred to the surface.

While the conductance traces in Figs. 6.1(a), (b) represent specific data sets Figs. 6.1(c), (d) comprise all conductance data as density plots. These density plots illustrate the propensity of single-adatom contacts to exhibit smaller conductance hysteresis widths than junctions on clean Pb(111) surfaces. For clarity the data sets of Figs. 6.1(a), (b) were added to the density plots as black lines.

Statistics were performed for the contact conductance,  $G_c$ , and the hysteresis width,  $H$ , in order to more thoroughly compare contact experiments on clean Pb(111) and on single Pb adatoms on Pb(111). To this end  $G_c$  was defined as the conductance value that is reached directly after the jump to contact. The hysteresis width was defined as follows [Fig. 6.1(a)]. A horizontal line starting from  $G_j$  – the conductance just before the jump to contact – intersects the conductance trace acquired during retraction. The difference of the corresponding displacements is referred to as  $H$ .

Figures 6.2(a), (b) show histograms of  $G_c$  obtained for contacts comprising Pb-covered W tips and the clean Pb(111) surface [Fig. 6.2(a)] and single Pb adatoms on Pb(111) [Fig. 6.2(b)]. The distribution of  $G_c$  for contacts on Pb(111) exhibited a broad maximum at  $\approx 2.5 G_0$ . Contacts on three-layer thick Pb films on Ag(111) were previously reported to exhibit similar conductances. (Becker & Berndt, 2010) However, these contact conductances were observed less frequently than contact conductances of  $\approx 1.4 G_0$ . (Becker & Berndt, 2010) Junctions comprising a single Pb adatom showed a maximum in the histogram of  $G_c$  that is more sharply peaked between  $2 G_0$  and  $2.25 G_0$ . The different widths of the conductance histograms are assigned to the degree of precise knowledge of the contact geometry. The Pb(111) surface was not imaged with atomic resolution. Therefore, whether contact was formed to on-top, hollow or bridge lattice sites of Pb(111) remained elusive. In contrast, contact to the adatom left less doubt to the junction geometry at the substrate and thus led to a sharper distribution of  $G_c$ . These findings are in agreement with results obtained

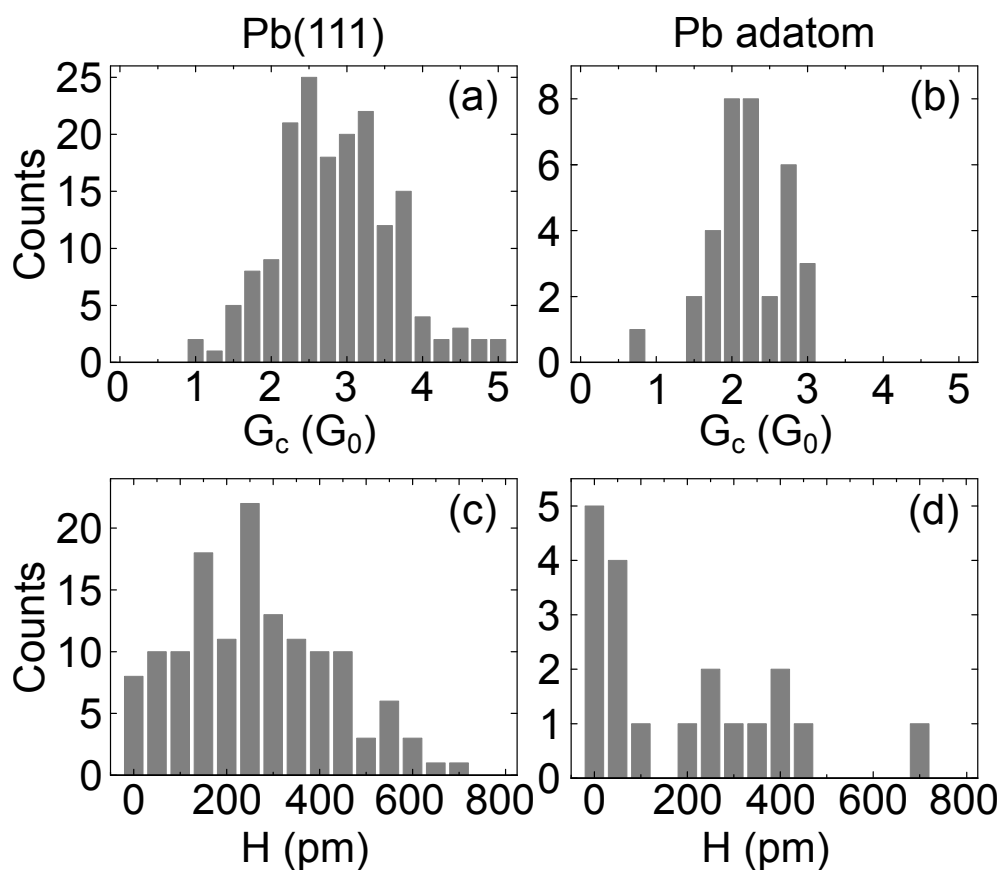


Figure 6.2: Histograms of observed contact conductances ( $G_c$ ) on pristine Pb(111) (a) and on single Pb adatoms (b). (c), (d) Histograms of hysteresis widths ( $H$ ) observed from closing and subsequent breaking of junctions comprising Pb(111) and single Pb adatoms, respectively. All contacts were formed with bias voltages ranging from  $-50$  mV to  $50$  mV.

for Ag(111), Cu(111) (Limot et al., n.d.) and Au(111). (Kröger et al., 2007; Kröger et al., 2009) Below we will show that contact conductances calculated for different lattice sites and tip geometries corroborate the experimental results (Table 6.1).

Histograms of the hysteresis widths are different for Pb(111) [Fig. 6.2(c)] and Pb adatoms [Fig. 6.2(d)], too. For contacts on clean Pb(111) the distribution is broad with a maximum at  $\approx 250$  pm. Junctions comprising Pb adatoms most frequently exhibit conductance hysteresis widths between 0 pm and 50 pm. In the probed bias voltage range  $10 \text{ mV} \leq |V| \leq 50 \text{ mV}$  and within the uncertainty margins the hysteresis width did not depend on the sample voltage. Moreover, the potential influence of Pb phonons was not explored since bulk and surface phonon energies are below 10 meV. (Sklyadneva, Heid, Bohnen, Echenique, & Chulkov, 2012)

For both contact types breaking of the junctions was accompanied by conductance instabilities before the jump out of contact occurred. These findings are different from results reported for Au contacts. (Trouwborst et al., 2008) The hysteretic conductance variations in Au contacts were characterized by clear jumps to contact and jumps out of contact. Stretching of the Au junctions led to a gradual decrease of the conductance without the occurrence of conductance fluctuations. These observations were rationalized in terms of junctions in which no further atomic reorganizations took place, i. e., the closing and opening of the Au contacts was understood by elastic deformations of the electrodes. (Trouwborst et al., 2008) For Pb, however, our *ab-initio* quantum mechanical calculations showed that reorganizations of the electrode structure occurred, i. e., the junctions were characterized by plastic deformations. In particular, several atoms were involved in forming and breaking of the contact. This interpretation is compatible with our observation that the hysteresis width slightly increased with increasing contact conductance (not shown).

In order to rationalize the experimental data and gain insight into the relation between the mechanical or structural properties and the conductance of the contacts, a full set of density functional calculations was performed. While it is common practice to address the mechanical behavior of contacts at the nanometer scale through molecular dynamics and effective interatomic potentials, (Sabater, Untiedt, Palacios, & Caturla, 2012) the detailed and controlled nature of the present experiments called for taking quantum effects on the forces into account. Both the mechanical behavior and the electron transport were addressed by means of our code ANT.G (J. J. Palacios et al., 2002; Louis et al., 2003) in combination with Gaussian. (M. J. Frisch, Trucks, Schlegel, Scuseria, Robb, Cheeseman, Scalmani, Barone, Mennucci, Petersson, Nakatsuji, Caricato, Li, Hratchian, Izmaylov, Bloino, Zheng, Sonnenberg, Hada, Ehara, Toyota, Fukuda, Hasegawa, Ishida, Nakajima, Honda, Kitao, Nakai, Vreven, Montgomery, et al., 2009) The atomic and electronic structure of the relevant contact region were obtained in a fully self-consistent manner and translated into a conductance through a standard Green function formalism with the help of effective self-energies representing the far and less relevant part of the system. (J. J. Palacios et al., 2001; J. J. Palacios et al., 2002; Louis et al., 2003; D. Jacob & Palacios, 2011) To expand the electronic density and represent the Green function, the CRENS minimal basis set was typically used, with one *s* and three *p* orbitals, including its corresponding core pseudo-potentials. (Ross et al., 1990) Additionally, calculations with larger basis sets such as the LANL2DZ were performed. (Wadt & Hay, 1985) However,

the resulting atomic and electronic properties were virtually identical to the findings obtained by the minimal basis sets. A standard local density approximation to the density functional was used. The choice of the functional is not critical to the results for mono-elemental *sp* metals. The specific procedure to mimic the experiments involved successive instantaneous structural relaxations subject to certain geometrical constraints on the boundary atoms of our system which coupled to the bulk substrate and the rest of the tip.

The geometry of the surface and of the contact was known to a very good extent owing to the imaging capabilities of the STM. However, to reduce the large number of possible atomic coordinates the starting atomic structure of the tip prior to contact had in part to be guessed. For all calculations a pyramidal Pb tip grown in the  $\langle 100 \rangle$  direction was chosen. This choice was motivated by the findings of several previous works. Pb tips grown along  $\langle 100 \rangle$  directions exhibit  $\{111\}$  facets, which were shown to exhibit the lowest surface energy. (Zhang, Ma, & Xu, 2004) Further, Pb electrodes stacked along  $\langle 100 \rangle$  directions gave rise to contact conductances of  $2.7 G_0$ , (Xie et al., 2010) in good agreement with our observations. Face-centered cubic metals in general realize  $\langle 100 \rangle$  stacking directions, which was demonstrated for, *e. g.*, Au (Ohnishi et al., 1998; Rodrigues, Fuhrer, & Ugarte, 2000; Rego, Rocha, Rodrigues, Ugarte, & Rego, 2003; Evangeli et al., 2015), Al (Schirm et al., 2013) and Pt (Evangeli et al., 2015) electrodes. Although  $\langle 111 \rangle$  growth directions are also likely to appear, qualitatively different physics was not unraveled from several tests carried out. Consequently, two obvious choices for the tip termination were available, *i. e.*, the commonly assumed single-atom termination and a termination via a four-atom plane parallel to the surface. While these two choices did not cover all possible configurations, the particular preparation of the tip (*vide supra*) certainly reduced the possibilities. The clean Pb(111) surface was represented by an embedded three-layer cluster of up to 100 atoms. The calculations revealed that threefold coordinated hollow sites of Pb(111) represent energetically favored adsorption sites for single Pb atoms.

Entire conductance traces were calculated for tips approaching to and retracting from on-top and hollow sites of the pristine Pb(111) lattice [Figs. 6.3(a), (e)]. Additionally, conductance traces for single Pb adatoms [Figs. 6.3(b), (f)] were simulated. The orientation of the tip structure with respect to the Pb(111) lattice is indicated for the single-atom [Figs. 6.3(c), (d)] and the four-atom [Figs. 6.3(g), (h)] terminated tip. The resulting contact conductances and hysteresis widths are summarized in Table 6.1. In the calculations contact formation ( $\Delta z = 0$  pm) was defined by a conductance increase exceeding  $0.3 G_0$  between two subsequent tip displacements. An additional requirement was the variation of the conductance by less than  $0.3 G_0$  for two subsequent displacements in the contact range ( $\Delta z > 0$  pm). According to this definition the single-atom terminated Pb tip exhibited calculated contact conductances of  $G_c = 0.7 G_0$  and  $G_c = 0.9 G_0$  for on-top and hollow sites on Pb(111), respectively [Fig. 6.3(a)]. The geometry of such low-conductance junctions is depicted in Fig. 6.3(i) for the on-top configuration at displacement  $\Delta z = 0$  pm. Distortions of the tip and the substrate were still elastic at this displacement. In particular, the tip apex atom was centered atop the approached Pb(111) atom. The calculations unveiled that the geometry of these low-conductance junctions was unstable. Indeed, the sim-

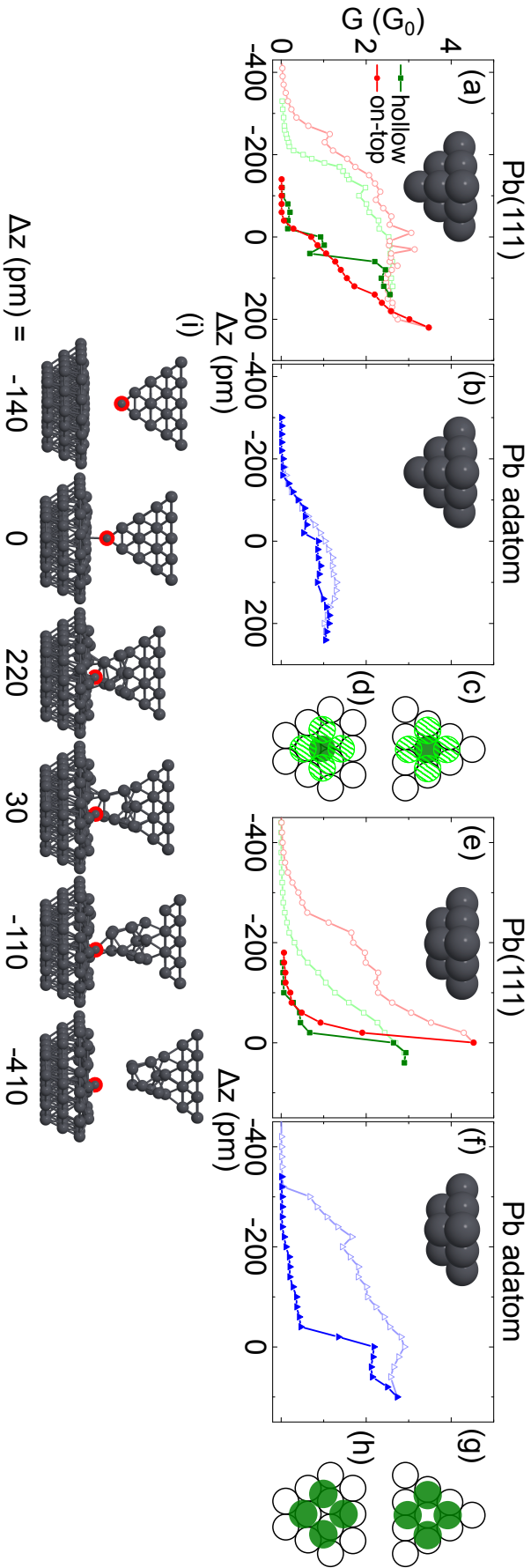


Figure 6.3: Calculations of conductance-distance characteristics during forming and breaking of Pb contacts. (a) A single-atom terminated tip approaches (filled symbols) to and retracts (open symbols) from on-top (squares) and hollow (circles) Pb(111) lattice sites. (b) Same as (a) for a single Pb adatom (triangles). (c), (d) Position of single-atom terminated tip (filled and hatched circles for apex atom and second-layer atoms, respectively) relative to the Pb(111) lattice (circles) for contacts comprising the on-top (c) and the hollow (d) site. (e), (f) Like (a), (b) for a four-atom terminated tip. (g), (h) Position of four-atom terminated tip (filled circles) relative to the Pb(111) lattice (circles) for contacts comprising the on-top (g) and hollow (h) site. (i) Snapshots of calculated contact geometries for a single-atom terminated tip approaching an on-top site of pristine Pb(111). Increasing (decreasing) displacements ( $\Delta z$ ) correspond to tip approach (retraction). Upon retraction the tip apex atom (encircled by a full red line) is transferred to a Pb(111) hollow site adjacent to the approached on-top site.

Table 6.1: Calculated contact conductances ( $G_c$ ) and hysteresis widths ( $H$ ) of atom-sized Pb junctions. Pb tips grown in the  $\langle 100 \rangle$  ( $\langle 111 \rangle$ ) have apices terminated by 1 and 4 (1 and 3) atoms. On pristine Pb(111) contacts are formed at on-top and hollow sites. The contacted single Pb adatom resides at a Pb(111) hollow site.

orientation & apex atoms		$G_c$ ( $G_0$ )			$H$ (pm)		
		on-top	hollow	adatom	on-top	hollow	adatom
$\langle 100 \rangle$	1	0.7	0.9	0.9	270	180	40
	4	2.2	4.5	2.2	200	140	260
$\langle 111 \rangle$	1	1.1	2.4	1.5	380	80	100
	3	(3)	2	2.5	(400)	150	550

ulations revealed that these junctions exhibited the propensity for atomic relaxations upon further tip approach. Approaching the single-atom terminated tip towards the Pb(111) on-top (hollow) site by 140 pm (60 pm) led to a strong increase of the junction conductance, rather than to a plateau-like variation. The calculated junction geometry showed the implantation of the tip apex atom into the surface [Fig. 6.3(i),  $\Delta z = 220$  pm], which caused the conductance increase.

Forming and breaking of contacts comprising a single-atom terminated tip and the pristine Pb(111) surface revealed hysteretic behavior [Fig. 6.3(a)]. The hysteresis widths were extracted from calculated conductance traces according to the procedure exposed in Fig. 6.1(a). For single-atom terminated tips hysteresis widths of 270 pm and 180 pm were obtained for on-top and hollow sites, respectively (Table 6.1). Figure 6.3(i) further shows that single-atom terminated tips transfer their apex atom to the bare Pb(111) surface upon contact, in agreement with the experimental observation. Upon approaching a Pb(111) on-top site the tip apex atom was transferred to an adjacent hollow site upon contact, reflecting the preferred adsorption site of a single Pb atom.

Junctions comprising an atomically sharp tip and a single Pb adatom showed conductance-displacement characteristics depicted in Fig. 6.3(b). In contrast to the simulation of contacts comprising the pristine Pb(111) surface a nearly gradual evolution of the conductance in transition range between tunneling and contact was observed, rather than an abrupt jump. The contact conductance was  $\approx 0.9 G_0$  and thus appreciably lower than the averaged experimental value. Only a few number of contacts were experimentally observed with a similarly low conductance [Fig. 6.2(b)]. In addition, a conductance hysteresis was virtually absent for the simulated contacts to adatoms.

The broad range of contact conductances observed in the experiments, i. e.,  $\approx 1.0 G_0$  to  $\approx 5.0 G_0$  for Pb(111) and  $\approx 1.5 G_0$  to  $\approx 3 G_0$  for Pb adatoms, could not be explained by tip apices terminated by a single atom alone. According to Table 6.1 calculated contact conductances comprising single-atom terminated tips and on-top and hollow sites of Pb(111) are  $0.7 G_0$  and  $0.9 G_0$ , respectively, while contacts to a single Pb adatom exhibit a conductance of  $0.9 G_0$ . These deviations to experimental observations represented the impetus to likewise consider junctions comprising tips terminated by 4 Pb atoms in the simulations.

Representative conductance-displacement characteristics are displayed in Fig. 6.3(e) for contacts at on-top and hollow Pb(111) sites and in Fig. 6.3(f) for single Pb adatoms residing at Pb(111) hollow sites. In agreement with the experiment abrupt changes of tunneling to contact conductances and jumps out of contact occurred in the calculations. The calculated contact conductance for on-top and hollow Pb(111) sites was  $2.2 G_0$  and  $4.5 G_0$ , respectively.<sup>2</sup> Contacts comprising a four-atom terminated tip and a single Pb adatom exhibited a conductance of  $2.2 G_0$ . The calculated hysteresis widths were 200 pm and 140 pm for on-top and hollow sites of Pb(111), respectively, and 260 pm for the Pb adatom. The simulated hysteresis width for the adatom junction exceeds the experimentally most frequently observed widths between 0 and 50 pm [Fig. 6.2(d)]. Only a few junctions exhibited widths in the range of 200 – 450 pm, which are compatible with the calculated result. For the other ideal contact geometry considered in the calculations, *i. e.*, a single-atom terminated tip and the adatom, an essentially vanishing  $H$  was obtained [Fig. 6.3(b)]. Therefore, the experimental junction most likely adopts a geometry within the range of these two extreme and ideal cases. Unlike the simulations based on a single-atom terminated tip, the approach of a four-atom terminated tip to a single Pb adatom on Pb(111) [Fig. 6.3(f)] showed – in accordance with the experiment – an abrupt jump to and out of contact. Therefore, considering both single-atom and four-atom terminated tips in the simulations led to an improved description of the broad conductance distribution observed in the experiments. Furthermore, the conductance hysteresis observed from closing and opening of the junctions was well reproduced.

Similar calculations were performed for Pb tips grown along the  $\langle 111 \rangle$  direction (Table 6.1).

## 6.5 CONCLUSIONS

Closing tunneling junctions comprising Pb tips of an STM and Pb(111) surfaces occurred via an abrupt jump to the first ballistic conductance plateau. Upon opening such junctions a pronounced hysteretic conductance behavior was observed. In contrast to previously studied Au junctions the Pb conductance hysteresis was not solely due to elastic distortions of the electrodes. Rather, it reflected the plasticity of Pb constrictions even at the ultimate size limit. Additionally, to comprehensively describe electron transport through the biased Pb contacts and mechanical relaxations of the junctions simulations had to deviate from the commonly assumed simple pyramidal tip structure and include more complex tip apices that were terminated by more than a single atom. The presented findings therefore highlight that low-conductance junctions do not necessarily reflect simple junction geometries. Moreover, the results are relevant to mechanical deformations at the nanometer scale.

<sup>2</sup> Calculations revealed that contacts comprising a four-atom terminated tip apex and on-top sites of Pb(111) involved many atoms in the contact range. In particular, decreasing the tip–surface distance led to an increase of the conductance without reaching a plateau-like conductance variation. Therefore, for this specific junction geometry contact was defined at the same displacement  $\Delta z$  at which contact was reached for junctions comprising four-atom terminated tips and Pb(111) hollow sites.

Part III

APPENDIX

## NOTATION FOR THE POSITION-SPIN REPRESENTATION

---

For the sake of simplicity, throughout this book, we use the simplified position-spin representation explained below. We consider the ultra-simplified notation  $1$  for the particle with associated position  $\mathbf{r}_1$ , spin  $\sigma_1$  and time  $z_1$  (on the contour) or  $t_1$  (if real) to be:

$$1 = (\mathbf{x}_1, z_1) = (\mathbf{r}_1 \sigma_1, z_1) \quad (\text{A.1})$$

where we have implicitly defined the position-spin coordinate  $\mathbf{x}_1$ . Following this definitions, for example, the two-particle Green's function for the interaction of particles 1 and 2 can be written with the next entries:

$$\begin{aligned} G_2(1, 2; 1', 2') &= G_2(\mathbf{x}_1, z_1, \mathbf{x}_2, z_2; \mathbf{x}'_1, z'_1, \mathbf{x}'_2, z'_2) \\ &= G_2(\mathbf{r}_1 \sigma_1, z_1, \mathbf{r}_2 \sigma_2, z_2; \mathbf{r}'_1 \sigma'_1, z'_1, \mathbf{r}'_2 \sigma'_2, z'_2) \end{aligned} \quad (\text{A.2})$$

The last term reveals how necessary this trick is to simplify the notation and the equations.

The definition of the simplified notations mixing positions and spin components forces us to use also a tricky, simplified notation for integrals in space and sums in the spin component defined by the next chain of equivalences:

$$\int d1 \equiv \int d\mathbf{x}_1 \equiv \sum_{\sigma_1} \int d\mathbf{r}_1 \quad (\text{A.3})$$

and also if we take limits on (real/contour)-time without touching the rest of coordinates:

$$1^+ \equiv \lim_{z_1 \rightarrow z_1^+} (\mathbf{x}_1, z_1) \equiv \lim_{z_1 \rightarrow z_1^+} (\mathbf{r}_1 \sigma_1, z_1) \quad (\text{A.4})$$

or if we act with the  $\delta$ -function:

$$\delta(\mathbf{x}_1 - \mathbf{x}_2) = \delta_{\sigma_1 \sigma_2} \delta(\mathbf{r}_1 - \mathbf{r}_2) \quad (\text{A.5})$$

## TIME EVOLUTION

---

The time evolution of a system governed by the Time-dependent Schrödinger equation:

$$\boxed{i \frac{d}{dt} |\Psi(t)\rangle = \hat{H}(t) |\Psi(t)\rangle} \quad (\text{B.1})$$

$|\Psi(t)\rangle$  is uniquely determined once the initial ket  $|\Psi(t_0)\rangle$  is given. For time-independent Hamiltonians  $\hat{H}(t) = \hat{H}(t_0)$  for all times  $t$  and ((B.1)) is solved by

$$|\Psi(t)\rangle = e^{-i\hat{H}(t_0)(t-t_0)} |\Psi(t_0)\rangle \quad (\text{B.2})$$

If  $\hat{H}(t)$  is time-dependent, we need the evolution operator  $\hat{U}(t, t_0)$  which converts  $|\Psi(t_0)\rangle$  into  $|\Psi(t)\rangle$ :

$$|\Psi(t)\rangle = \hat{U}(t, t_0) |\Psi(t_0)\rangle \quad (\text{B.3})$$

Now we introduce the *time* and *anti-time ordering operators*  $T$  and  $\bar{T}$ . The action of the former is to sort the operators in chronological order with that of the later time to the right, while the later, as its counterpart, does the opposite. The *time-evolution operator* results in:

$$\hat{U}(t, t_0) = \begin{cases} T \left\{ e^{-i \int_{t_0}^t d\bar{t} \hat{H}(\bar{t})} \right\} & t > t_0 \\ \bar{T} \left\{ e^{+i \int_t^{t_0} d\bar{t} \hat{H}(\bar{t})} \right\} & t < t_0 \end{cases} \quad (\text{B.4})$$

In the Heisenberg picture, operators instead of wavefunctions evolve in time, so that the evolution of a Heisenberg picture operator  $\hat{O}_H(t)$  looks, in terms of its corresponding Schrödinger picture  $\hat{O}(t)$  and the *time-evolution operator*:

$$\boxed{\hat{O}_H(t) \equiv \hat{U}(t_0, t) \hat{O}(t) \hat{U}(t, t_0)} \quad (\text{B.5})$$

which we apply not only to observable operators, but also to field operators. To show that it is legitimate, we take the density operator  $\hat{n}(\mathbf{x}) = \hat{\psi}^\dagger(\mathbf{x}) \hat{\psi}(\mathbf{x})$  which is

associated with an observable quantity and is written in terms of two field operators which also admit a Heisenberg picture

$$\begin{aligned}\hat{n}_H(\mathbf{x}) &= \hat{U}(t_0, t) \hat{n}(\mathbf{x}) \hat{U}(t, t_0) = \hat{U}(t_0, t) \hat{\psi}^\dagger(\mathbf{x}) \hat{\psi}(\mathbf{x}) \hat{U}(t, t_0) \\ &= \hat{U}(t_0, t) \hat{\psi}^\dagger(\mathbf{x}) \underbrace{\hat{U}(t, t_0) \hat{U}(t_0, t)}_{\hat{1}} \hat{\psi}(\mathbf{x}) \hat{U}(t, t_0) = \hat{\psi}_H^\dagger(\mathbf{x}, t) \hat{\psi}_H(\mathbf{x}, t)\end{aligned}\quad (\text{B.6})$$

which respects the form given by the Schrödinger picture definition of the density operator, so that the Heisenberg picture of the product of two operators  $\hat{O} = \hat{O}_1 \hat{O}_2$  is simply the product of the two operators in the Heisenberg picture  $\hat{O}_H(t) = \hat{O}_{1,H}(t) \hat{O}_{2,H}(t)$ . As a consequence, operators in the Heisenberg picture at equal times satisfy the same (anti)commutation relations as the original operators.

For the non-observable field operators:

$$\left[ \hat{\psi}_H^\dagger(\mathbf{x}, t), \hat{\psi}_H(\mathbf{x}', t) \right]_{\mp} = \delta(\mathbf{x} - \mathbf{x}')$$

## B.1 EQUATIONS OF MOTION FOR OPERATORS IN THE HEISENBERG PICTURE

The equation of motion for operators in the Heisenberg picture:

$$i \frac{d}{dt} \hat{O}_H(t) = \left[ \hat{O}_H(t), \hat{H}_H(t) \right]_{-} + i \frac{\partial}{\partial t} \hat{O}_H(t)\quad (\text{B.7})$$

Because field operators  $\hat{\psi}(\mathbf{x})$ ,  $\hat{\psi}^\dagger(\mathbf{x})$  are the basis to build any operator in second quantization, the equations of motion for  $\hat{\psi}_H(\mathbf{x}, t)$  and  $\hat{\psi}_H^\dagger(\mathbf{x}, t)$  play a crucial role. Let us consider the many-body Hamiltonian 1.4 with some time-dependent one-body part  $\hat{h}(t)$

$$\begin{aligned}\hat{H}_H(t) &= \underbrace{\sum_{\sigma\sigma'} \int d\mathbf{r} \hat{\psi}^\dagger(\mathbf{r}\sigma, t) h_{\sigma\sigma'}(\mathbf{r}, -i\nabla, \mathbf{S}, t) \hat{\psi}(\mathbf{r}\sigma', t)}_{\hat{H}_0(t)} \\ &\quad + \frac{1}{2} \int d\mathbf{x} d\mathbf{x}' v(\mathbf{x}, \mathbf{x}') \hat{\psi}^\dagger(\mathbf{x}) \hat{\psi}^\dagger(\mathbf{x}') \hat{\psi}(\mathbf{x}') \hat{\psi}(\mathbf{x})\end{aligned}\quad (\text{B.8})$$

After some algebra, the equation of motion for the non-observable field annihilation operator  $\hat{\psi}_H(t)$  reads:

$$\boxed{i \frac{d}{dt} \hat{\psi}_H(t) = \sum_{\sigma'} h_{\sigma\sigma'}(\mathbf{r}, -i\nabla, \mathbf{S}, t) \hat{\psi}_H(\mathbf{r}\sigma', t) + \int d\mathbf{x}' v(\mathbf{x}, \mathbf{x}') \hat{n}_H(\mathbf{x}', t) \hat{\psi}_H(t)}$$

(B.9)

And the adjoint equation for the creation operator  $\hat{\psi}_H^\dagger(t)$ :

$$i \frac{d}{dt} \hat{\psi}_H^\dagger(t) = - \sum_{\sigma'} \hat{\psi}_H^\dagger(\mathbf{r}\sigma', t) h_{\sigma\sigma'}(\mathbf{r}, i\overleftarrow{\nabla}, \mathbf{S}, t) + \int d\mathbf{x}' v(\mathbf{x}, \mathbf{x}') \hat{\psi}_H^\dagger(t) \hat{n}_H(\mathbf{x}', t)$$

(B.10)

## TIME-DEPENDENT QUANTUM AND ENSEMBLE AVERAGES.

### C.1 TIME-DEPENDENT QUANTUM AVERAGES: THE KELDYSH CONTOUR

The time-dependent quantum average of an operator  $\hat{O}(t)$  at time  $t$  when the system is prepared in the state  $|\Psi(t_0)\rangle \equiv |\Psi_0\rangle$  at time  $t_0$  is, by performing the average of equation (B.5) with  $|\Psi(t)\rangle$ :

$$\begin{aligned} O(t) &= \overbrace{\langle \Psi(t) | \hat{O}(t) | \Psi(t) \rangle}^{\text{Schrödinger picture}} \equiv \overbrace{\langle \Psi_0 | \hat{O}_H(t) | \Psi_0 \rangle}^{\text{Heisenberg picture}} \\ &= \langle \Psi_0 | \hat{U}(t_0, t) \hat{O}(t) \hat{U}(t, t_0) | \Psi_0 \rangle \end{aligned} \quad (\text{C.1})$$

with  $\hat{U}(t_0, t)$  the evolution operator defined in (B.4). With this definition of  $\hat{U}(t_0, t)$  and  $\hat{U}(t, t_0)$ , we get:

$$O(t) = \langle \Psi_0 | \underbrace{\bar{T} \left\{ e^{+i \int_{t_0}^t d\bar{t} \hat{H}(\bar{t})} \right\}}_{\hat{U}(t_0, t) \ t_0 < t} \hat{O}(t) \underbrace{T \left\{ e^{-i \int_{t_0}^t d\bar{t} \hat{H}(\bar{t})} \right\}}_{\hat{U}(t, t_0) \ t_0 < t} | \Psi_0 \rangle \quad (\text{C.2})$$

As can be checked in the literature (for example (Stefanucci & Van Leeuwen, 2010)), when expanding the exponentials in (C.2) in powers of the Hamiltonian, the terms of the expansion are composed by integrals of operators like (Stefanucci & Van Leeuwen, 2010)

$$\bar{T} \left\{ \hat{H}(\bar{t}_1) \dots \hat{H}(\bar{t}_n) \right\} \hat{O}(t) T \left\{ \hat{H}(t'_1) \dots \hat{H}(t'_m) \right\} \quad (\text{C.3})$$

where all  $t_i$  and  $t'_i$  have values between  $t_0$  and  $t$ . Introducing the next tricks, these terms can be written in a more convenient form. First, we define the oriented "contour":

$$\gamma \equiv \underbrace{(t_0, t)}_{\gamma_-} \oplus \underbrace{(t, t_0)}_{\gamma_+} \quad (\text{C.4})$$

which travels the path  $t_0 \rightarrow t \rightarrow t_0$ . The contour  $\gamma$  is composed by two paths: the right-travelling branch  $\gamma_-$  and the left-travelling branch  $\gamma_+$ . With this definition of  $\gamma$ , we introduce operators evaluated on time-arguments on the contour as:

$$\hat{O}(z') \equiv \begin{cases} \hat{O}_-(t') & z' = t'_- \\ \hat{O}_+(t') & z' = t'_+ \end{cases} \quad (\text{C.5})$$

In general  $\hat{O}_+(t') \neq \hat{O}_-(t')$ . By defining a contour ordering operator for the product of operators on the contour, say  $\mathcal{T}$ , which puts the "latest" operators on the left, for every permutation  $P$  of the times  $z_m$  later than  $z_{m-1}$ ... later than  $z_1$  we have

$$\mathcal{T} \left\{ \hat{O}_m(z_{P(m)}) \hat{O}_{m-1}(z_{P(m-1)}) \dots \hat{O}_1(z_{P(1)}) \right\} = \hat{O}_m(z_m) \hat{O}_{m-1}(z_{m-1}) \dots \hat{O}_1(z_1) \quad (\text{C.6})$$

Any point on the left-travelling branch is always later than a point on the right-travelling branch.

The contour ordering operator can be used to rewrite (C.3) in a compact form. By writing the Hamiltonian  $\hat{H}$  and the operator  $\hat{O}$  on  $\gamma$ , taking into account that both  $\hat{H}$  and  $\hat{O}$  are the same on the left- and right-travelling branches, and the same as evaluated on the real-time axis:

$$\hat{H}(z' = t'_\pm) \equiv \hat{H}(t') \quad \hat{O}(z' = t'_\pm) \equiv \hat{O}(t') \quad (\text{C.7})$$

Actually, all operators associated with observable quantities (like the density, current, energy, etc.), with argument on the contour are defined as in (C.7), in particular the field operators:

$$\boxed{\hat{\psi}(\mathbf{x}, z' = t'_\pm) \equiv \hat{\psi}(\mathbf{x}, t') \quad \hat{\psi}^\dagger(\mathbf{x}, z' = t'_\pm) \equiv \hat{\psi}^\dagger(\mathbf{x}, t')} \quad (\text{C.8})$$

Using (C.7) we can rewrite (C.3) using a single contour ordered instead of two time-ordered operator product chains as:

$$\mathcal{T} \left\{ \hat{H}(t_{1+}) \dots \hat{H}(t_{n+}) \hat{O}(t_\pm) \hat{H}(t'_{1-}) \dots \hat{H}(t'_{m-}) \right\} \quad (\text{C.9})$$

The contour integral between two points  $z_1$  and  $z_2$  on  $\gamma$  works the same way as the standard integral along any contour. If  $z_1$  is earlier than  $z_2$

$$\int_{z_1}^{z_2} d\bar{z} \hat{O}(\bar{z}) = \begin{cases} \int_{t_1}^{t_2} d\bar{z} \hat{O}_-(\bar{z}) & \text{if } z_1 = t_{1-} \text{ and } z_2 = t_{2-} \\ \int_{t_1}^{t_2} d\bar{z} \hat{O}_-(\bar{z}) + \int_t^{t_2} d\bar{z} \hat{O}_+(\bar{z}) & \text{if } z_1 = t_{1-} \text{ and } z_2 = t_{2+} \\ \int_{t_1}^{t_2} d\bar{z} \hat{O}_+(\bar{z}) & \text{if } z_1 = t_{1+} \text{ and } z_2 = t_{2+} \end{cases} \quad (\text{C.10})$$

while if  $z_1$  is later than  $z_2$ , the sign is the opposite:

$$\int_{z_1}^{z_2} d\bar{z} \hat{O}(\bar{z}) = - \int_{z_2}^{z_1} d\bar{z} \hat{O}(\bar{z}) \quad (\text{C.11})$$

Doing this for every term (C.3) of the expansion of the exponentials in (C.2) the time-dependent quantum average (which coincides for both the Schrödinger and the Heisenberg pictures) of the later is rewritten as:

$$O(t) = \langle \Psi_0 | \mathcal{T} \left\{ \underbrace{e^{-i \int_{\gamma_+} d\bar{z} \hat{H}(\bar{z})}}_{- \int_{\gamma_+} \equiv - \int_{t_+^{t_0+}} \equiv \int_{t_0}^t} \hat{O}(t_{\pm}) \underbrace{e^{-i \int_{\gamma_-} d\bar{z} \hat{H}(\bar{z})}}_{\int_{\gamma_-} \equiv \int_{t_{0-}^{t_0-}} \equiv \int_{t_0}^t} \right\} | \Psi_0 \rangle$$

Because products of operators under the  $\mathcal{T}$  action can be reordered without changing the result, as if these were commuting ones (the same happens for the time and anti-time ordering operators), this can be simplified as:

$$O(t) = \langle \Psi_0 | \mathcal{T} \left\{ e^{-i \int_{\gamma} d\bar{z} \hat{H}(\bar{z})} \hat{O}(t_{\pm}) \right\} | \Psi_0 \rangle \quad (\text{C.12})$$

where  $\int_{\gamma} \equiv \int_{\gamma_-} + \int_{\gamma_+}$  travels through  $t_{0-} \rightarrow t_- \rightarrow t_+ \rightarrow t_{0+}$ .

If we extend  $\gamma$  up to infinity, the contour ordered product in (C.12) is evaluated, with  $\gamma$  the extended contour, when the operator  $\hat{O}$  is placed in the position  $t_{\pm}$

$$\mathcal{T} \left\{ e^{-i \int_{\gamma} d\bar{z} \hat{H}(\bar{z})} \hat{O}(t_-) \right\} = \hat{U}(t_0, \infty) \hat{U}(\infty, t) \hat{O}(t) \hat{U}(t, t_0) = \hat{U}(t_0, t) \hat{O}(t) \hat{U}(t, t_0)$$

and

$$\mathcal{T} \left\{ e^{-i \int_{\gamma} d\bar{z} \hat{H}(\bar{z})} \hat{O}(t_+) \right\} = \hat{U}(t_0, t) \hat{O}(t) \hat{U}(t, \infty) \hat{U}(\infty, t_0) = \hat{U}(t_0, t) \hat{O}(t) \hat{U}(t, t_0)$$

So that expanding the contour until  $\infty$  in time does not change the expectation value. This infinitely extended contour is referred as the *Keldysh or Schwinger-Keldysh contour* (Stefanucci and Van Leeuwen (Stefanucci & Van Leeuwen, 2010)). The physics does not depend on the contour choice, thus, all the different formulations of the Green's function method must be equivalent.

Taking into account that  $O(t_{\pm}) = O(t_-) = O(t_+) = O(t)$ , equation (C.12) can be rewritten as:

$$O(z) = \langle \Psi_0 | \mathcal{T} \left\{ e^{-i \int_{\gamma} d\bar{z} \hat{H}(\bar{z})} \hat{O}(t_{\pm}) \right\} | \Psi_0 \rangle \quad (\text{C.13})$$

## C.2 TIME-DEPENDENT ENSEMBLE AVERAGES: THE DENSITY MATRIX OPERATOR

In the section before we treated an isolated system in which kets  $|\Psi\rangle$  and  $|\Psi_0\rangle$  designed a pure state. However, such systems rarely exist, these are idealizations. Systems interacting with the environment need to be described by a mixture of many-body pure states. The statistical approach is to assign a probability  $w_n \in [0, 1]$  for the system to be in the state  $|\chi_n\rangle$  in  $t_0$ , with the normalization condition  $\sum_n w_n = 1$ . The kets  $|\chi_n\rangle$  are normalized  $\langle \chi_n | \chi_n \rangle$  but do not need to be orthogonal, because, typically, they have different spectral energies and other quantum numbers, forming a spectral distribution given by the spectral function  $\hat{A}(E)$ .

With this definition of the mixed states, the ensemble average of an operator  $\hat{O}(t)$  at time  $t_0$  is defined in the most natural way as:

$$O(t_0) = \sum_n w_n \langle \chi_n | \hat{O}(t_0) | \chi_n \rangle \quad (\text{C.14})$$

with all  $w_n = 0$  except for one in the case of a pure state, when it reduces to the former quantum average. The weighting factor  $w_n$  introduces the interaction between the system and the environment.

The ensemble average is characterized by a quantity which is extremely useful, the density matrix operator  $\hat{\rho}$ , described by the states forming the mixture as:

$$\hat{\rho} = \sum_n w_n |\chi_n\rangle\langle\chi_n| \quad (\text{C.15})$$

which is self-adjoint  $\hat{\rho} = \hat{\rho}^\dagger$  and positive-semidefinite since:

$$\langle \Psi | \hat{\rho} | \Psi \rangle = \sum_n w_n |\langle \Psi | \chi_n \rangle|^2 \geq 0$$

for any state  $|\Psi\rangle$ . If we construct a generic basis of orthonormal states denoted by  $|\Psi_k\rangle$ , the ensemble average based on  $\hat{\rho}$  is:

$$\begin{aligned} O(t_0) &= \sum_k \sum_n w_n \langle \chi_n | \Psi_k \rangle \langle \Psi_k | \hat{O}(t_0) | \chi_n \rangle = \sum_k \langle \Psi_k | \hat{O}(t_0) \hat{\rho} | \Psi_k \rangle \\ &= Tr[\hat{O}(t_0) \hat{\rho}] = Tr[\hat{\rho} \hat{O}(t_0)] \end{aligned} \quad (\text{C.16})$$

where  $Tr$  represents the Trace in the Fock space  $\mathcal{F}$ . Every  $|\chi_n\rangle$  is normalized and  $\sum_n w_n = 1$ , so that  $Tr[\hat{\rho}] = 1$ .

If we choose the family of kets  $|\Psi_k\rangle$  to be the eigenstates of  $\hat{\rho}$  with positive eigenvalues  $\rho_k$  summing up to 1, which leads to  $\rho_k \in [0, 1]$  and  $Tr[\hat{\rho}^2] \leq 1$ , the density matrix operator can be expanded by its eigenstates as  $\sum_k \rho_k |\Psi_k\rangle\langle\Psi_k|$ . The  $\rho_k$  are defined as:

$$\rho_k = \frac{e^{-\beta E_k^M}}{\sum_p e^{-\beta E_p^M}}$$

where  $E_k^M$  is the energy eigenvalue of ket  $\Psi_k$  from the so called Matsubara Hamiltonian  $\hat{H}^M$ , which describe the system in the initial preparation, and  $\beta$  is the inverse

temperature  $\beta = \frac{1}{k_B T}$  where  $k_B$  is the Boltzmann constant. We can write the Matsubara Hamiltonian:

$$\hat{H}^M = \sum_k E_k^M |\Psi_k\rangle\langle\Psi_k| \quad (\text{C.17})$$

and the density operator as:

$$\hat{\rho} = \sum_k \frac{e^{-\beta E_k^M}}{Z} |\Psi_k\rangle\langle\Psi_k| = \frac{e^{-\beta \hat{H}^M}}{Z} \quad (\text{C.18})$$

where  $Z$  is the partition function defines as:

$$Z = \sum_p e^{-\beta E_p^M} = \text{Tr} \left[ e^{-\beta \hat{H}^M} \right] \quad (\text{C.19})$$

Typically the density matrix operator  $\hat{\rho}$  is chosen to describe a system in thermodynamic equilibrium at a given temperature  $T$  and chemical potential  $\mu$ . The Matsubara Hamiltonian from which  $\hat{\rho}$  arises relates the many-body Hamiltonian and the chemical potential of the system as  $\hat{H}^M = \hat{H} - \mu \hat{N}$ .

Following the statistical description of the mixed states explained above, the time-evolution of each system of the ensemble needs to be calculated and then the  $w_n$  weighted sum of the time-dependent single-state quantum averages  $\langle \chi_n(t) | \hat{O}(t) | \chi_n(t) \rangle$ . Because the Hamiltonian  $\hat{H}(z)$  is common for all the single many-body kets  $|\chi_n(t)\rangle$ , the time-evolution is also common:

$$\begin{aligned} O(z) &= \sum_n \langle \chi_n(t) | \hat{U}(t_0, t) \hat{O}(t) \hat{U}(t, t_0) | \chi_n(t) \rangle = \text{Tr} \left[ \hat{\rho} \hat{U}(t_0, t) \hat{O}(t) \hat{U}(t, t_0) \right] \\ &= \text{Tr} \left[ \hat{\rho} \mathcal{T} \left\{ e^{-i \int_{\gamma} d\bar{z} \hat{H}(\bar{z})} \hat{O}(z) \right\} \right] \end{aligned} \quad (\text{C.20})$$

with the representation of the density matrix operator in (C.18)

$$O(z) = \frac{\text{Tr} \left[ e^{-\beta \hat{H}^M} \mathcal{T} \left\{ e^{-i \int_{\gamma} d\bar{z} \hat{H}(\bar{z})} \hat{O}(z) \right\} \right]}{\text{Tr} \left[ e^{-\beta \hat{H}^M} \right]} \quad (\text{C.21})$$

By inspection of the equations, as seen in (Stefanucci and Van Leeuwen (Stefanucci & Van Leeuwen, 2010)), two remarkable issues arise:

1. The contour ordered product equals the identity and, thus, can be inserted anywhere, particularly inside the trace in the denominator of (C.21)

$$\mathcal{T} \left\{ e^{-i \int_{\gamma} d\bar{z} \hat{H}(\bar{z})} \hat{O}(z) \right\} = \hat{U}(t_0, \infty) \hat{U}(\infty, t_0) = \hat{1} \quad (\text{C.22})$$

2. There is a trick to write the exponential of  $\hat{H}^M$  as an integral along a vertical path in the complex plane related to the inverse temperature  $\beta$ :

$$e^{-\beta \hat{H}^M} = e^{-i \int_{\gamma^M} d\bar{z} \hat{H}^M(\bar{z})} \quad (\text{C.23})$$

the path  $\gamma^M$  being any contour travelling from  $z_a$  to  $z_b$  fulfilling:

$$\boxed{z_b - z_a = -i\beta}$$

From 1 and 2:

$$O(z) = \frac{\text{Tr} \left[ e^{-i \int_{\gamma^M} d\bar{z} \hat{H}^M(\bar{z})} \mathcal{T} \left\{ e^{-i \int_{\gamma} d\bar{z} \hat{H}(\bar{z})} \hat{O}(z) \right\} \right]}{\text{Tr} \left[ e^{-i \int_{\gamma^M} d\bar{z} \hat{H}^M(\bar{z})} \mathcal{T} \left\{ e^{-i \int_{\gamma} d\bar{z} \hat{H}(\bar{z})} \right\} \right]} \quad (\text{C.24})$$

Which, after redefining  $\gamma$  as  $\gamma = \gamma_- \oplus \gamma_+ \oplus \gamma^M$ , can be reduced, due to the cyclic property of the trace (see (Stefanucci & Van Leeuwen, 2010)), to:

$$\boxed{O(z) = \frac{\text{Tr} \left[ \mathcal{T} \left\{ e^{-i \int_{\gamma} d\bar{z} \hat{H}(\bar{z})} \hat{O}(z) \right\} \right]}{\text{Tr} \left[ \mathcal{T} \left\{ e^{-i \int_{\gamma} d\bar{z} \hat{H}(\bar{z})} \right\} \right]}} \quad (\text{C.25})$$

## EQUATIONS OF MOTION OF THE GREEN'S FUNCTION ON THE CONTOUR

---

### D.1 EQUATIONS OF MOTION ON THE CONTOUR

Moving the equations of motion of the creation (B.9) and annihilation (B.10) operators to the contour, by doing:

$$\langle \mathbf{x} | \hat{h} | \mathbf{x} \rangle = h_{\sigma\sigma'}(\mathbf{r}, -i\nabla, \mathbf{S}, z) \delta(\mathbf{r} - \mathbf{r}') = \delta(\mathbf{r} - \mathbf{r}') h_{\sigma\sigma'}(\mathbf{r}', i\overleftarrow{\nabla}', \mathbf{S}, z)$$

the equation of motion for the non-observable field annihilation operator  $\hat{\psi}_H(z)$  reads:

$$\boxed{i \frac{d}{dz} \hat{\psi}_H(z) = \int d\mathbf{x}' \langle \mathbf{x} | \hat{h}(z) | \mathbf{x} \rangle \hat{\psi}_H(\mathbf{x}', z) + \int d\mathbf{x}' v(\mathbf{x}, \mathbf{x}', z) \hat{n}_H(\mathbf{x}', z) \hat{\psi}_H(z)}$$

(D.1)

and the adjoint equation for the creation operator  $\hat{\psi}_H^\dagger(z)$ :

$$\boxed{-i \frac{d}{dz} \hat{\psi}_H^\dagger(z) = \int d\mathbf{x}' \hat{\psi}_H^\dagger(\mathbf{x}', z) \langle \mathbf{x} | \hat{h}(z) | \mathbf{x} \rangle + \int d\mathbf{x}' v(\mathbf{x}, \mathbf{x}', z) \hat{\psi}_H^\dagger(z) \hat{n}_H(\mathbf{x}', z)}$$

(D.2)

### D.2 OPERATOR CORRELATORS ON THE CONTOUR

The operator correlators are strings of operators with the following structure:

$$\hat{k}(z_1, \dots, z_n) = \mathcal{T} \left\{ \hat{O}_1(z_1) \dots \hat{O}_n(z_n) \right\} \quad (D.3)$$

The best way to derive relations for the operator correlators is to differentiate them with respect to their contour arguments. The most simple operator correlator is the contour ordered product of two operators (abbreviating the notation  $\hat{O}_j(z_j) \equiv \hat{O}_j$ ):

The operator correlators are strings of operators with the following structure:

$$\mathcal{T} \left\{ \hat{O}_1 \hat{O}_2 \right\} = \theta(z_1, z_2) \hat{O}_1 \hat{O}_2 + \theta(z_2, z_1) \hat{O}_2 \hat{O}_1 \quad (D.4)$$

Differentiating with respect to  $z_1$ :

$$\frac{d}{dz_1} \mathcal{T} \{ \hat{O}_1 \hat{O}_2 \} = \delta(z_1, z_2) \left[ \hat{O}_1, \hat{O}_2 \right]_{\mp} + \mathcal{T} \left\{ \left( \frac{d}{dz_1} \hat{O}_1 \right) \hat{O}_2 \right\} \quad (\text{D.5})$$

where the upper/lower  $\mp$  sign stands for bosonic/fermionic operators, so that fermions use the anti-commutator.

The generalization of (D.5) for correlators of  $n$  operators is:

$$\frac{d}{dz_k} \mathcal{T} \{ \hat{O}_1 \dots \hat{O}_n \} = \delta_{z_k}^{\theta} \mathcal{T} \{ \hat{O}_1 \dots \hat{O}_n \} + \mathcal{T} \left\{ \hat{O}_1 \dots \hat{O}_{k-1} \left( \frac{d}{dz_k} \hat{O}_k \right) \hat{O}_{k+1} \dots \hat{O}_n \right\} \quad (\text{D.6})$$

and defining

$$\partial_{z_k}^{\theta} \mathcal{T} \{ \hat{O}_1 \dots \hat{O}_n \} = \sum_P (\pm)^P \left( \frac{d}{dz_k} \theta_n(z_{P(1)}, \dots, z_{P(n)}) \right) \hat{O}_{P(1)} \dots \hat{O}_{P(n)} \quad (\text{D.7})$$

where:

$$\begin{aligned} & \partial_{z_k}^{\theta} \mathcal{T} \{ \hat{O}_1 \dots \hat{O}_n \} \\ &= \sum_{l=1}^{k-1} (\pm)^{k-l} \delta(z_k, z_l) \mathcal{T} \left\{ \hat{O}_1 \dots \hat{O}_{l-1} \hat{O}_{l+1} \dots \left[ \hat{O}_k, \hat{O}_l \right]_{\mp} \hat{O}_{k+1} \dots \hat{O}_n \right\} \\ &+ \sum_{l=k+1}^n (\pm)^{l-k-1} \delta(z_k, z_l) \mathcal{T} \left\{ \hat{O}_1 \dots \left[ \hat{O}_k, \hat{O}_l \right]_{\mp} \hat{O}_{k+1} \dots \hat{O}_{l-1} \hat{O}_{l+1} \dots \hat{O}_n \right\} \end{aligned} \quad (\text{D.8})$$

In case the operators  $\hat{O}_l$  are the field operators in the contour Heisenberg picture, taking into account that equal-time operators are subject to the (anti)commutation in each term of the sum:

$$\boxed{\begin{aligned} \left[ \hat{\psi}^{\dagger}(\mathbf{x}_k, z), \hat{\psi}^{\dagger}(\mathbf{y}_l, z) \right]_{\mp} &= 0; \\ \left[ \hat{\psi}(\mathbf{x}_k, z), \hat{\psi}(\mathbf{y}_l, z) \right]_{\mp} &= 0; \\ \left[ \hat{\psi}(\mathbf{x}_k, z), \hat{\psi}^{\dagger}(\mathbf{y}_l, z) \right]_{\mp} &= \delta(\mathbf{x}_k - \mathbf{y}_l); \end{aligned}}$$

we propose for the  $\hat{O}_l$ 's:

$$\left[ \hat{O}_k(z), \hat{O}_l(z) \right]_{\mp} = c_{kl}(z) \hat{\mathbb{1}} \quad (\text{D.9})$$

where  $c_{kl}(z)$  is a scalar function of  $z$  and the expression is valid only for the equal-time (anti)commutation. Of course, the identity commutes with all the operators inside the contour-ordering operator and, thus, can be extracted:

$$\begin{aligned}
 & \partial_{z_k}^\theta \mathcal{T} \left\{ \hat{O}_1 \dots \hat{O}_n \right\} \\
 &= \sum_{l=1}^{k-1} (\pm)^{k-l} \delta(z_k, z_l) \left[ \hat{O}_k, \hat{O}_l \right]_{\mp} \mathcal{T} \left\{ \hat{O}_1 \dots \hat{O}_{l-1} \dots \hat{O}_{k+1} \dots \hat{O}_n \right\} \\
 &+ \sum_{l=k+1}^n (\pm)^{l-k-1} \delta(z_k, z_l) \left[ \hat{O}_k, \hat{O}_l \right]_{\mp} \mathcal{T} \left\{ \hat{O}_1 \dots \hat{O}_{k-1} \dots \hat{O}_{l-1} \dots \hat{O}_n \right\}
 \end{aligned} \tag{D.10}$$

The operator correlators  $\hat{k}$  arise from the expansion of the contour-ordered exponential and in the equations of motion. Because of this fact, the  $\hat{O}_k$ 's correspond usually to observable quantities characterized by an equal number of creation and annihilation field operators.

For simplicity, we make the notation more compact:

$$i = \mathbf{x}_i, z_i; \quad j = \mathbf{x}_j, z_j; \quad i' = \mathbf{x}'_i, z'_i; \quad j' = \mathbf{x}'_j, z'_j;$$

and for the arguments of the functions, for example, the  $\delta$ -function:

$$\delta(j; k) = \delta(z_j, z_k) \delta(\mathbf{x}_j - \mathbf{x}_k)$$

by defining a special kind of correlators, the Green's functions, which play the central role in our formalism:

$$\hat{G}_n(1, \dots, n; 1', \dots, n') \equiv \frac{1}{i^n} \mathcal{T} \left\{ \hat{\psi}_H(1) \dots \hat{\psi}_H(n) \hat{\psi}_H^\dagger(n') \dots \hat{\psi}_H^\dagger(1') \right\} \tag{D.11}$$

where the  $j' = x'_j, z'_j$  and  $j = x_j, z_j$  coordinates label creation and annihilation field operators respectively. In case  $n = 0$  we define  $\hat{G}_0 \equiv 1$ . Identifying

$$\hat{O}_j = \begin{cases} \hat{\psi}_H(j) & j = 1, \dots, n \\ \hat{\psi}_H^\dagger((2n - j + 1)') & j = n + 1, \dots, 2n \end{cases}$$

we get

$$\begin{aligned}
 & i \frac{d}{dz_k} \hat{G}_n(1, \dots, n; 1', \dots, n') \\
 &= \frac{1}{i^n} \mathcal{T} \left\{ \hat{\psi}_H(1) \dots \left( i \frac{d}{dz_k} \hat{\psi}_H(k) \right) \dots \hat{\psi}_H(n) \hat{\psi}_H^\dagger(n') \dots \hat{\psi}_H^\dagger(1') \right\} \\
 &+ \sum_{j=1}^n (\pm)^{k+j} \delta(k; j') \hat{G}_{n-1}(1, \dots, \cancel{k}, \dots, n; 1', \dots, \cancel{j'}, \dots, n')
 \end{aligned} \tag{D.12}$$

and

$$\begin{aligned}
 & -i \frac{d}{dz'_k} \hat{G}_n(1, \dots, n; 1', \dots, n') \\
 &= \frac{1}{i^n} \mathcal{T} \left\{ \hat{\psi}_H(1) \dots \hat{\psi}_H(n) \hat{\psi}_H^\dagger(n') \dots \left( -i \frac{d}{dz'_k} \hat{\psi}_H(k') \right) \dots \hat{\psi}_H^\dagger(1') \right\} \quad (\text{D.13}) \\
 &+ \sum_{j=1}^n (\pm)^{k+j} \delta(k; j') \hat{G}_{n-1}(1, \dots, j', \dots, n; 1', \dots, k', \dots, n')
 \end{aligned}$$

Assuming that  $\hat{h}$  does not mix the spin components, being diagonal in spin space

$$\langle \mathbf{x}_1 | \hat{h}(z_1) | \mathbf{x}_2 \rangle = h(1) \delta(\mathbf{x}_1 - \mathbf{x}_2) = \delta(\mathbf{x}_1 - \mathbf{x}_2) h(2) \quad (\text{D.14})$$

rewriting equations (C.24) and (C.25), with the definition  $v(i; j) \equiv \delta(z_i, z_j) v(\mathbf{x}_i, \mathbf{x}_j, z_i)$

$$\boxed{i \frac{d}{dz_k} \hat{\psi}_H(k) = h(k) \hat{\psi}_H(k) + \int d\bar{1} v(k, \bar{1}, z) \hat{n}_H(\bar{1}) \hat{\psi}_H(k)} \quad (\text{D.15})$$

and the adjoint equation for the creation operator  $\hat{\psi}_H^\dagger(z)$ :

$$\boxed{-i \frac{d}{dz'_k} \hat{\psi}_H^\dagger(k') = \hat{\psi}_H^\dagger(k') h(k') + \int d\bar{1} v(k', \bar{1}, z) \hat{\psi}_H(k') \hat{n}_H(\bar{1})} \quad (\text{D.16})$$

Now we want to remove the  $\left( i \frac{d}{dz_k} \hat{\psi}_H(k) \right)$  terms in (D.12) and (D.13). First, we notice that the r.h.s. of (D.15) and (D.16) contains chains of three field operator with the same contour time argument.

$$\hat{n}_H(\bar{1}) \hat{\psi}_H(k) = \hat{\psi}_H^\dagger(\bar{1}) \hat{\psi}_H(\bar{1}) \hat{\psi}_H(k) = \pm \hat{\psi}_H^\dagger(\bar{1}) \hat{\psi}_H(k) \hat{\psi}_H(\bar{1})$$

We want to move the  $\hat{\psi}_H^\dagger(\bar{1})$  to the right to form a  $\hat{G}_n$ , by means of the contour ordering operator  $\mathcal{T}$ . Because we want  $\hat{\psi}_H^\dagger(\bar{1})$  to end up to the left of both  $\hat{\psi}_H(\bar{1})$  and  $\hat{\psi}_H(k)$ , we choose to calculate it infinitesimally after  $\hat{\psi}_H(\bar{1})$ , in  $\bar{1}^+ = \mathbf{x}_1, z_1^+$ , as  $\hat{\psi}_H^\dagger(\bar{1}^+)$ . When being under the action of  $\mathcal{T}$ :

$$\mathcal{T} \left\{ \dots \hat{\psi}_H^\dagger(\bar{1}^+) \hat{\psi}_H(\bar{1}) \hat{\psi}_H(k) \dots \right\} = \pm \mathcal{T} \left\{ \dots \hat{\psi}_H(k) \hat{\psi}_H(\bar{1}) \hat{\psi}_H^\dagger(\bar{1}^+) \dots \right\}$$

Taking into account that  $\hat{\psi}_H(\bar{1}) \hat{\psi}_H^\dagger(\bar{1}^+)$  is formed by an even number of field operators it works like a bosonic operator under the action of the  $\mathcal{T}$  and can be freely moved. With this trick the first term on the r.h.s. of (D.12) can be written as

$$\begin{aligned}
 & \frac{1}{i^n} \mathcal{T} \left\{ \hat{\psi}_H(1) \dots \left( i \frac{d}{dz_k} \hat{\psi}_H(k) \right) \dots \hat{\psi}_H(n) \hat{\psi}_H^\dagger(n') \dots \hat{\psi}_H^\dagger(1') \right\} \\
 &= h(k) \hat{G}_n(1, \dots, n; 1', \dots, n') \\
 & \quad \pm \frac{1}{i^n} \int d\bar{1} v(k; \bar{1}) \mathcal{T} \left\{ \hat{\psi}_H(1) \dots \hat{\psi}_H(n) \hat{\psi}_H(\bar{1}) \hat{\psi}_H^\dagger(\bar{1}^+) \hat{\psi}_H^\dagger(n') \dots \hat{\psi}_H^\dagger(1') \right\} \\
 &= h(k) \hat{G}_n(1, \dots, n; 1', \dots, n') \pm i \int d\bar{1} v(k; \bar{1}) \hat{G}_{n+1}(1, \dots, n, \bar{1}; 1', \dots, n', \bar{1}^+)
 \end{aligned}$$

and a similar one for (D.13).

Using (D.15) and (D.16) in (D.12) and (D.13), and inserting the result before, the final equations of motion for the Green's function are:

$$\begin{aligned}
 & \left[ i \frac{d}{dz_k} - h(k) \right] \hat{G}_n(1, \dots, n; 1', \dots, n') \\
 &= \pm i \int d\bar{1} v(k; \bar{1}) \hat{G}_{n+1}(1, \dots, n, \bar{1}; 1', \dots, n', \bar{1}^+) \\
 & \quad + \sum_{j=1}^n (\pm)^{k+j} \delta(k; j') \hat{G}_{n-1}(1, \dots, \cancel{k} \dots, n; 1', \dots, \cancel{j'} \dots, n')
 \end{aligned} \tag{D.17}$$

and

$$\begin{aligned}
 & \hat{G}_n(1, \dots, n; 1', \dots, n') \left[ -i \frac{\overleftarrow{d}}{dz'_k} - h(k') \right] \\
 &= \pm i \int d\bar{1} v(k'; \bar{1}) \hat{G}_{n+1}(1, \dots, n, \bar{1}^-; 1', \dots, n', \bar{1}) \\
 & \quad + \sum_{j=1}^n (\pm)^{k'+j} \delta(j; k') \hat{G}_{n-1}(1, \dots, \cancel{j} \dots, n; 1', \dots, \cancel{k'} \dots, n')
 \end{aligned} \tag{D.18}$$

Thus, the derivative of  $\hat{G}_n$  is expressed in terms of  $\hat{G}_{n-1}$  and  $\hat{G}_{n+1}$ . These are the general equations of motion for the Green's functions, which constitute the Martin-Schwinger Hierarchy, whose complexity is far beyond the scope of this thesis. However, its knowledge derivation is necessary to present the useful simplifications of the One-body and Two-body Green's functions we are going to use explained in E.

### D.3 THE GREEN'S FUNCTION AS THE AVERAGE OF THE CORRELATORS

To transform the Martin-Schwinger hierarchy for the Green's function operators into a coupled set of differential equations we need to take the average by means of the

density matrix operator  $\hat{\rho} = e^{-\beta\hat{H}_M}/Z$  as seen in Appendix H.1 to get the  $n$ -body Green's function  $G_n$ :

$$\begin{aligned}
 G_n(1, \dots, n; 1', \dots, n') &\equiv \frac{\text{Tr} \left[ e^{-\beta\hat{H}_M} \hat{G}_n(1, \dots, n; 1', \dots, n') \right]}{\text{Tr} \left[ e^{-\beta\hat{H}_M} \right]} \\
 &= \frac{1}{i^n} \frac{\text{Tr} \left[ \mathcal{T} \left\{ e^{-\iota \int_{\gamma} d\bar{z} \hat{H}(\bar{z})} \hat{\psi}(1) \dots \hat{\psi}(n) \hat{\psi}^\dagger(n') \dots \hat{\psi}^\dagger(1') \right\} \right]}{\text{Tr} \left[ e^{-\beta\hat{H}_M} \right]}
 \end{aligned}
 \tag{D.19}$$

Given the Martin-Schwinger hierarchy, which constitutes in any case the system of equations to be solved, what remains to be determined to provide a unique solution are the spatial and temporal boundary conditions. The spatial boundary conditions of the Green's function are the same as the ones for the wavefunctions of the many-body states. For the boundary conditions on the time-dependence, since the equations of motion for each Green's function  $\hat{G}_n$  are first order in contour ordered time  $z_k$  we also need one condition per time-argument  $z_1, \dots, z_k, \dots, z_n$ . From (D.19) it follows:

$$\boxed{
 \begin{aligned}
 G_n(1, \dots, \mathbf{x}_k, z_i, \dots, n; 1', \dots, n') &= \pm G_n(1, \dots, \mathbf{x}_k, z_f, \dots, n; 1', \dots, n') \\
 G_n(1, \dots, n; 1', \dots, \mathbf{x}'_k, z_i, \dots, n') &= \pm G_n(1, \dots, n; 1', \dots, \mathbf{x}'_k, z_f, \dots, n')
 \end{aligned}
 }
 \tag{D.20}$$

where the sign  $\pm$  makes the difference for bosonic/fermionic operators. As a consequence, the Green's functions are (anti)periodic along the time contour  $\gamma$ . The boundary conditions (D.20) receive the name of *Kubo-Martin-Schwinger (KMS) relations*.

THE MEAN-FIELD APPROXIMATION: HARTREE-FOCK  
AND THE DYSON EQUATION

---

E.1 THE HARTREE-FOCK APPROXIMATION

By writing down the lowest order equations of motion in the Martin-Schwinger hierarchy (D.17) and (D.18), the only useful throughout the scope of this thesis, we get the one-  $G(1; 2) = \hat{G}_1(\mathbf{x}_1, z_1; \mathbf{x}_2, z_2)$  and two-particle  $G_2(1, 2; 1', 2') = G_2(\mathbf{x}_1, z_1, \mathbf{x}_2, z_2; \mathbf{x}'_1, z'_1, \mathbf{x}'_2, z'_2)$  Green's functions. For the sake of simplicity we avoid the subscript 1 in the one-particle Green's function. The form of  $G_0$  is trivial, because of the lack of creation and annihilation operators,  $G_0 = \hat{1}$ . For  $G_1(1; 1')$ , which has a creation operator and an annihilation one:

$$\left[ \imath \frac{d}{dz_1} - h(1) \right] G(1; 1') = \delta(1; 1') \pm \imath \int d2v(1; 2)G_2(1, 2; 1', 2^+) \quad (\text{E.1})$$

$$G(1; 1') \left[ -\imath \frac{d}{dz'_1} - h(1') \right] = \delta(1; 1') \pm \imath \int d2v(1'; 2)G_2(1, 2^-; 1', 2) \quad (\text{E.2})$$

Notice that  $2^+ = \mathbf{x}_2, z_2^+$  takes place infinitesimally after  $2 = \mathbf{x}_2, z_2$  in the time contour, while  $2^- = \mathbf{x}_2, z_2^-$  infinitesimally before.

We can do the same with the equations of motion of  $G_2$ , which have two creation operators and two annihilation ones, and therefore four position-spin-time coordinates and entries. Differentiating with respect to the four time coordinates, four equations arise:

$$\begin{aligned} \left[ \imath \frac{d}{dz_1} - h(1) \right] G_2(1, 2; 1', 2') &= \delta(1; 1')G(2; 2') \pm \delta(1; 2')G(2; 1') \\ &\pm \imath \int d3v(1; 3)G_3(1, 2, 3; 1', 2', 3^+) \end{aligned} \quad (\text{E.3})$$

$$\begin{aligned} \left[ \imath \frac{d}{dz_2} - h(2) \right] G_2(1, 2; 1', 2') &= \pm \delta(2; 1')G(1; 2') + \delta(2; 2')G(2; 1') \\ &\pm \imath \int d3v(2; 3)G_3(1, 2, 3; 1', 2', 3^+) \end{aligned} \quad (\text{E.4})$$

$$G_2(1, 2; 1', 2') \left[ -\iota \frac{\overleftarrow{d}}{dz_1'} - h(1') \right] = \delta(1; 1')G(2; 2') \pm \delta(2; 1')G(1; 2') \pm \iota \int d3v(1'; 3)G_3(1, 2, 3^-; 1', 2', 3) \quad (\text{E.5})$$

$$G_2(1, 2; 1', 2') \left[ -\iota \frac{\overleftarrow{d}}{dz_2'} - h(2') \right] = \pm \delta(1; 2')G(2; 1') + \delta(2; 2')G(1; 1') \pm \iota \int d3v(2'; 3)G_3(1, 2, 3^-; 1', 2', 3) \quad (\text{E.6})$$

Because of the complexity of the  $G_2(1, 2; 1', 2')$ 's, we are looking for correlator operators quadratic in the field operators, as is the case of  $G(1; 1')$ . Thus, an approximation for  $G_2(1, 2; 1', 2')$  which truncates the Martin-Schwinger hierarchy and avoids the use of higher order Green's functions is desired. Let's try:

$$G_2(1, 2; 1', 2') = G(1; 1')G(2; 2') \pm G(1; 2')G(2; 1') + \Upsilon(1, 2; 1', 2') \quad (\text{E.7})$$

where we have implicitly defined the four position-spin-time correlation function  $\Upsilon(1, 2; 1', 2')$ . If the interaction  $v = 0$ , the above  $G_2$  with  $\Upsilon = 0$  is a solution of the equations of motion in the Martin-Schwinger hierarchy. Inserting (E.7) into (E.3) with  $\Upsilon = 0$  and  $v = 0$ :

$$\left[ \iota \frac{d}{dz_1} - h(1) \right] [G_1(1; 1')G_1(2; 2') \pm G_1(1; 2')G_1(2; 1')] = \delta(1; 1')G(2; 2') \pm \delta(1; 2')G(2; 1')$$

This  $G_2$  inherits from  $G$  the satisfaction of the KMS boundary conditions and therefore, if the exact noninteracting  $G$  is used, this will be exactly the corresponding noninteracting  $G_2$ . Thus, for weak interactions, we eliminate the remaining four coordinates Green's function  $\Upsilon \approx 0$  and

$$G_2(1, 2; 1', 2') = G(1; 1')G(2; 2') \pm G(1; 2')G(2; 1') \quad (\text{E.8})$$

This Ansatz for the second order  $G_2$ , which is the average of a quartic product of the field operators, in terms of only first order Green's functions  $G$ , which are quadratic, is called the *Hartree-Fock approximation*. Inserting this approximation into the equations (E.1) and (E.2) for  $G$ :

$$\begin{aligned} \left[ \iota \frac{d}{dz_1} - h(1) \right] G(1; 1') &= \delta(1; 1') \pm \iota \int d2v(1; 2) [G(1; 1')G(2; 2') \pm G(1; 2')G(2; 1')] \\ &= \delta(1; 1') + \int d2\Sigma(1; 2)G(2; 1') \end{aligned} \quad (\text{E.9})$$

$$\begin{aligned}
 G(1; 1') \left[ -i \frac{\overleftarrow{d}}{dz_1'} - h(1') \right] &= \delta(1; 1') \pm i \int d2 v(1'; 2) [G(1; 1')G(2; 2') \pm G(1; 2')G(2; 1')] \\
 &= \delta(1; 1') + \int d2 G(1; 2) \Sigma(2; 1')
 \end{aligned}
 \tag{E.10}$$

where we have defined the integral kernel  $\Sigma$  as:

$$\Sigma(1; 2) = \delta(1; 2) V_H(1) + v(1; 2) G(1; 2^+)$$

with  $V_H(1) = \pm i \int d3 v(1; 3) G(3; 3^+) = \int d\mathbf{x}_3 v(\mathbf{x}_1, \mathbf{x}_3, z_1) n(\mathbf{x}_3, z_1)$ . Notice that  $v(1; 3) = \delta(z_1, z_3) v(\mathbf{x}_1, \mathbf{x}_3, z_1)$  and  $\pm i G(\mathbf{x}_3, z_1; \mathbf{x}_3, z_1^+) = n(\mathbf{x}_3, z_1)$ . Remember from equations (D.17) and (D.18) that the infinitesimal delay in time between  $z_1$  and  $z_1^+$ ,  $z_2$  and  $z_2^+$  or  $z_2^-$  and  $z_2$  is the trick to maintain equal-time creation operators to the right and get the correct Green's function operators. The *Hartree potential*  $V_H(\mathbf{x}_1, z_1)$  has a clear physical interpretation as the classical potential that a particle in  $x_1$  experiences from a density distribution  $n$  of all the particles in the system (for Coulombic interactions  $v(\mathbf{x}_1, \mathbf{x}_3, z_1) = 1/|\mathbf{r}_1 - \mathbf{r}_3|$  the Hartree potential is the potential of classical electrostatics). The integral kernel  $\Sigma$  which is known as the *self-energy*. While the first term of  $\Sigma$  is  $V_H$ , the second one is the *Fock* or *exchange potential*, which is local in time but non-local in space and has no classical interpretation.

### E.1.1 The Dyson equations

The equations (E.9) and (E.10) are self-consistent as  $\Sigma$  depends on the  $G$  itself. To write the solution in integral form, using the KMS boundary conditions, we define the noninteracting Green's function  $G_0$  as the solution of the equations of motion with  $v = 0$ ,

$$\left[ i \frac{d}{dz_1} - h(1) \right] G_0(1; 1') = \delta(1; 1') \tag{E.11}$$

$$G_0(1; 1') \left[ -i \frac{\overleftarrow{d}}{dz_1'} - h(1') \right] = \delta(1; 1') \tag{E.12}$$

Taking equations (E.9) and (E.10) with  $v = 0$ , we have:

$$\left[ i \frac{d}{dz_1} - h(1) \right] G(1; 1') = \delta(1; 1') \tag{E.13}$$

$$G(1; 1') \left[ -\imath \frac{\overleftarrow{d}}{dz'_1} - h(1') \right] = \delta(1; 1') \quad (\text{E.14})$$

Multiplying (E.13) by  $G_0(2; 1)$  from the left and integrating by parts in  $z_1$ , taking into account that  $d1 \equiv dx_1 dz_1$ :

$$\begin{aligned} & \int d1 G_0(2; 1) \left[ \imath \frac{d}{dz_1} - h(1) \right] G(1; 1') \\ &= \int \underbrace{G_0(2; 1)}_u \underbrace{\left( \imath \frac{d}{dz_1} \right) G(1; 1')}_{dw} d1 + \int d1 G_0(2; 1) (-h(1)) G(1; 1') \\ &= \int \underbrace{G_0(2; 1)}_{-du} \underbrace{\left( -\imath \frac{\overleftarrow{d}}{dz'_1} \right) d1}_{\overleftarrow{d}} \underbrace{G(1; 1')}_w + \imath \int \underbrace{dx_1 G_0(2; \mathbf{x}_1, z_1)}_{u \times w} \underbrace{G(\mathbf{x}_1, z_1; 1')}_{w} \Big|_{z_1=z_i}^{z_1=z_f} \\ &+ \int d1 G_0(2; 1) (-h(1)) G(1; 1') \\ &= \int d1 \underbrace{G_0(2; 1)}_{\delta(2;1)} \left[ -\imath \frac{\overleftarrow{d}}{dz'_1} - h(1) \right] G(1; 1') \\ &+ \imath \int \underbrace{dx_1 G_0(2; \mathbf{x}_1, z_1) G(\mathbf{x}_1, z_1; 1')}_{0 \text{ due to KMS b.c.}} \Big|_{z_1=z_i}^{z_1=z_f} \\ &= \int d1 \delta(2; 1) G(1; 1') = \boxed{G(2; 1')} \end{aligned} \quad (\text{E.15})$$

Because of the KMS boundary conditions we know that  $G_0(2; \mathbf{x}_1, z_f) = \pm G_0(2; \mathbf{x}_1, z_i)$  and also  $G(\mathbf{x}_1, z_f; 1') = \pm G(\mathbf{x}_1, z_i; 1')$ , so that in both, the bosonic (+) and the fermionic (−) cases the integral

$$\imath \int dx_1 G_0(2; \mathbf{x}_1, z_1) G(\mathbf{x}_1, z_1; 1') \Big|_{z_1=z_i}^{z_1=z_f} = 0$$

vanishes.

The integrals for (E.14) work the same way, so that:

$$\int d1' G(1; 1') \left[ -\imath \frac{\overleftarrow{d}}{dz'_1} - h(1') \right] G_0(1'; 2) = G(1; 2) \quad (\text{E.16})$$

Multiplying both equations (E.9) and (E.10) by  $G_0$  from the left and using (E.15) and (E.16) we obtain the *Dyson equations* for the Green's function:

$$\boxed{\begin{aligned} G(1; 2) &= G_0(1; 2) + \int d3d4 G_0(1; 3) \Sigma(3; 4) G(4; 2) \\ G(1; 2) &= G_0(1; 2) + \int d3d4 G(1; 3) \Sigma(3; 4) G_0(4; 2) \end{aligned}} \quad (\text{E.17})$$

The difference between the Dyson equations and the integro-differential equations (E.9) and (E.10) is that in the Dyson equations the boundary conditions are incorporated through  $G_0$ . The exact Green's function  $G$  satisfies a Dyson equation in which  $\Sigma$  depends in a more complicated manner on  $G$ . *The Dyson equation is, thus, the solution of the Martin-Schwinger hierarchy for the one-particle Green's function.*

If converted to the general basis of the  $\varphi(\mathbf{r})$ 's:

$$\begin{aligned} G_{ji}(z_1; z_2) &= G_{0,ji}(z_1; z_2) \\ &+ \sum_{ijkl} \int_{\gamma} dz_3 dz_4 G_{0,jk}(z_1; z_3) \Sigma_{kl}(z_3; z_4) G_{li}(\mathbf{r}_4, z_4; \mathbf{r}_2, z_2) \\ G_{ji}(z_1; z_2) &= G_{0,ji}(z_1; z_2) \\ &+ \sum_{ijkl} \int_{\gamma} dz_3 dz_4 G_{jk}(z_1; z_3) \Sigma_{kl}(z_3; z_4) G_{0,li}(\mathbf{r}_4, z_4; \mathbf{r}_2, z_2) \end{aligned} \quad (\text{E.18})$$

And to the more suitable first quantization operator form:

$$\begin{aligned} \hat{G}(z_1; z_2) &= \hat{G}_0(z_1; z_2) \\ &+ \int_{\gamma} dz_3 dz_4 \hat{G}_0(z_1; z_3) \hat{\Sigma}(z_3; z_4) \hat{G}(\mathbf{r}_4, z_4; \mathbf{r}_2, z_2) \\ \hat{G}(z_1; z_2) &= \hat{G}_0(z_1; z_2) \\ &+ \int_{\gamma} dz_3 dz_4 \hat{G}(z_1; z_3) \hat{\Sigma}(z_3; z_4) \hat{G}_0(\mathbf{r}_4, z_4; \mathbf{r}_2, z_2) \end{aligned} \quad (\text{E.19})$$

## THE EMBEDDING SELF-ENERGY

---

### F.1 THE EMBEDDING SELF-ENERGY

To calculate the Green's function, the density matrix and all the properties of the central region in (1.5) caused by the surrounding reservoirs, according to the spatial division in the Caroli partition scheme (Datta, 1995; Caroli et al., 1971), we make use of a useful tool called wembedding self-energy  $\Sigma_{em}(z, z')$ . This self-energy reproduces in the central region  $C$  the effects of the reservoirs, so that its definition is only useful after partitioning. For interacting systems, we can write the Kadanoff-Baym equations in its matricial form, by transforming equations (1.34) and (1.35) from the position-spin representation to the general basis of the  $\phi_i(\mathbf{r})$ 's:

$$\left[ v \frac{d}{dz} - h(z) \right] G(z, z') = \delta(z, z') + \int_{\gamma} d\bar{z} \Sigma(z, \bar{z}) G(\bar{z}, z') \quad (\text{F.1})$$

and

$$G(z, z') \left[ -v \frac{\overleftarrow{d}}{dz'} - \hat{h}(z') \right] = \delta(z, z') + \int_{\gamma} d\bar{z} G(z, \bar{z}) \Sigma(\bar{z}, z') \quad (\text{F.2})$$

where the self-energy has to satisfy:

$$\int_{\gamma} d\bar{z} \Sigma(z, \bar{z}) G(\bar{z}, z') = \pm v \int_{\gamma} d\bar{z} v(z, \bar{z}) G_2(z, \bar{z}; z', \bar{z}^+) \quad (\text{F.3})$$

With the equations written in the general basis, following the Caroli partition scheme (Datta, 1995; Caroli et al., 1971) we separate the full Hamiltonian, the self-energy and the Green's function matrices in blocks for the central region  $C$  and the reservoirs labelled  $\alpha = 1, 2, \dots$ . Each block in the matrices corresponds to the projec-

tion of the full matrix onto the subspace corresponding to this reservoir or onto the subspace of the central region  $C$ .

$$h = \begin{pmatrix} h_{11} & 0 & 0 & \dots & h_{1C} \\ 0 & h_{22} & 0 & \dots & h_{2C} \\ 0 & 0 & h_{33} & \dots & h_{3C} \\ \cdot & \cdot & \cdot & \cdot & \cdot \\ \cdot & \cdot & \cdot & \cdot & \cdot \\ \cdot & \cdot & \cdot & \cdot & \cdot \\ h_{C1} & h_{C2} & h_{C3} & \dots & h_{CC} \end{pmatrix} \quad (\text{F.4})$$

If we compare to (1.5), we can identify the reservoir on-diagonal element  $[h_{\alpha\alpha'}]_{kk'} = \delta_{\alpha\alpha'} \delta_{kk'} \epsilon_{k\alpha}$ , the off-diagonal interaction between reservoir alpha and the central region  $[h_{\alpha C}]_{km} = T_{k\alpha m}$ , and the on-diagonal block which represents the projection onto the central region  $h_{CC}$ , whose elements  $[h_{CC}]_{mn} = H_{mn}^C$ .

While the Hamiltonian matrix  $h$  has 'zero' blocks in the off-diagonal blocks that connect subspaces whose interaction vanish, the Green's function matrix  $G$  is non-zero everywhere, and the self-energy  $\Sigma$  has only one non-vanishing block, which is  $\Sigma_{CC}$ .

The projections of equation (F.1) onto the blocks corresponding to the on-diagonal central region  $CC$ , and the off-diagonal block  $\alpha C$ , encoding the interaction between the central region and reservoir  $\alpha$  are:

$$\begin{aligned} \left[ i \frac{d}{dz} - h_{CC}(z) \right] G_{CC}(z, z') &= \delta(z, z') \\ + \sum_{\alpha} h_{C\alpha}(z) G_{\alpha C}(z, z') &+ \int_{\gamma} d\bar{z} \Sigma_{CC}(z, \bar{z}) G_{CC}(\bar{z}, z') \end{aligned} \quad (\text{F.5})$$

where the sum includes only the non-vanishing matrix elements  $\langle i | h_{C\alpha} | k\alpha \rangle \neq 0$ . In the central region  $CC$ , the self-energy is non-zero only in the subspace whose Hamiltonian interaction with any of the reservoirs does not vanish.

$$\left[ i \frac{d}{dz} - h_{\alpha\alpha}(z) \right] G_{\alpha C}(z, z') = h_{\alpha C}(z) G_{CC}(z, z') \quad (\text{F.6})$$

The solution for (F.6) is:

$$G_{\alpha C}(z, z') = \int_{\gamma} d\bar{z} g_{\alpha\alpha}(z, \bar{z}) h_{\alpha C}(\bar{z}) G_{CC}(\bar{z}, z') \quad (\text{F.7})$$

where the Green's function on-diagonal block  $g_{\alpha\alpha}$  on the subspace of the isolated contact  $\alpha$  solves the noninteracting Kadanoff-Baym equation (1.26), under the KMS boundary conditions in time, projected onto this reservoir:

$$\left[ i \frac{d}{dz} - h_{\alpha\alpha}(z) \right] g_{\alpha\alpha}(z, z') = \delta(z, z') \quad (\text{F.8})$$

Recall that the Green's function  $g_{\alpha\alpha}$  is noninteracting and its solution does not depend on any interaction with the central region. Since the projection of the Hamiltonian in this block  $h_{\alpha\alpha}(z)$  is diagonal with matrix elements  $\epsilon_{k\alpha}(z)$ , the solution is  $[g_{\alpha\alpha}]_{kk'}(z, z') = \delta_{\alpha\alpha} \delta_{kk'} g_{k\alpha}(z, z')$ , where:

$$g_{k\alpha}(z, z') = -i \left[ \theta(z, z') \bar{f}(\epsilon_{k\alpha}^M) - \theta(z', z) f(\epsilon_{k\alpha}^M) \right] e^{-i \int_{z'}^z d\bar{z} \epsilon_{k\alpha}(\bar{z})} \quad (\text{F.9})$$

where  $\epsilon_{k\alpha}^M = \epsilon_{k\alpha} - \mu$ . Inserting (F.7) in (F.5) it results:

$$\sum_{\alpha} h_{C\alpha}(z) G_{\alpha C}(z, z') = \int d\bar{z} \Sigma_{em}(z, \bar{z}) G_{CC}(\bar{z}, z') \quad (\text{F.10})$$

where the embedding self-energy  $\Sigma_{em}(z, z')$  is defined as:

$$\begin{aligned} \Sigma_{em}(z, z') &= \sum_{\alpha} \Sigma_{\alpha}(z, z') \\ \Sigma_{\alpha}(z, z') &= h_{C\alpha}(z) g_{\alpha\alpha}(z, z') h_{\alpha C}(z') \end{aligned} \quad (\text{F.11})$$

which is also an interaction independent quantity, and is completely determined by the noninteracting Hamiltonian of the reservoir  $h_{\alpha\alpha}$  and by off-diagonal contact Hamiltonian  $h_{\alpha C}$ .

Using (F.11), the Kadanoff-Baym equation of the central region  $C$  becomes:

$$\begin{aligned} \left[ i \frac{d}{dz} - h_{CC}(z) \right] G_{CC}(z, z') &= \delta(z, z') \\ + \int_{\gamma} d\bar{z} [\Sigma_{CC}(z, \bar{z}) + \Sigma_{em}(z, \bar{z})] G_{CC}(\bar{z}, z') & \end{aligned} \quad (\text{F.12})$$

Equation (F.12) is not an approximation, but an exact closed equation for the projection  $G_{CC}(z, z')$  of the Green's function in the central region, including both, the Hartree-Fock self-energy  $\Sigma_{CC}(z, \bar{z})$ , which includes the interaction and correlations strictly inside the central region, and whose structure is described in appendix H, and  $\Sigma_{em}(z, \bar{z})$ , which incorporates the effects of the surroundings. It is practical to be implemented computationally because of its finite size.

If we now want to calculate the Green's function of the reservoir after the perturbation  $G_{\alpha\alpha}(z, z')$ :

$$\left[ i \frac{d}{dz} - h_{\alpha\alpha}(z) \right] G_{\alpha\alpha}(z, z') = \delta(z, z') + h_{\alpha C}(z) G_{C\alpha}(z, z') \quad (\text{F.13})$$

taking the adjoint of (F.7)

$$G_{C\alpha}(z, z') = \int_{\gamma} d\bar{z} G_{CC}(z, \bar{z}) h_{C\alpha}(\bar{z}) g_{\alpha\alpha}(\bar{z}, z') \quad (\text{F.14})$$

and substituting  $G_{C\alpha}(z, z')$  into (F.13)

$$\begin{aligned} \left[ i \frac{d}{dz} - h_{\alpha\alpha}(z) \right] G_{\alpha\alpha}(z, z') &= \delta(z, z') \\ &+ \int_{\gamma} d\bar{z} \Sigma_{in,\alpha}(z, \bar{z}) g_{\alpha\alpha}(\bar{z}, z') \end{aligned} \quad (\text{F.15})$$

where the inbedding self-energy  $\Sigma_{in,\alpha}(z, z')$  for reservoir  $\alpha$  plays the inverse role of the embedding one and is defined as:

$$\Sigma_{in,\alpha}(z, z') = h_{\alpha C}(z) G_{CC}(z, z') h_{C\alpha}(z') \quad (\text{F.16})$$

and after integrating (F.15):

$$\begin{aligned} G_{\alpha\alpha}(z, z') &= g_{\alpha\alpha}(z, z') \\ &+ \int_{\gamma} d\bar{z} d\bar{z}' g_{\alpha\alpha}(z, \bar{z}) \Sigma_{in,\alpha}(\bar{z}, \bar{z}') g_{\alpha\alpha}(\bar{z}', z') \end{aligned} \quad (\text{F.17})$$

we get the integral solution for lead's  $\alpha$  Green's function, which is useful to calculate physical quantities in the reservoir as is the case of the density, charge, current, energy, etc.

If the Green's functions of the reservoirs in (F.11) are considered to be in steady-state, the retarded/advanced embedding self-energy can be Fourier transformed to the frequency domain:

$$\begin{aligned} \Sigma_{em}(E) &= \sum_{\alpha} \Sigma_{\alpha}(E) \\ \Sigma_{\alpha}^{R/A}(E) &= h_{C\alpha}(E) g_{\alpha\alpha}^{R/A}(E) h_{\alpha C}(E) \end{aligned} \quad (\text{F.18})$$

Converting to the first quantization operator notation:

$$\begin{aligned}
 \hat{\Sigma}_\alpha^{R/A}(E) &= \sum_{\substack{j,i \\ k\alpha,l\alpha}} |j\rangle \langle j| h_{C\alpha}(E) |k\alpha\rangle \\
 &\quad \langle k\alpha| g_{\alpha\alpha}^{R/A}(E) |l\alpha\rangle \langle l\alpha| h_{\alpha C}(E) |i\rangle \langle i| \\
 &= \sum_{\substack{j,i \\ k\alpha,l\alpha}} |j\rangle h_{C\alpha,jk\alpha}(E) g_{\alpha\alpha,k\alpha l\alpha}^{R/A}(E) h_{\alpha C,l\alpha j}(E) \langle i|
 \end{aligned} \tag{F.19}$$

and every matrix element:

$$\Sigma_{\alpha,ji}^{R/A}(E) = \sum_{k\alpha,l\alpha} h_{C\alpha,jk\alpha}(E) g_{\alpha\alpha,k\alpha l\alpha}^{R/A}(E) h_{\alpha C,l\alpha i}(E) \tag{F.20}$$

where, of course, the retarded/advanced unperturbed Green's function matrix  $g_{\alpha\alpha}^{R/A}(E)$  has to satisfy the Fourier transform of (F.8):

$$g_{\alpha\alpha}^{R/A}(E) = \frac{1}{((E \pm i\eta)\hat{\mathbb{1}}_{\alpha\alpha} - h_{\alpha\alpha})} \tag{F.21}$$

so that the first quantization operator for the retarded/advanced embedding self-energy reduces to:

$$\hat{\Sigma}_\alpha^{R/A}(E) = \sum_{ji} |j\rangle \Sigma_{\alpha,ji}^{R/A}(E) \langle i| \tag{F.22}$$

The embedding self-energy operator of each reservoir  $\alpha$  and the total one can be separated in their real and an imaginary parts:

$$\hat{\Sigma}_\alpha^{R/A}(E) = \hat{\Lambda}_\alpha(E) \mp \frac{i}{2} \hat{\Gamma}_\alpha(E) \tag{F.23}$$

Where we have defined the rate operator  $\hat{\Gamma}_\alpha(E)$ . With this definition, the spectral function operator in equation (H.10), if projected onto the central region  $C$ , in the same way as the lesser/greater Green's function operators in equation (F.25) and the embedding self-energy in (F.18), can be separated into components corresponding to each reservoir:

$$\begin{aligned}
 \hat{A}(E) &= \sum_\alpha \hat{A}_\alpha(E) \\
 \hat{A}_\alpha(E) &= \hat{\mathcal{G}}^R(E) \hat{\Gamma}_\alpha(E) \hat{\mathcal{G}}^A(E)
 \end{aligned} \tag{F.24}$$

The lesser/greater Green's function  $G^{\lessgtr}$  can be decomposed in as many components as reservoirs are present, in other words, in as many components as embedding

Self-Energy operators  $\hat{\Sigma}_\alpha$  are added to the Hamiltonian. Following (F.23) for the partial self-energies and (H.11) for the lesser/greater Green's functions, we define the partial spectral lesser/greater Green's function operators  $\hat{\mathcal{G}}_\alpha^{\lessgtr}(E)$ . Each of these partial lesser/greater Green's function operators  $\alpha$ , expressed in the frequency domain, takes the form:

$$\hat{\mathcal{G}}_\alpha^{\lessgtr}(E) = \hat{\mathcal{G}}^R(E) \hat{\Sigma}_\alpha^{\lessgtr}(E) \hat{\mathcal{G}}^A(E) \quad (\text{F.25})$$

where

$$\hat{\Sigma}_\alpha^<(E) = i\hat{\Gamma}_\alpha(E) f(E - \mu_\alpha) \quad (\text{F.26})$$

and

$$\hat{\Sigma}_\alpha^>(E) = i\hat{\Gamma}_\alpha(E) \bar{f}(E - \mu_\alpha) \quad (\text{F.27})$$

where  $\hat{\Gamma}_\alpha(E)$  is twice the imaginary part of the retarded self-energy as defined in appendix H, and  $f$  and  $\bar{f}$  the Fermi function and its complementary, defined in equation (H.6).

In a similar manner as (F.25), in steady-state, the convolution in (F.17) reduces to a conventional product:

$$G_{\alpha\alpha}^{R/A}(E) = g_{\alpha\alpha}^{R/A}(E) + g_{\alpha\alpha}^{R/A}(E) \Sigma_{in,\alpha}^{R/A}(E) g_{\alpha\alpha}^{R/A}(E) \quad (\text{F.28})$$

and in first quantization operator form:

$$\hat{\mathcal{G}}_{\alpha\alpha}^{R/A}(E) = \hat{g}_{\alpha\alpha}^{R/A}(E) + \hat{g}_{\alpha\alpha}^{R/A}(E) \hat{\Sigma}_{in,\alpha}^{R/A}(E) \hat{g}_{\alpha\alpha}^{R/A}(E) \quad (\text{F.29})$$

where the only non-vanishing matrix elements  $\langle i | \hat{\mathcal{G}}_{\alpha\alpha}^{R/A}(E) | j \rangle$  are those with  $\varphi_i(\mathbf{r})$  and  $\varphi_j(\mathbf{r})$  located in the  $\alpha$  reservoir's partition.

From the matrix elements of (F.25), we define the partial spectral density of states  $DOS_\alpha(E)$  and the partial density matrix  $\rho_\alpha$  as:

$$\begin{aligned} DOS_\alpha(E) &= -i\hat{G}_\alpha^<(E) \\ \rho_{\alpha,ij} &= \int_{-\infty}^{\infty} dE DOS_{\alpha,ij}(E) \end{aligned} \quad (\text{F.30})$$

from which we can calculate the partial numbers of particles injected from each lead:

$$N_\alpha = Tr[\rho_\alpha] \quad (\text{F.31})$$

## THE SELF-CONSISTENT METHOD

The self-consistent calculation then proceeds by computing the input density matrix to the next iteration from the correlation function computed in the current iteration:

$$\rho(\mathbf{r}) = \sum_{ij} \rho_{ij} \varphi_i(\mathbf{r}) \varphi_j^*(\mathbf{r}) = \int \frac{dE}{2\pi i} G^<(\mathbf{r}, \mathbf{r}; E) = \sum_{ij} \int \frac{dE E}{2\pi i} G_{ij}^<(E) \varphi_i(\mathbf{r}) \varphi_j^*(\mathbf{r}) \quad (\text{G.1})$$

or in the matrix formulation.

$$\rho_{ij} = \int \frac{dE E}{2\pi i} G_{ij}^<(E) \quad (\text{G.2})$$

The density matrix is nothing but the energy integration of the matrix correlation function. To see better the physical meaning of this, we divide both sides of Eq. (5.11) by:

$$A(E) = i(G^R(E)G^A(E)) = G^R(E)[\Gamma_L(E) + \Gamma_R(E)]G^A(E) \quad (\text{G.3})$$

and get:

$$\begin{aligned} \frac{-iG^<(E)}{A(E)} &= f(E - \mu_L)\gamma_L - f(E - \mu_R)\gamma_R, \\ \gamma_L &= G^R(E)\Gamma_L(E)G^A(E)/A(E) \\ \gamma_R &= G^R(E)\Gamma_R(E)G^A(E)/A(E) \end{aligned} \quad (\text{G.4})$$

where the coefficient-wise division of matrices is defined such that  $[\frac{A}{B}]_{ij} = \frac{A_{ij}}{B_{ij}}$ . Since the correlation function  $-iG^<$  describes the number of electrons at energy  $E$  and the spectral function  $A$  describes the density of states at energy  $E$ , the above equation essentially says that the probability of the states at energy  $E$  being occupied in the molecule equals the probability of it being occupied in the left electrode multiplying the escape rate  $\gamma_L$  from the left electrode to the molecule plus the probability of it being occupied in the right electrode multiplying the escape rate  $\gamma_R$  from the right electrode to the molecule. Note the integration contour appearing in Eq. (5.13) is along the real energy axis rather than in the complex energy plane. Unlike the retarded Green's function, the correlation Green's function  $-iG^<(E)$  is not analytic away from the real energy axis. This would have increased significantly the computational cost of the energy integration. However, for energy sufficiently lower than both

$\mu_L$  and  $\mu_R$ , say  $E < \mu_{L(R)} - 10kT$ , we have  $f(E - \mu_{L(R)}) \approx 1$  and Eq. (5.11) reduces to:

$$G^<(E) = i[G^R(E)\Gamma_L(E)G^A(E)] + i[G^R(E)\Gamma_R(E)G^A(E)] = G_L^<(E) + G_R^<(E) \quad (\text{G.5})$$

Comparing with Eq. (5.14), we have:

$$G^<(E) = iA(E) = -2i\text{Im}[G^R(E)] \quad (\text{G.6})$$

Consequently the integration over the energy in Eq. (5.13) can be split into two parts:

$$\rho_{ij} = \frac{1}{2\pi i} \int_C dZ G_{ij}^R(Z) + \frac{1}{2\pi i} \int_{\mu_{\text{drain}}}^{\mu_{\text{source}}} dE G_{ij}^<(E) \quad (\text{G.7})$$

The lesser Green's Function inside the Central region can be decomposed into two parts, representing the influx of electrons from each lead (at the corresponding chemical potential):

$$G^<(E) = i[G^R(E)\Gamma_L(E)G^A(E)] + i[G^R(E)\Gamma_R(E)G^A(E)] = G_L^<(E) + G_R^<(E) \quad (\text{G.8})$$

Giving rise to the partial spectral density matrices  $L/R$  inside the device:

$$\rho_{\alpha,ij} = \frac{1}{2\pi i} \int_{-\infty}^{\mu_{\alpha}} dE G_{\alpha,ij}^<(E); \quad \alpha = L, R \quad (\text{G.9})$$

Depending on the point along the Keldysh contour on which the complex plane Green's function operator is evaluated, different components are defined.

Considering a Hamiltonian constant in time  $\hat{h}_{eff}$ , a reasonable assumption for the long-time limit steady-state, which can be noninteracting, or may include the interaction at the Mean-Field level (Hartree-Fock) through a self-energy  $\hat{\Sigma}$ . The usual starting point for the definitions are the frequency domain retarded/advanced Green's function operators in first quantization. The noninteracting Green's function operator  $\hat{\mathcal{G}}_0^{R/A}$  is calculated as:

$$\hat{\mathcal{G}}_0^{R/A}(E) = \frac{1}{E - \hat{h} \pm i\eta} \quad (\text{H.1})$$

while the interacting one  $\hat{\mathcal{G}}^{R/A}$ :

$$\hat{\mathcal{G}}^{R/A}(E) = \frac{1}{E - \hat{h} - \Sigma^{R/A}(E) \pm i\eta} \quad (\text{H.2})$$

where the self-energy  $\Sigma^{R/A}(E)$  can include the embedding self-energy operator defined in equation (F.22) from section F.1, if the system is partitioned as in the Caroli partition scheme, and also the Hartree-Fock self-energy and the correlation one. The Hartree-Fock self energy, derived from equations (1.41) and (1.43) is:

$$\hat{\Sigma}_{HF}^{R/A}(z_1, z_2) = \delta(z_1; z_2) q \hat{\mathcal{V}}_{HF}(t_1) \quad (\text{H.3})$$

in the long-time limit steady state the Hartree-Fock potential operator  $\hat{\mathcal{V}}_{HF}^{R/A}$  does not depend on time, so does not the associated the self-energy. Because of its definition,  $\hat{\Sigma}_{HF}$  is real.

The correlation self energy takes into account all the effects beyond Mean-Field (HF) and has the following structure (Stefanucci & Van Leeuwen, 2010; Stefanucci & Almladh, 2004):

$$\hat{\Sigma}_c(z_1, z_2) = \theta(z_1; z_2) \hat{\Sigma}^>(z_1, z_2) + \theta(z_2; z_1) \hat{\Sigma}^<(z_1, z_2) \quad (\text{H.4})$$

where the lesser/greater Green's function operator remains undefined. From the definition of the rate operator  $\hat{\Gamma}(E)$  in (F.23), in the frequency domain:

$$\begin{aligned} \hat{\Sigma}^<(E) &= \mp i f(E - \mu) \hat{\Gamma}(E) \\ \hat{\Sigma}^>(E) &= -i \bar{f}(E - \mu) \hat{\Gamma}(E) \end{aligned} \quad (\text{H.5})$$

where  $f$  is the Fermi distribution function and  $\bar{f}$  its complementary

$$\begin{aligned} f(E - \mu) &= \frac{1}{1 + e^{-\beta(E - \mu)}} \\ \bar{f}(E - \mu) &= 1 - f(E - \mu) \end{aligned} \quad (\text{H.6})$$

and the rate operator also has to satisfy:

$$\hat{\Gamma}(E) \equiv \imath \left[ \hat{\Sigma}^>(E) - \hat{\Sigma}^<(E) \right] = \imath \left[ \hat{\Sigma}^R(E) - \hat{\Sigma}^A(E) \right] \quad (\text{H.7})$$

Knowing  $\hat{\Gamma}$  we can determine all Keldysh components of  $\hat{\Sigma}$  approaching the real-time axis. The retarded/advanced correlation self-energy operators are calculated by taking (H.4) with real-time arguments, and in the frequency domain by Fourier transforming:

$$\hat{\Sigma}_c(E) = \int \frac{dE'}{2\pi} \frac{\hat{\Gamma}(E')}{E - E' \pm \imath\eta} \quad (\text{H.8})$$

Only the Matsubara self-energy remains to be defined. Approaching the real-frequency axis it is related to the retarded/advanced self-energy operator:

$$\hat{\Sigma}^M(E \pm \imath\eta) = \hat{\Sigma}^{R/A}(E + \mu) \quad (\text{H.9})$$

Now we proceed to define the spectral function operator  $\hat{A}(E)$ :

$$\begin{aligned} \hat{A}(E) &= \imath \left[ \hat{\mathcal{G}}^R(E) - \hat{\mathcal{G}}^A(E) \right] \\ &= \imath \hat{\mathcal{G}}^R(E) \left[ \frac{1}{\hat{\mathcal{G}}^A(E)} - \frac{1}{\hat{\mathcal{G}}^R(E)} \right] \hat{\mathcal{G}}^A(E) \\ &= \imath \hat{\mathcal{G}}^R(E) \left[ \hat{\Sigma}^R(E) - \hat{\Sigma}^A(E) \right] \hat{\mathcal{G}}^A(E) \\ &= \hat{\mathcal{G}}^R(E) \hat{\Gamma}(E) \hat{\mathcal{G}}^A(E) \end{aligned} \quad (\text{H.10})$$

Meanwhile, the lesser/greater Green's function operators can be written in terms of the lesser/greater self-energy, taking into account (H.5), as:

$$\hat{\mathcal{G}}^{\lessgtr}(E) = \hat{\mathcal{G}}^R(E) \hat{\Sigma}^{\lessgtr}(E) \hat{\mathcal{G}}^A(E) \quad (\text{H.11})$$

where the elements of its matrix expression  $G_{ij}$  are proportional to the ones of density of states  $DOS_{ij}(E)$  at energy  $E$  and by integration permit the calculation of the (non)equilibrium steady-state single-particle density matrix  $\rho_{ij}$ :

$$\begin{aligned} DOS(E) &= -i\hat{G}^<(E) \\ \rho_{ij} &= \int_{-\infty}^{\infty} dE DOS_{ij}(E) \end{aligned} \quad (\text{H.12})$$

And the left/right Green's function operators, with one real and one imaginary time argument:

$$\begin{aligned} \hat{G}^{\uparrow}(\tau, t) &\equiv \hat{G}(t_0 - i\tau, t_{\pm}) \\ \hat{G}^{\downarrow}(t, \tau) &\equiv \hat{G}(t_{\pm}, t_0 - i\tau) \end{aligned} \quad (\text{H.13})$$

Approaching the real-frequency axis it is related to the retarded/advanced Green's function operator:

$$\hat{G}^M(E \pm i\eta) = \hat{G}^{R/A}(E + \mu) \quad (\text{H.14})$$

## H.1 STEADY-STATE ENSEMBLE AVERAGES

Taking into account that the partition function, being  $\beta = 1/k_B T$  the inverse temperature and  $E_k^M$  the eigenvalues of the Matsubara Hamiltonian, is defined as:

$$Z = \sum_k e^{-\beta E_k^M} = Tr \left[ e^{-\beta \hat{H}^M} \right] \quad (\text{H.15})$$

and the density matrix operator:

$$\begin{aligned} \hat{\rho} &= \sum_k \rho_k |\Psi_k\rangle \langle \Psi_k| \\ &= \sum_k \frac{e^{-\beta E_k^M}}{Z} |\Psi_k\rangle \langle \Psi_k| = \frac{e^{-\beta \hat{H}^M}}{Z} \end{aligned} \quad (\text{H.16})$$

where the  $|\Psi_k\rangle$ 's form the common set of eigenkets of both, the first quantization Hamiltonian  $\hat{\mathcal{H}}$  and the Matsubara Hamiltonian  $\hat{\mathcal{H}}^M$ :

$$\begin{aligned} \hat{\mathcal{H}} &= \sum_k E_k |\Psi_k\rangle \langle \Psi_k| \\ \hat{\mathcal{H}}^M &= \hat{\mathcal{H}} - \mu \hat{\mathcal{N}} = \sum_k E_k^M |\Psi_k\rangle \langle \Psi_k| \end{aligned} \quad (\text{H.17})$$

The contour-time dependent ensemble average  $O$  of any operator  $\hat{O}$  in second quantization results:

$$\langle O \rangle(z) = \frac{1}{i} \frac{\text{Tr} \left[ e^{-\beta \hat{H}^M} \mathcal{T} \left\{ e^{-i \int_{\gamma} d\bar{z} \hat{H}(\bar{z})} \hat{O}(z) \right\} \right]}{\text{Tr} \left[ e^{-\beta \hat{H}^M} \right]} \quad (\text{H.18})$$

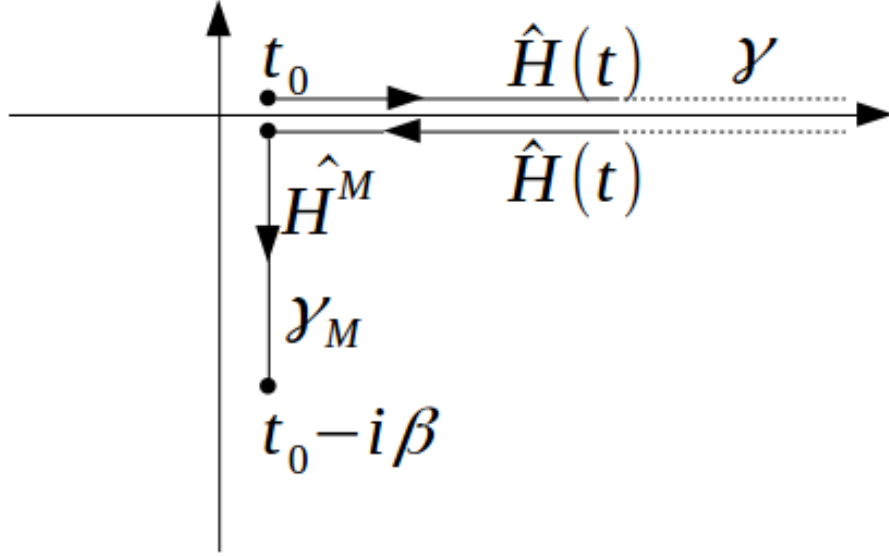


Figure H.1: Contour for the Hamiltonian  $\hat{H}(z)$  to calculate the time-dependent ensemble average of any operator in a system whose time-evolution is governed by the Hamiltonian  $\hat{H}(z)$  from the initial equilibrium in  $t_0$ . The system is supposed to be at temperature  $T$ , being  $\beta = 1/(k_B T)$ .

The statistical average performed after the second equality in (1.2) is equivalent to a time propagation along  $\gamma^M$ , where  $\gamma^M$ , related to the inverse temperature, is any contour from  $z_a$  to  $z_b$  with the constraint  $z_b - z_a = -i\beta$ , (see fig. H.1), resulting in

$$-i \int_{\gamma^M} d\bar{z} \hat{H}(\bar{z}) = -\beta \hat{H}^M \quad (\text{H.19})$$

so that the most simple  $\gamma^M$  is a vertical segment  $\overrightarrow{z_a z_b}$  in the complex time plane. We can choose  $z'$  to be  $z^+$  infinitesimally after  $z$ , and by choosing the arguments of the inverse temperature contour to be  $z_a = z$  and  $z'_a = z' = z^+$ , and thus:

$$\langle O \rangle(z) = \frac{1}{i} \frac{\text{Tr} \left[ e^{-i \int_{\gamma^M} d\bar{z} \hat{H}^M} \mathcal{T} \left\{ e^{-i \int_{\gamma} d\bar{z} \hat{H}(\bar{z})} \hat{O}(z) \right\} \right]}{\text{Tr} \left[ e^{-i \int_{\gamma^M} d\bar{z} \hat{H}^M} \mathcal{T} \left\{ e^{-i \int_{\gamma} d\bar{z} \hat{H}(\bar{z})} \right\} \right]} \quad (\text{H.20})$$

If we now incorporate  $\gamma^M$  to the full continuous path  $\gamma$  in the Keldysh contour the result simplifies to:

$$\langle O \rangle(z) = \frac{1}{i} \frac{\text{Tr} \left[ \mathcal{T} \left\{ e^{-i \int_{\gamma} dz \hat{H}(\bar{z})} \hat{O}(z) \right\} \right]}{\text{Tr} \left[ \mathcal{T} \left\{ e^{-i \int_{\gamma} dz \hat{H}(\bar{z})} \right\} \right]} \quad (\text{H.21})$$

if restricted to the real-time ensemble average of one-body operators, since any one-body operator in second quantization can be written as:

$$\hat{O} = \sum_{ij} O_{ij} \hat{d}_i^\dagger \hat{d}_j \quad (\text{H.22})$$

taking into account the definition (1.30) for the lesser Green's function, we get:

$$\langle O \rangle(t) = \pm i \sum_{ij} O_{ij} G_{ji}^<(t, t) \quad (\text{H.23})$$

where  $\pm$  stands for bosons/fermions.

In steady-state and from the definition of the steady-state single particle density matrix operator (H.16), the ensemble average of operator  $\hat{O}$ :

$$\langle O \rangle = \text{Tr} \left[ \hat{\rho} \hat{O} \right] \quad (\text{H.24})$$

Part IV

SUMMARY AND OUTLOOK - RESUMEN Y  
PERSPECTIVAS

## CONCLUSIONS

---

In chapters 1, 2 and 3, we present the theory and an actual numerical implementation for the evaluation of thermodynamic forces in an out of equilibrium situation. Our purpose has been to bridge the gap between existing theoretical work and a practical use of these forces for, e.g., electromigration problems (Sadeghi et al., 2015; Sabater, Untiedt, & van Ruitenbeek, 2017) and STM atomic manipulation (González-Herrero et al., 2016), while explaining several important conceptual and numerical issues that arise along the way. As we have shown here, the numerical evaluation of the derivatives of the corresponding free energy becomes non-trivial since non-equilibrium Green's functions are involved in the evaluation of such free energy. We have implemented this at the Hartree-Fock (HF) and DFT levels using LCAO where the orbitals are described by Gaussian functions. Several results for model systems illustrating the need, validity, and prospective use of our implementation have been presented. We have focused here on electrostatic effects, while intentionally leaving out of the discussion Joule heating effects or dissipation of energy by coupling to phonons (Engelund, Brandbyge, & Jauho, 2009, 4; Lü, Christensen, Wang, Hedegård, & Brandbyge, 2015, 9), which may also play a role in actual experiments.

Chapters 4, 5 and 6 present the collaborations with experimentalists in which the methods previously described have been applied during the development of the thesis.

## CONCLUSIONES

---

En los capítulos 1, 2 y 3, presentamos la teoría y una implementación numérica efectiva de la evaluación de las fuerzas termodinámicas en una situación fuera de equilibrio electroquímico. Nuestro propósito ha sido cerrar la brecha entre el trabajo teórico existente y el uso práctico de estas fuerzas para, por ejemplo, problemas de electromigración (Sadeghi u. a., 2015; Sabater u. a., 2017) y de manipulación atómica por medio de STM (González-Herrero u. a., 2016), al tiempo que explicamos varios problemas conceptuales y numéricos importantes surgidos en el camino. Como hemos mostrado aquí, la evaluación numérica de las derivadas de la energía libre correspondiente se vuelve no trivial, ya que las funciones de Green fuera del equilibrio están involucradas en la evaluación de dicha energía libre. Hemos implementado esto a nivel Hartree-Fock (HF) y DFT usando LCAO, método en el cual los orbitales son descritos por funciones gaussianas. Se han presentado varios resultados para sistemas modelo que ilustran la necesidad, validez y uso prospectivo de nuestra implementación. Nos hemos centrado aquí en los efectos electrostáticos, mientras que dejamos deliberadamente fuera de la discusión los efectos de calentamiento de Joule o la disipación de energía mediante el acoplamiento de fonones (Engelund u. a., 2009, 4; Lü u. a., 2015, 9), que también pueden desempeñar un papel en experimentos reales.

Los capítulos 4, 5 and 6 presentan las colaboraciones con físicos experimentales en las que los métodos anteriormente descritos han sido aplicados durante el desarrollo de la tesis.

Part V

BIBLIOGRAPHY

## BIBLIOGRAPHY

---

- Agrait, N. [N.], Rodrigo, J. G., Rubio, G., Sirvent, C., & Vieira, S. (1994). Plastic deformation in atomic size contacts. *Thin Solid Films*, 253, 199–203. doi:[10.1016/0040-6090\(94\)90320-4](https://doi.org/10.1016/0040-6090(94)90320-4)
- Agrait, N., Rodrigo, J. G., & Vieira, S. (1993). Conductance steps and quantization in atomic-size contacts. *Physical Review B*, 47(18). doi:[10.1103/PhysRevB.47.12345](https://doi.org/10.1103/PhysRevB.47.12345)
- Agrait, N. [Nicolás], Yeyati, A. L., & van Ruitenbeek, J. M. (2003). Quantum properties of atomic-sized conductors. 377(2-3), 81–279. doi:[10.1016/S0370-1573\(02\)00633-6](https://doi.org/10.1016/S0370-1573(02)00633-6). arXiv: [0208239](https://arxiv.org/abs/0208239) [cond-mat]
- Akimenko, A. & Yanson, I. (1980). Point contact spectroscopy of magnons in metals. *Jetp Letters*, 31(4), 191–194.
- Arenhold, K., Surnev, S., Bonzel, H. P., & Wynblatt, P. (1999). Step energetics of Pb(111) vicinal surfaces from facet shape. *Surface Science*, 424, 271–277. doi:[10.1016/S0039-6028\(99\)00074-6](https://doi.org/10.1016/S0039-6028(99)00074-6)
- Bauer, G. E. W., Saitph, E., & van Wees, B. J. (2012). Spin caloritronics. *Nat. Mater.* 11, 391–399.
- Becker, M. & Berndt, R. [Richard]. (2010). Conductance of atom-sized Pb contacts. *New Journal of Physics*, 12, 113010. doi:[10.1088/1367-2630/12/11/113010](https://doi.org/10.1088/1367-2630/12/11/113010)
- Berg, O. (2014). *Elektrischer transport durch nanokontakte von selten-erd-metallen* (Doctoral dissertation, Karlsruher Institut für Technologie (KIT)).
- Bergner, A., Dolg, M., Küchle, W., Stoll, H., & Preuß, H. (1993). Ab initio energy-adjusted pseudopotentials for elements of groups 13-17. *Molecular Physics*, 80(6), 1431–1441. doi:[10.1080/00268979300103121](https://doi.org/10.1080/00268979300103121)
- Berndt, R. [R.], Kröger, J., Néel, N., & Schull, G. (2010). Controlled single atom and single molecule contacts. *Physical Chemistry Chemical Physics*, 12, 1022–1032. doi:[10.1039/b908672m](https://doi.org/10.1039/b908672m)
- Binning, G., Rohrer, H., Gerber, C., & Weibel, E. (1982). Surface studies by scanning tunneling microscopy. *Physical Review Letters*. doi:[10.1103/PhysRevLett.49.57](https://doi.org/10.1103/PhysRevLett.49.57)
- Bovensiepen, U. (2007). Coherent and incoherent excitations of the Gd(0001) surface on ultrafast timescales. *Journal of Physics Condensed Matter*, 19(083201). doi:[10.1088/0953-8984/19/8/083201](https://doi.org/10.1088/0953-8984/19/8/083201)
- Brand, C., Pfnür, H., Landolt, G., Muff, S., Dil, J. H., Das, T., & Tegenkamp, C. (2015). Observation of correlated spin-orbit order in a strongly anisotropic quantum wire system. *Nature Communications*, 6, 8118. doi:[10.1038/ncomms9118](https://doi.org/10.1038/ncomms9118). arXiv: [1507.06152](https://arxiv.org/abs/1507.06152)
- Bultmark, F., Cricchio, F., Grånäs, O., & Nordström, L. (2009). Multipole decomposition of LDA+U energy and its application to actinide compounds. *Physical Review B - Condensed Matter and Materials Physics*, 80(3), 035121. doi:[10.1103/PhysRevB.80.035121](https://doi.org/10.1103/PhysRevB.80.035121). arXiv: [0904.0742](https://arxiv.org/abs/0904.0742)
- C. Santos, W. N. & Eyert, V. (2004). Ferromagnetism and temperature-dependent electronic structure of hcp gadolinium. *Phys. Rev. B*, 69(214412).

- Calvo, M. R. [M. R.], Jacob, D., & Untiedt, C. (2012). Analysis of the Kondo effect in ferromagnetic atomic-sized contacts. *Physical Review B - Condensed Matter and Materials Physics*, 86, 075447. doi:[10.1103/PhysRevB.86.075447](https://doi.org/10.1103/PhysRevB.86.075447). arXiv: [1208.5257](https://arxiv.org/abs/1208.5257)
- Calvo, M. R. [M. Reyes], Fernández-Rossier, J., Palacios, J. J., Jacob, D., Natelson, D., & Untiedt, C. (2009). The Kondo effect in ferromagnetic atomic contacts. *Nature*, 458(7242), 1150. doi:[10.1038/nature07878](https://doi.org/10.1038/nature07878). arXiv: [0906.3135](https://arxiv.org/abs/0906.3135)
- Caroli, C., Combescot, R., Nozieres, P., & Saint-James, D. (1971). Direct calculation of the tunneling current. *Journal of Physics C: Solid State Physics*, 4(8), 916. doi:[10.1088/0022-3719/4/8/018](https://doi.org/10.1088/0022-3719/4/8/018). arXiv: [0022-3719/4/8/018](https://arxiv.org/abs/0022-3719/4/8/018) [[10.1088](https://arxiv.org/abs/10.1088)]
- Cuevas, J. C., Levy Yeyati, A., Martín-Rodero, A., Rubio Bollinger, G., Untiedt, C., & Agraït, N. (1998). Evolution of conducting channels in metallic atomic contacts under elastic deformation. *Physical Review Letters*, 81(14), 2990–2993. doi:[10.1103/PhysRevLett.81.2990](https://doi.org/10.1103/PhysRevLett.81.2990)
- Datta, S. (1995). *Electronic transport in mesoscopic systems*. Cambridge university press. doi:[10.1063/1.2807624](https://doi.org/10.1063/1.2807624). arXiv: [0607219](https://arxiv.org/abs/0607219) [[cond-mat](https://arxiv.org/abs/cond-mat)]
- Datta, S. (2005). *Quantum transport: Atom to transistor*. Cambridge university press. doi:[10.1017/CBO9781139164313](https://doi.org/10.1017/CBO9781139164313). arXiv: [arXiv:1011.1669v3](https://arxiv.org/abs/1011.1669v3)
- den Brom, H., Yanson, A., & Ruitenbeek, J. (1998a). Characterization of individual conductance steps in metallic quantum point contacts. *Physica B: Condensed Matter*, 252, 69–75. doi:[10.1016/S0921-4526\(97\)00996-4](https://doi.org/10.1016/S0921-4526(97)00996-4)
- den Brom, H., Yanson, A., & Ruitenbeek, J. (1998b). Characterization of individual conductance steps in metallic quantum point contacts. *Physica B: Condensed Matter*, 252(1-2), 69–75. doi:[10.1016/S0921-4526\(97\)00996-4](https://doi.org/10.1016/S0921-4526(97)00996-4)
- Dolg, M., Stoll, H., Preuss, H., & Pitzer, R. M. (1993). Relativistic and correlation effects for element 105 (hahnium, ha): a comparative study of m and mo (m=nb, ta, ha) using energy-adjusted ab initio pseudopotentials. *The Journal of Physical Chemistry*, 97(22), 5852–5859.
- Dovesi, R., Orlando, R., Erba, A., Zicovich-Wilson, C. M., Civalieri, B., Casassa, S., ... Kirtman, B. (2014). CRYSTAL14: A program for the ab initio investigation of crystalline solids. *International Journal of Quantum Chemistry*, 114(19), 1287–1317. doi:[10.1002/qua.24658](https://doi.org/10.1002/qua.24658)
- Duan, C. G., Sabirianov, R. F., Mei, W. N., Dowben, P. A., Jaswal, S. S., & Tsymbal, E. Y. (2007). Electronic, magnetic and transport properties of rare-earth mononictides. *Journal of Physics Condensed Matter*, 19(315220). doi:[10.1088/0953-8984/19/31/315220](https://doi.org/10.1088/0953-8984/19/31/315220)
- Dubi, Y. & Di Ventra, M. (2011). Colloquium: Heat flow and thermoelectricity in atomic and molecular junctions. *Reviews of Modern Physics*, 83, 131–155. doi:[10.1103/RevModPhys.83.131](https://doi.org/10.1103/RevModPhys.83.131). arXiv: [0910.0425](https://arxiv.org/abs/0910.0425)
- Dutt, P., Koch, J., Han, J., & Le Hur, K. (2011). Effective equilibrium theory of nonequilibrium quantum transport. *Annals of Physics*, 326(12), 2963–2999. doi:[10.1016/j.aop.2011.07.001](https://doi.org/10.1016/j.aop.2011.07.001). arXiv: [1101.1526](https://arxiv.org/abs/1101.1526)
- Engelund, M., Brandbyge, M., & Jauho, A. P. (2009, July). Atomistic theory for the damping of vibrational modes in monoatomic gold chains. *Phys. Rev. B*, 80, 045427. doi:[10.1103/PhysRevB.80.045427](https://doi.org/10.1103/PhysRevB.80.045427)

- Evangelii, C., Matt, M., Rincón-García, L., Pauly, F., Nielaba, P., Rubio-Bollinger, G., ... Agraït, N. (2015). Quantum thermopower of metallic atomic-size contacts at room temperature. *Nano Letters*, *15*, 1006–1011. doi:[10.1021/nl503853v](https://doi.org/10.1021/nl503853v)
- Feynman, R. P. (1964). *Feynman lectures on physics. Volume 2: Mainly electromagnetism and matter*. doi:[10.1119/1.1972241](https://doi.org/10.1119/1.1972241)
- Flores, F., Echenique, P. M., & Ritchie, R. H. (1986). Energy dissipation processes in scanning tunneling microscopy. *Physical Review B*. doi:[10.1103/PhysRevB.34.2899](https://doi.org/10.1103/PhysRevB.34.2899)
- Franke, K. J., Schulze, G., & Pascual, J. I. (2011). Competition of superconducting phenomena and Kondo screening at the nanoscale. *Science*, *332*, 940–944. doi:[10.1126/science.1202204](https://doi.org/10.1126/science.1202204)
- Frisch, M. J., Trucks, G. W., Schlegel, H. B. [H. B.], Scuseria, G. E. [G. E.], Robb, M. A., Cheeseman, J. R., ... Fox, D. J. (2009). Gaussian 09 Revision E.01. doi:[10.1007/s13524-014-0367-9](https://doi.org/10.1007/s13524-014-0367-9). arXiv: [111](https://arxiv.org/abs/111)
- Frisch, M. J., Trucks, G. W., Schlegel, H. B. [H. B.], Scuseria, G. E. [G. E.], Robb, M. A., Cheeseman, J. R., ... Fox, D. J. (2009). *Gaussian Inc. Wallingford CT*.
- Frisch, M., Trucks, G., Schlegel, H. B. [Hs B], Scuseria, G., Robb, M., Cheeseman, J., ... Petersson, G. e., et al. (2009). Gaussian 09. Gaussian, Inc. Wallingford, CT.
- Gimzewski, J. K. & Möller, R. (1987). Transition from the tunneling regime to point contact studied using scanning tunneling microscopy. *Phys. Rev. B*, *36*(1284).
- González-Herrero, H., Gómez-Rodríguez, J., Mallet, P., Moaied, M., Palacios, J., Salgado, C., ... Brihuega, I. (2016). Atomic-scale control of graphene magnetism by using hydrogen atoms. *Science*, *352*(6284). doi:[10.1126/science.aad8038](https://doi.org/10.1126/science.aad8038)
- Goodings, D. A. (1962). Magnitude of exchange interactions in gadolinium. *Physical Review*, *127*, 5. doi:[10.1103/PhysRev.127.1532](https://doi.org/10.1103/PhysRev.127.1532)
- Gordon, M. S., Binkley, J. S., Pople, J. A., Pietro, W. J., & Hehre, W. J. (1982). Self-Consistent Molecular-Orbital Methods. 22. Small Split-Valence Basis Sets for Second-Row Elements. *Journal of the American Chemical Society*. doi:[10.1021/ja00374a017](https://doi.org/10.1021/ja00374a017)
- Gschneidner, K. A. & Eyring, L. (1978). *Handbook on the physics and chemistry of rare earth*.
- Gschneidner Jr, K. A., Pecharsky, V., & Tsokol, A. (2005). Recent developments in magnetocaloric materials. *Reports on progress in physics*, *68*(6), 1479.
- H. E. Nigh, S. L. & Spedding, F. H. (1963). Magnetization and electrical resistivity of gadolinium single crystals. *Phys. Rev.* *132*, 3.
- Häfner, M., Konrad, P., Pauly, F., Cuevas, J. C., & Scheer, E. (2004). Conduction channels of one-atom zinc contacts. *Physical Review B - Condensed Matter and Materials Physics*, *70*(24), 241404. doi:[10.1103/PhysRevB.70.241404](https://doi.org/10.1103/PhysRevB.70.241404). arXiv: [0407207](https://arxiv.org/abs/0407207) [cond-mat]
- Halbritter, A., Csonka, S., Kolesnychenko, O. Y., Mihály, G., Shklyarevskii, O. I., Shklyarevskii, O. I., & van Kempen, H. (2002). Connective neck evolution and conductance steps in hot point contacts. *Physical Review B - Condensed Matter and Materials Physics*, *65*, 045413. doi:[10.1103/PhysRevB.65.045413](https://doi.org/10.1103/PhysRevB.65.045413). arXiv: [0112167](https://arxiv.org/abs/0112167) [cond-mat]

- Han, J. E. [J. E.]. (2007). Mapping of strongly correlated steady-state nonequilibrium system to an effective equilibrium. *Physical Review B - Condensed Matter and Materials Physics*, 75(12), 125122. doi:[10.1103/PhysRevB.75.125122](https://doi.org/10.1103/PhysRevB.75.125122). arXiv: [0604583v1](https://arxiv.org/abs/0604583v1) [cond-mat]
- Han, J. E. [J. E.] & Heary, R. J. (2007). Imaginary-time formulation of steady-state nonequilibrium: Application to strongly correlated transport. *Physical Review Letters*, 99(23), 236808. doi:[10.1103/PhysRevLett.99.236808](https://doi.org/10.1103/PhysRevLett.99.236808). arXiv: [0704.3198](https://arxiv.org/abs/0704.3198)
- Han, J. E. [Jong E.], Dirks, A., & Pruschke, T. (2012). Imaginary-time quantum many-body theory out of equilibrium: Formal equivalence to Keldysh real-time theory and calculation of static properties. *Physical Review B - Condensed Matter and Materials Physics*, 86(15), 155130. doi:[10.1103/PhysRevB.86.155130](https://doi.org/10.1103/PhysRevB.86.155130). arXiv: [1205.1816](https://arxiv.org/abs/1205.1816)
- Han, J. E. [Jong E.] & Li, J. (2013). Energy dissipation in a dc-field-driven electron lattice coupled to fermion baths. *Physical Review B - Condensed Matter and Materials Physics*, 88(7), 075113. doi:[10.1103/PhysRevB.88.075113](https://doi.org/10.1103/PhysRevB.88.075113)
- Hershfield, S. (1993). Reformulation of steady state nonequilibrium quantum statistical mechanics. *Physical Review Letters*, 70(14), 2134. doi:[10.1103/PhysRevLett.70.2134](https://doi.org/10.1103/PhysRevLett.70.2134)
- Heyd, J. & Scuseria, G. E. [Gustavo E]. (2004). Efficient hybrid density functional calculations in solids: assessment of the heyd–scuseria–ernzerhof screened coulomb hybrid functional. *The Journal of chemical physics*, 121(3), 1187–1192.
- Horcas, I., Fernández, R., Gómez-Rodríguez, J. M., Colchero, J., Gómez-Herrero, J., & Baro, A. M. (2007). WSXM: A software for scanning probe microscopy and a tool for nanotechnology. *Review of Scientific Instruments*, 78, 13705. doi:[10.1063/1.2432410](https://doi.org/10.1063/1.2432410)
- Hyltdgaard, P. [P.]. (2012). Nonequilibrium thermodynamics of interacting tunneling transport: Variational grand potential, density functional formulation and nature of steady-state forces. *Journal of Physics Condensed Matter*, 24(42), 667–673. doi:[10.1088/0953-8984/24/42/424219](https://doi.org/10.1088/0953-8984/24/42/424219). arXiv: [1108.4536](https://arxiv.org/abs/1108.4536)
- Hyltdgaard, P. [Per]. (2008). Density-functional theory of nonequilibrium tunneling. *Physical Review B - Condensed Matter and Materials Physics*, 78(16), 165109. doi:[10.1103/PhysRevB.78.165109](https://doi.org/10.1103/PhysRevB.78.165109). arXiv: [arXiv:0807.4555v2](https://arxiv.org/abs/0807.4555v2)
- I. Turek, G. B., J. Kudrnovský & Blügel, S. (2003). Ab initio theory of exchange interactions and the curie temperature of bulk gd. *J. Phys.: Condens. Matter*, 15, 2771–2782.
- Jacob, D. [D.] & Palacios, J. J. [J. J.]. (2011). Critical comparison of electrode models in density functional theory based quantum transport calculations. *Journal of Chemical Physics*, 134, 044118. doi:[10.1063/1.3526044](https://doi.org/10.1063/1.3526044). arXiv: [1008.4538](https://arxiv.org/abs/1008.4538)
- Jacob, D. [D] & Palacios, J. J. [Juan José]. (2011). Critical comparison of electrode models in density functional theory based quantum transport calculations. *The Journal of chemical physics*, 134(4), 044118.
- Jacob, D. [David] & Palacios, J. J. [J. J.]. (2006). Orbital eigenchannel analysis for ab initio quantum transport calculations. *Physical Review B - Condensed Matter and Materials Physics*, 73(7), 075429. doi:[10.1103/PhysRevB.73.075429](https://doi.org/10.1103/PhysRevB.73.075429). arXiv: [0510696](https://arxiv.org/abs/0510696) [cond-mat]

- Jacobi, K. (1988). Photoemission from Ar, Kr, and Xe on Pb(111). *Physical Review B*. doi:[10.1103/PhysRevB.38.5869](https://doi.org/10.1103/PhysRevB.38.5869)
- Jammalamadaka, S. N., Kuntz, S., Berg, O., Kittler, W., Kannan, U. M., Chelvane, J. A., & Sürgers, C. (2015). Remote control of magnetostriction-based nanocontacts at room temperature. *Scientific Reports*, 5, 13621. doi:[10.1038/srep13621](https://doi.org/10.1038/srep13621)
- Kaupp, M., Schleyer, P. V., Stoll, H., & Preuss, H. (1991). Pseudopotential approaches to Ca, Sr, and Ba hydrides. Why are some alkaline earth MX<sub>2</sub> compounds bent? *The Journal of Chemical Physics*, 94(2), 1360–1366. doi:[10.1063/1.459993](https://doi.org/10.1063/1.459993)
- Kenny, J. P., Janssen, C. L., Valeev, E. F., & Windus, T. L. (2008). Components for integral evaluation in quantum chemistry. *Journal of Computational Chemistry*. doi:[10.1002/jcc.20815](https://doi.org/10.1002/jcc.20815)
- Kim, H. & Hasegawa, Y. (2015). Site-Dependent Evolution of Electrical Conductance from Tunneling to Atomic Point Contact. *Physical Review Letters*, 114, 206801. doi:[10.1103/PhysRevLett.114.206801](https://doi.org/10.1103/PhysRevLett.114.206801). arXiv: [0206469](https://arxiv.org/abs/0206469) [astro-ph]
- Kröger, J., Jensen, H., & Berndt, R. (2007). Conductance of tip-surface and tip-atom junctions on Au(111) explored by a scanning tunnelling microscope. *New Journal of Physics*, 9, 153. doi:[10.1088/1367-2630/9/5/153](https://doi.org/10.1088/1367-2630/9/5/153)
- Kröger, J., Néel, N., & Limot, L. (2008). Contact to single atoms and molecules with the tip of a scanning tunnelling microscope. *Journal of Physics Condensed Matter*, 20, 223001. doi:[10.1088/0953-8984/20/22/223001](https://doi.org/10.1088/0953-8984/20/22/223001)
- Kröger, J., Néel, N., Sperl, A., Wang, Y. F., & Berndt, R. (2009). Single-atom contacts with a scanning tunnelling microscope. *New Journal of Physics*, 11, 125006. doi:[10.1088/1367-2630/11/12/125006](https://doi.org/10.1088/1367-2630/11/12/125006)
- Kuipers, L. & Frenken, J. W. (1993). Jump to contact, neck formation, and surface melting in the scanning tunneling microscope. *Physical Review Letters*, 70, 3907–3910. doi:[10.1103/PhysRevLett.70.3907](https://doi.org/10.1103/PhysRevLett.70.3907)
- Kurnosikov, O., Adam, O. A. O., Swagten, H. J. M., De Jonge, W. J. M., & Koopmans, B. (2008). Probing quantum wells induced above a subsurface nanocavity in copper. *Physical Review B - Condensed Matter and Materials Physics*, 77, 125429. doi:[10.1016/j.molliq.2014.05.013](https://doi.org/10.1016/j.molliq.2014.05.013)
- Kurz, P., Bihlmayer, G., & Blügel, S. (2002). Magnetism and electronic structure of hcp Gd and the Gd(0001) surface. *Journal of Physics Condensed Matter*, 14, 6353–6371. doi:[10.1088/0953-8984/14/25/305](https://doi.org/10.1088/0953-8984/14/25/305)
- Lee, W., Kim, K., Jeong, W., Zotti, L. A., Pauly, F., Cuevas, J. C., & Reddy, P. (2013). Heat dissipation in atomic-scale junctions. *Nature*, 498, 209–212. doi:[10.1038/nature12183](https://doi.org/10.1038/nature12183). arXiv: [1307.8313](https://arxiv.org/abs/1307.8313)
- Lehtola, J., Hakala, M., Sakko, A., & Hämäläinen, K. (2012). ERKALE-A flexible program package for X-ray properties of atoms and molecules. *Journal of Computational Chemistry*. doi:[10.1002/jcc.22987](https://doi.org/10.1002/jcc.22987)
- Leinweber, G., Barry, D., Trbovich, M., Burke, J., Drindak, N., Knox, H., ... Severniyak, L. (2006). Neutron capture and total cross-section measurements and resonance parameters of gadolinium. *Nucl. Sci. Eng.* 154(3), 261–279. doi:[10.13182/NSE05-64](https://doi.org/10.13182/NSE05-64)
- Li, S. C., Han, Y., Jia, J. F., Xue, Q. K., & Liu, F. (2006). Determination of the Ehrlich-Schwoebel barrier in epitaxial growth of thin films. *Physical Review B -*

*Condensed Matter and Materials Physics*, 74, 195428. doi:[10.1103/PhysRevB.74.195428](https://doi.org/10.1103/PhysRevB.74.195428)

- Limot, L., Kröger, J., Berndt, R., Garcia-Lekue, A., & Hofer, W. A. (n.d.). Atom transfer and single-atom contacts. *Phys. Rev. Lett.* 94(12), 126102. doi:[10.1103/PhysRevLett.94.126102](https://doi.org/10.1103/PhysRevLett.94.126102). arXiv: [0412249](https://arxiv.org/abs/0412249) [cond-mat]
- Louis, E., Vergés, J., Palacios, J., Pérez-Jiménez, A., & SanFabián, E. (2003). Implementing the keldysh formalism into ab initio methods for the calculation of quantum transport: application to metallic nanocontacts. *Physical Review B*, 67(15), 155321.
- Lü, J.-T., Christensen, R. B., Wang, J.-S., Hedegård, P., & Brandbyge, M. (2015, March). Current-induced forces and hot spots in biased nanojunctions. *Phys. Rev. Lett.* 114, 096801. doi:[10.1103/PhysRevLett.114.096801](https://doi.org/10.1103/PhysRevLett.114.096801)
- Madhavan, V., Chen, W., Jamneala, T., Crommie, M. F., & Wingreen, N. S. (1998). Tunneling into a single magnetic atom: Spectroscopic evidence of the Kondo resonance. *Science*, 280, 567. doi:[10.1126/science.280.5363.567](https://doi.org/10.1126/science.280.5363.567). arXiv: [arXiv: 1312.6184v5](https://arxiv.org/abs/1312.6184v5)
- Marques, M. A., Oliveira, M. J., & Burnus, T. (2012). Libxc: A library of exchange and correlation functionals for density functional theory. *Computer Physics Communications*. doi:[10.1016/j.cpc.2012.05.007](https://doi.org/10.1016/j.cpc.2012.05.007). arXiv: [1203.1739](https://arxiv.org/abs/1203.1739)
- Moreland, J. & Ekin, J. W. (1985). Electron tunneling experiments using nb-sn “break” junctions. *J. Appl. Phys.* 58(3888).
- Müller, M. [M], Salgado, C., Néel, N., Palacios, J., & Kröger, J. (2016). Plasticity of single-atom pb junctions. *Physical Review B*, 93(23), 235402.
- Müller, M. [M.], Salgado, C., Néel, N., Palacios, J., & Kröger, J. (2016). Plasticity of single-atom Pb junctions. *Physical Review B*, 93(23). doi:[10.1103/PhysRevB.93.235402](https://doi.org/10.1103/PhysRevB.93.235402)
- Müller, M. [Marc], Montbrun, R., Marz, M., Fritsch, V., Sürgers, C., & Löhneysen, H. V. (2010). Switching the conductance of Dy nanocontacts by magnetostriction. *Nano Letters*, 11(2), 574–578. doi:[10.1021/nl103574m](https://doi.org/10.1021/nl103574m)
- Myöhänen, P., Stan, A., Stefanucci, G., & Van Leeuwen, R. (2009). Kadanoff-Baym approach to quantum transport through interacting nanoscale systems: From the transient to the steady-state regime. *Physical Review B - Condensed Matter and Materials Physics*, 80(11), 115107. doi:[10.1103/PhysRevB.80.115107](https://doi.org/10.1103/PhysRevB.80.115107). arXiv: [0906.2136](https://arxiv.org/abs/0906.2136)
- N. Agraït, A. L. Y. & van Ruitenbeek, J. M. (2003). Quantum properties of atomic-sized conductors. *Phys. Rep.* 377, 81–279. doi:[10.1016/S0370-1573\(02\)00633-6](https://doi.org/10.1016/S0370-1573(02)00633-6). arXiv: [0208239](https://arxiv.org/abs/0208239) [cond-mat]
- Naidyuk, Y. G. & Yanson, I. K. (2008). Point-contact spectroscopy. *arXiv:physics*, [0312016v1](https://arxiv.org/abs/0312016v1).
- Néel, N., Kröger, J., & Berndt, R. (2011). Two-level conductance fluctuations of a single-molecule junction. *Nano Letters*, 11, 3593–3596. doi:[10.1021/nl201327c](https://doi.org/10.1021/nl201327c)
- Ness, H. (2014). Nonequilibrium density matrix in quantum open systems: Generalization for simultaneous heat and charge steady-state transport. *Physical Review E - Statistical, Nonlinear, and Soft Matter Physics*, 90(6), 062119. doi:[10.1103/PhysRevE.90.062119](https://doi.org/10.1103/PhysRevE.90.062119). arXiv: [1409.4982](https://arxiv.org/abs/1409.4982)

- Ness, H. (2017). Nonequilibrium thermodynamics and steady state density matrix for quantum open systems. *Entropy*, 19(4), 158. doi:[10.3390/e19040158](https://doi.org/10.3390/e19040158). arXiv: [1703.10531](https://arxiv.org/abs/1703.10531)
- Ohnishi, H., Kondo, Y., & Takayanagi, K. (1998). *Nature*, 395, 780–783.
- Olivera, B., Salgado, C., Lado, J., Karimi, A., Henkel, V., Scheer, E., ... Untiedt, C. (2017). Electronic transport in gadolinium atomic-size contacts. *Physical Review B*, 95(7). doi:[10.1103/PhysRevB.95.075409](https://doi.org/10.1103/PhysRevB.95.075409)
- Palacios, J. J. [J. J.], Pérez-Jiménez, A. J., Louis, E., SanFabián, E., & Vergés, J. A. (2002). First-principles approach to electrical transport in atomic-scale nanostructures. *Physical Review B - Condensed Matter and Materials Physics*, 66(3), 035322. doi:[10.1103/PhysRevB.66.035322](https://doi.org/10.1103/PhysRevB.66.035322). arXiv: [0202375](https://arxiv.org/abs/0202375) [cond-mat]
- Palacios, J. J. [J. J.], Pérez-Jiménez, A. J., Louis, E., & Vergés, J. A. (2001). Fullerene-based molecular nanobridges: A first-principles study. *Physical Review B - Condensed Matter and Materials Physics*, 64(11), 115411. doi:[10.1103/PhysRevB.64.115411](https://doi.org/10.1103/PhysRevB.64.115411). arXiv: [0101359](https://arxiv.org/abs/0101359) [cond-mat]
- Palacios, J. [JJ], Pérez-Jiménez, A., Louis, E., & Vergés, J. (2001). Fullerene-based molecular nanobridges: a first-principles study. *Physical Review B*, 64(11), 115411.
- Peng, C., Ayala, P. Y., Schlegel, H. B., & Frisch, M. J. (1996). Using redundant internal coordinates to optimize equilibrium geometries and transition states. *Journal of Computational Chemistry*. doi:[10.1002/\(SICI\)1096-987X\(19960115\)17:1<49::AID-JCC5>3.0.CO;2-0](https://doi.org/10.1002/(SICI)1096-987X(19960115)17:1<49::AID-JCC5>3.0.CO;2-0). arXiv: [CCC0192-86511961010049-08](https://arxiv.org/abs/CCC0192-86511961010049-08)
- Pernau, H. F., Pietsch, T., & Scheer, E. (2014). Magnetotransport in atomic-size bismuth contacts. *Journal of Physics Condensed Matter*, 26(47), 474203. doi:[10.1088/0953-8984/26/47/474203](https://doi.org/10.1088/0953-8984/26/47/474203)
- R. Ahuja, B. J., S. Auluck & Brooks, M. S. S. (1994). Electronic structure, magnetism, and fermi surfaces of gd and tb. *Phys. Rev. B*, 50(8).
- R. H. M. Smit, A. I. Y., C. Untiedt & van Ruitenbeek, J. M. (2001). Common origin for surface reconstruction and the formation of chains of metal atoms. *Phys. Rev. Lett.* 87, 266102.
- Rego, L. G., Rocha, A. R., Rodrigues, V., Ugarte, D., & Rego, L. G. (2003). Role of structural evolution in the quantum conductance behavior of gold nanowires during stretching. *Physical Review B - Condensed Matter and Materials Physics*. doi:[10.1103/PhysRevB.67.045412](https://doi.org/10.1103/PhysRevB.67.045412). arXiv: [0206412](https://arxiv.org/abs/0206412) [cond-mat]
- Rodrigo, J. G., Crespo, V., Suderow, H., Vieira, S., & Guinea, F. (2012). Topological superconducting state of lead nanowires in an external magnetic field. *Physical Review Letters*, 109, 237003. doi:[10.1103/PhysRevLett.109.237003](https://doi.org/10.1103/PhysRevLett.109.237003)
- Rodrigo, J. G., Suderow, H., Vieira, S., Bascones, E., & Guinea, F. (2004). Superconducting nanostructures fabricated with the scanning tunnelling microscope. *16*, R1151–R1182. doi:[10.1088/0953-8984/16/34/R01](https://doi.org/10.1088/0953-8984/16/34/R01). arXiv: [0410500](https://arxiv.org/abs/0410500) [cond-mat]
- Rodrigues, V., Fuhrer, T., & Ugarte, D. (2000). Signature of atomic structure in the quantum conductance of gold nanowires. *Physical Review Letters*, 85, 4124–4127. doi:[10.1103/PhysRevLett.85.4124](https://doi.org/10.1103/PhysRevLett.85.4124)
- Ross, R. B., Powers, J. M., Atashroo, T., Ermler, W. C., LaJohn, L. A., & Christiansen, P. A. (1990). Ab initio relativistic effective potentials with spin-orbit operators.

- IV. Cs through Rn. *The Journal of Chemical Physics*, 93, 6654. doi:[10.1063/1.458934](https://doi.org/10.1063/1.458934)
- Ruby, M., Heinrich, B. W., Pascual, J. I., & Franke, K. J. (2015). Experimental demonstration of a two-band superconducting state for lead using scanning tunneling spectroscopy. *Physical Review Letters*, 114, 157001. doi:[10.1103/PhysRevLett.114.157001](https://doi.org/10.1103/PhysRevLett.114.157001). arXiv: [1409.6638](https://arxiv.org/abs/1409.6638)
- Ruby, M., Pientka, F., Peng, Y., Von Oppen, F., Heinrich, B. W., & Franke, K. J. (2015). Tunneling Processes into Localized Subgap States in Superconductors. *Physical Review Letters*, 115, 087001. doi:[10.1103/PhysRevLett.115.087001](https://doi.org/10.1103/PhysRevLett.115.087001). arXiv: [1502.05048](https://arxiv.org/abs/1502.05048)
- Sabater, C., Gosálbez-Martínez, D., Fernández-Rossier, J., Rodrigo, J. G., Untiedt, C., & Palacios, J. J. (2013). Topologically protected quantum transport in locally exfoliated bismuth at room temperature. *Physical Review Letters*, 110(17), 176802. doi:[10.1103/PhysRevLett.110.176802](https://doi.org/10.1103/PhysRevLett.110.176802). arXiv: [1304.0934](https://arxiv.org/abs/1304.0934)
- Sabater, C., Untiedt, C., Palacios, J. J., & Caturla, M. J. (2012). Mechanical annealing of metallic electrodes at the atomic scale. *Physical Review Letters*. doi:[10.1103/PhysRevLett.108.205502](https://doi.org/10.1103/PhysRevLett.108.205502). arXiv: [1205.4612](https://arxiv.org/abs/1205.4612)
- Sabater, C., Untiedt, C., & van Ruitenbeek, J. (2017). *Beilstein J. of Nanotechnology*, 6, 2338–2344.
- Sadeghi, H., Mol, J. A., Lau, C. S., Briggs, G. A. D., Warner, J., & Lambert, C. J. (2015). Conductance enlargement in picoscale electroburnt graphene nanojunctions. *Proceedings of the National Academy of Sciences*, 112(9), 2658–2663. doi:[10.1073/pnas.1418632112](https://doi.org/10.1073/pnas.1418632112). eprint: <https://www.pnas.org/content/112/9/2658.full.pdf>
- Salgado, C. & Palacios, J. [J.J.]. (2019). Atomistic Evaluation of Thermodynamic Forces in Open Systems for Equilibrium and Non-Equilibrium Electron Quantum Transport. TO BE PUBLISHED.
- Sánchez-Portal, D., Untiedt, C., Soler, J. M., Sáenz, J. J., & Agraåt, N. (1997). Nanocontacts: Probing electronic structure under extreme uniaxial strains. *Physical Review Letters*, 79(21). doi:[10.1103/PhysRevLett.79.4198](https://doi.org/10.1103/PhysRevLett.79.4198)
- Sanvito, S. (2011). Molecular spintronics. *Chemical Society reviews*. doi:[10.1039/c1cs15047b](https://doi.org/10.1039/c1cs15047b). arXiv: [1102.4151](https://arxiv.org/abs/1102.4151)
- Scheer, E., Agraåt, N., Cuevas, J. C., Yeyati, A. L., Ludoph, B., Martín-Rodero, A., ... Urbina, C. (1998). *Nature*, 394, 154–157.
- Scheer, E., Joyez, P., Esteve, D., Urbina, C., & Devoret, M. H. (1997). Conduction Channel Transmissions of Atomic-Size Aluminum Contacts. *Physical Review Letters*, 78(18), 3535. doi:[10.1103/PhysRevLett.78.3535](https://doi.org/10.1103/PhysRevLett.78.3535)
- Schirm, C., Matt, M., Pauly, F., Cuevas, J. C., Nielaba, P., & Scheer, E. (2013). A current-driven single-atom memory. *Nature Nanotechnology*, 8, 645–648. doi:[10.1038/nnano.2013.170](https://doi.org/10.1038/nnano.2013.170)
- Schmid, M., Hebenstreit, W., Varga, P., & Crampin, S. (1996). Quantum wells and electron interference phenomena in Al due to subsurface noble gas bubbles. *Physical Review Letters*, 76(13), 2298. doi:[10.1103/PhysRevLett.76.2298](https://doi.org/10.1103/PhysRevLett.76.2298)
- Schull, G., Frederiksen, T., Arnau, A., Sánchez-Portal, D., & Berndt, R. (2011). *Nat. Nanotechnol.* 6, 23–27.

- Sklyadneva, I. Y., Heid, R., Bohnen, K. P., Echenique, P. M., & Chulkov, E. V. (2012). Surface phonons on Pb(111). *Journal of Physics Condensed Matter*, 24, 104004. doi:[10.1088/0953-8984/24/10/104004](https://doi.org/10.1088/0953-8984/24/10/104004)
- Sperl, A., Kröger, J., & Berndt, R. (2010). Direct observation of conductance fluctuations of a single-atom tunneling contact. *Physical Review B - Condensed Matter and Materials Physics*, 81, 035406. doi:[10.1103/PhysRevB.81.035406](https://doi.org/10.1103/PhysRevB.81.035406)
- Stefanucci, G. & Almladh, C. O. (2004). Time-dependent partition-free approach in resonant tunneling systems. *Physical Review B - Condensed Matter and Materials Physics*, 69(19), 195318. doi:[10.1103/PhysRevB.69.195318](https://doi.org/10.1103/PhysRevB.69.195318). arXiv: [0310084](https://arxiv.org/abs/0310084) [cond-mat]
- Stefanucci, G. & Van Leeuwen, R. (2010). *Nonequilibrium many-body theory of quantum systems: A modern introduction*. doi:[10.1017/CBO9781139023979](https://doi.org/10.1017/CBO9781139023979)
- Temmerman, W. M. & Sterne, P. A. (1990). The band model for the ground state properties of gadolinium metal. *J. Phys.: Condens. Matter*, 2, 5529–5538.
- Trouwborst, M. L., Huisman, E. H., Bakker, F. L., Van Der Molen, S. J., & Van Wees, B. J. (2008). Single atom adhesion in optimized gold nanojunctions. *Physical Review Letters*, 100(17), 175502. doi:[10.1103/PhysRevLett.100.175502](https://doi.org/10.1103/PhysRevLett.100.175502). arXiv: [0802.3814](https://arxiv.org/abs/0802.3814)
- Untiedt, C., Rubio, G., Vieira, S., & Agraït, N. (1997). Fabrication and characterization of metallic nanowires. *Physical Review B - Condensed Matter and Materials Physics*. doi:[10.1103/PhysRevB.56.2154](https://doi.org/10.1103/PhysRevB.56.2154)
- Van Ruitenbeek, J. M., Alvarez, A., Piñeyro, I., Grahmann, C., Joyez, P., Devoret, M. H., ... Urbina, C. (1996). Adjustable nanofabricated atomic size contacts. *Review of Scientific Instruments*. doi:[10.1063/1.1146558](https://doi.org/10.1063/1.1146558)
- Vreven, T. [Thom], Morokuma, K., Farkas, Ö., Schlegel, H. B., & Frisch, M. J. (2003). Geometry optimization with QM/MM, ONIOM, and other combined methods. I. Microiterations and constraints. *Journal of Computational Chemistry*, 24(6), 760–769. doi:[10.1002/jcc.10156](https://doi.org/10.1002/jcc.10156)
- Wadt, W. R. & Hay, P. J. (1985). *Ab initio* effective core potentials for molecular calculations. Potentials for main group elements Na to Bi. *The Journal of Chemical Physics*, 82, 284. doi:[10.1063/1.448800](https://doi.org/10.1063/1.448800)
- Wang, Y. F., Kröger, J., Berndt, R., Vázquez, H., Brandbyge, M., & Paulsson, M. (2010). *Phys. Rev. Lett.* 104, 176802.
- Xie, F. Q., Hüser, F., Pauly, F., Obermair, C., Schön, G., & Schimmel, T. (2010). Conductance of atomic-scale Pb contacts in an electrochemical environment. *Physical Review B - Condensed Matter and Materials Physics*, 82, 075417. doi:[10.1103/PhysRevB.82.075417](https://doi.org/10.1103/PhysRevB.82.075417). arXiv: [arXiv:1002.4291v1](https://arxiv.org/abs/1002.4291v1)
- Xue, Y., Datta, S., & Ratner, M. A. (2002). First-principles based matrix Green's function approach to molecular electronic devices: General formalism. *Chemical Physics*, 281(2-3), 151–170. doi:[10.1016/S0301-0104\(02\)00446-9](https://doi.org/10.1016/S0301-0104(02)00446-9). arXiv: [0112136](https://arxiv.org/abs/0112136) [cond-mat]
- Yanson, A. I. [A. I.], Bollinger, G. R., van den Brom, H. E., Agraït, N., & van Ruitenbeek, J. M. (1998). *Nature*, 395, 783–785.
- Yanson, A. I. [A. I.], Rubio Bollinger, G., Van Den Brom, H. E., Agraït, N., & Van Ruitenbeek, J. M. (1998). Formation and manipulation of a metallic wire of sin-

gle gold atoms. *Nature*, 395(6704), 783. doi:[10.1038/27405](https://doi.org/10.1038/27405). arXiv: [9811093](https://arxiv.org/abs/9811093)  
[ [cond-mat](#) ]

Yanson, A. I. [A. I.] & van Ruitenbeek, J. M. (1997). Do histograms constitute a proof for conductance quantization? *Phys. Rev. Letters*, 79(11).

Yanson, A. I. [Alexei Igorevich]. (2001). *Atomic chains and electronic shells: quantum mechanisms for the formation of nanowires* (Doctoral dissertation, Universiteit Leiden).

Zhang, J.-M., Ma, F., & Xu, K.-W. (2004). Calculation of the surface energy of FCC metals with modified embedded-atom method. *Applied Surface Science*, 229, 34–42. doi:[10.1016/j.apsusc.2003.09.050](https://doi.org/10.1016/j.apsusc.2003.09.050)